Liquid Needle Free Injectors:
Design and Analysis of Power Sources

Rocco Portaro

A Thesis

in

The Department

of

Mechanical, Industrial and Aerospace Engineering

Presented in the Partial Fulfilment of Requirements

For the Degree of Doctor of Philosophy (Mechanical Engineering) at

Concordia University

Montreal, Quebec, Canada

August 2022

CONOCRDIA UNIVERSITY

SCHOOL OF GRADUATE STUDIES

This is to certify that the thesis prepared

By: Rocco Portaro

Entitled: Liquid Needle Free Injectors: Design and Analysis of Power Sources

And submitted in partial fulfillment of the requirement for the degree of

                Doctor of Philosophy Mechanical Engineering

complies with the regulations of the University and meets the accepted standards with respect to originality and quality

Signed by the final examining committee:

              _____Chair

              Dr. Ahmed Kishk

              _____Thesis Supervisor

              Dr. Hoi Dick Ng

              _____Examiner

              Dr. Lyes Kadem

              _____Examiner

              Dr. Gerard J. Gouw

              _____Examiner

              Dr. Nizar Bouguila

              _____External Examiner

              Dr. Hachimi Fellouah

Approved by   _____Graduate Program Director

              Dr. Muthukumaran Packirisamy

August 11th, 2022   _____Dean or Delegate

              Dr. Mourad Debbabi

Abstract

Liquid Needle Free Injectors: Design and Analysis of Power Sources

Rocco Portaro, PhD.
Concordia University, 2022

Drug delivery without the use of hypodermic needles has been a long-term objective within the medical field. Although there exist many different needle free technologies such as, but not limited to: electroporation, tape striping, transdermal patches, micro-needles or ultrasound therapy, these have typically been limited to the delivery of micro-molecules and small volumes. One technique that has shown great promise for overcoming these limitations, is that of utilizing micro size, high-speed liquid jets for the delivery of large macro-molecules, and delivery volumes in line with commercially developed injectables. The devices used to administer medication through this technique are known as needle-free liquid jet injectors (NFJI), and puncture human tissue by compressing the drug, using a plunger, through a micro orifice 10-350 μm in diameter. The result is that the injectable is expelled through the orifice as a high-speed liquid jet exhibiting velocities from 100-200 m/s and attaining stagnation pressures above the critical mechanical stress required to puncture human skin. Simple spring-powered and gas-powered liquid jet injectors have been in use since the late 1930's, and have been applied to mass immunization against polio, influenza, and smallpox. However, due to the presence of pain, bruising, hematomas, incomplete delivery and cross-contamination, these devices have never seen widespread use within the medical community. Recent interest in developing this technology to reduce needle stick injuries, reduce biohazardous waste, curb the reuse of needles, and provide a delivery platform for new emerging drug therapies has led to a multitude of experimental devices aimed at increasing the delivery efficiency and precision of NFJIs.

As a result, this dissertation study will focus on contributing to the development of perhaps the most important aspect of an NFJI, the power source. This is accomplished by determining the power source requirements of NFJIs through a numerical study utilizing a computational fluid dynamic model constructed by Nakayama *et al.* (2013) and analyzing the effect of drug viscosity to underline the requirements for successful liquid jet injection. The results of this study highlight that increasing viscosity to levels required by novel drug therapies on the order of 200 cP will make it difficult for commercially available NFJI to deliver viscous injectables. Consequently, making it is necessary to

focus on developing power sources that exhibit greater energy delivery as well as controllability. This notion was explored through the design, construction, and analysis of a servo tube actuated NFJI. The prototype advanced the work conducted by Taberner et *al.,* (2012) and Do *et al.,* (2017), which utilized a controllable voice coil and linear permanent magnet synchronous motor respectively, to power their injectors. The research study presented in this work utilized advanced power electronics and fully closed-loop control to illustrate the viability and real-time controllability of linear permanent magnet synchronous motors for their use in producing high-speed liquid jets. The device could deliver both large volumes and viscous aqueous-glycerol solutions in a repeatable and precise manner.

However, it was noted that the large power consumption at the onset of the injection, required by these devices can make scaling of the technology for practical handheld sizes difficult. As a result, a combustion-driven injector was constructed and analyzed to provide rapid and substantial energy release in a smaller form factor. The study yielded a prototype capable of producing jets attaining stagnation pressures above 80 MPa, by the detonation of the gaseous mixture of acetylene-oxygen. The injector can deliver large volumes over a different range of viscosities whilst exhibiting only a slight decrease in peak and average stagnation pressure. Although it was possible to vary the peak and average stagnation pressure by adjusting the initial pressure of the combustible gaseous mixture, real-time control of jet stagnation pressure is not possible. In order to combine the scalability and energy release of the combustion-driven injector, with the controllability of a servo tube-powered NFJI, a concept is proposed in the last section of this research work. The proposed unit makes use of a high-speed rotary servo motor, coupled to an electromagnetic clutch, which then drives a lead screw to convert the rotary motion into linear motion applied to the injection chamber. The decoupling of the direct link between the motor and lead screw allows the rotary servo to ramp up to its optimal operating speed and then transfer its energy in a 3 ms window through the electromagnetic clutch. This will enable the use of smaller motors and power electronics, resulting in high-powered NFJIs contained within practical form factors for clinical settings.

Acknowledgments

Table of Contents

List of Figures

List of Tables

List of Symbols

A Area [m^2]

b, h   O-ring thickness [m]

B Bulk modulus [GPa]; Magnetic field strength

c Speed of sound [m/s]

C Characteristic lines

C_v Specific heat at constant volume [J/kg-K]

F Force [N]

l Drive screw lead [mm]

i Current [A]

L_0 Initial injection chamber length [m]

M_p Mass of plunger [kg]

p Pressure [Pa]

V Injection volume [m^3]

V_D Volume of driver [m^3]

R Universal gas constant [kJ/kmol-K]

t Time [s]

T Temperature [K]

x Distance [m]

Greek Letters

α   Strain hardening exponents; Friction coefficient; Lead angle; Liquid volume fraction

γ   Mesh diffusivity; specific heat ratio

κ   O-ring compression fit [N]

λ_n Principal stretch ratios

μ   Shear modulus [N/m^2]; viscosity [Pa·s]; friction coefficient

φ Energy density [J/m^3]

Ψ   Compressibility [Pa^{-1}]

ρ   Density [kg/m^3]

τ   Time decay [s^{-1}]

Γ-   Riemann invariant

β   Friction term

η   Screw efficiency

Chapter 1 : Drug Delivery using Liquid Jet Injection

1.1 Introduction

Today's society has witnessed tremendous technological breakthroughs which are helping to deal with the challenges of an ever-increasing population, and new threats posed by novel viruses like COVID-19. A great emphasis is placed on providing the most efficient and comfortable health care to patients. In order to achieve these objectives, the health care profession often implements engineering concepts to solve the problems it faces. This has resulted in many new medical breakthroughs. Technologies such as minimally invasive robotic surgery and advanced imagining techniques such as magnetic resonance imaging are just a few examples of biomedical engineering innovations used to make medical procedures safer, more effective and decrease recovery time.

One technology that has yet to be fully exploited in the realm of biomedical engineering is that of micro size, high-speed, liquid jets (**Fig. 1.1**). These micro-sized jets demonstrate great promise for their use in needle-free drug delivery (Mitragotri, 2005 and 2006). They have been successfully used to deliver drugs into the epidermal, subcutaneous and intramuscular regions. Moreover because of the simplicity of the delivery procedure, no special training is required for administering an injection, which is accomplished in less than a few seconds and lends itself well for mass immunization. This can greatly aid in vaccination efforts when health care professionals are faced with the task of delivering an extremely large number of injections rapidly and in ways that reduce biohazardous waste, deliver the medication more efficiently and decrease the reluctance to undergo vaccination due to needle stick phobias.

Healthcare professionals currently administer most medication using hypodermic needles. Although this practice has been used for over 300 years, and advancements in design and manufacturing have improved the performance of needles, drawbacks such as accidental needle stick injuries, transmission of deadly viruses and bio-hazardous waste are still present. It is estimated that approximately over 2 million healthcare professionals are subject to accidental needle stick injuries each year, with 40% resulting in some form of cross-contamination leading to Hepatitis B and C. This figure is only exacerbated if the cases of cross-contamination in developing countries are considered, whereby the medical systems practice the reuse of needles. Moreover, if the COVD-19 immunization efforts are considered, whereby a large quantity of the

world population must be vaccinated to overcome the transmission of the virus, the use of traditional techniques in these circumstances is not only subject to the aforementioned drawbacks, but also play a psychological role in deterring people with trypanophobia, a very real medical condition that deals with the fear of needles and leads to approximately 10% of the population to avoiding vaccination or complying with medical treatments.

Figure 1.1 Early air-powered needle-free injector (Washington Post, 2021 www.washingtonpost.com)

In order to eliminate these drawbacks, the scientific community has focused on developing many types of needle-free technologies such as tape stripping, ultrasound and electroporation illustrated in **Fig. 1.2** (Mitragotri, 2005). Many of these methods are limited to delivering micro molecules by diffusion through skin pores. However, a technique known as liquid jet injection, which originated in the 1930's can deliver both micro- and macro-molecules by penetrating the skin using a micrometer scale high-speed liquid jet. This topic has undergone research for the past 50 years, however it is only in the last few decades that interest has grown substantially. This concept has been used to immunize the masses quickly and effectively against diseases such as polio, influenza and smallpox. Although these devices have shown great potential in delivering a wide range of medication at different tissue depths, they are prone to producing pain, bruising, hematomas, excessive penetration, and cross-contamination (Hingson *et al.*,1963; Wijsmuller *et al.*, 1974; Schneider *et al.*, 1994). This has greatly hindered their widespread use, and little research has been conducted on understanding the principles governing the mechanics of liquid jet injection in order to propel its mainstream use.

1.2 Relevance of Liquid Jet Injection in Today's Health Care System

In order to improve the performance of needle-free injectors, ongoing research that focuses on analyzing the fluid dynamics of jet injection is being conducted to render this technology feasible for widespread commercial use as well as for use with emerging drug therapies. This is because jet injectors are a suitable platform for dispensing emerging medical treatments such as DNA therapy, which require precise drug localization. It will be necessary to target shallow layers of the skin such as the epidermis as well as sensitive organs. Recent studies demonstrate that jet injectors can target the shallow portions of the epidermis which contain Langerhans cells as well as soft tissue. These cells play a vital role in the human body's immunological response to viruses. Consequently, DNA therapies used for cancer treatment as well as immunization are under investigation using jet injectors
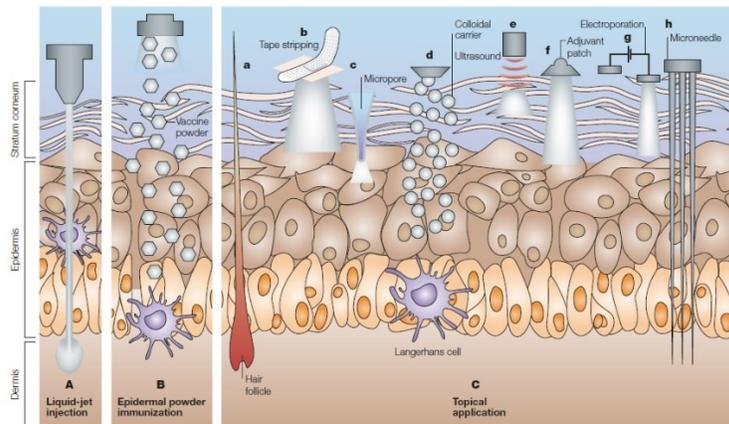
Figure 1.2 Different methods for needle-free drug delivery (Mitragotri, 2005)

Furthermore, liquid jet injectors can also be used for targeting diseases which benefit from localized treatment techniques. These include vascular occlusive disease, whereby the injector produces a jet of sufficiently small diameter to puncture small blood vessels within the eye and deliver pico-liter amounts of medication to unblock occlusions (Fletcher *et al.*, 2001). Researchers have also found that liquid jet injection provides an ideal platform for specifically targeting myocardial tissue and utilizing specific gene expressions to treat heart disease (Fargnoli *et al.*, 2014). A recent study conducted by Mckeage *et al.* (2021) also suggests that liquid jets can help deliver localized dental anesthetic and eliminate the long and painful needles used in dental procedures. However, one of the major challenges hindering the successful implementation of these new types of treatments is the inability to provide reliable, precise and controllable jets. The

current generation of liquid jet injectors lack the ability to vary jet velocity as the injection is progressing, and the ability to deliver viscous injectables with viscosities greater than 200 cP as required by DNA therapy remains unclear. Injectors capable of controlling jet velocity remain in the experimental prototype stages and no significant work has been accomplished on optimizing needle-free liquid jet injection for the aforementioned medical treatments.

| Medication Delivered Via Needle-Free Injection ||
Drug	Usage
Vaccines	Immunization
Insulin	Blood Sugar Control
Growth Hormones	Increase Growth Rate
Lidocaine	Anesthetic
Midazolam	Sedative
Erythroprotein	Proteins for DNA Therapy
Interferon	
Botulinum Toxin	

Table 1.1 Examples of drugs administered via liquid jet injector (Mohnanty *et al.*, 2011)

1.3 Fundamental Concepts Related to Liquid jet Injection

The goal of needle free liquid jet injections is to puncture human skin and deliver large macro-molecules, while minimizing damage to the skin caused by the injection. In order to accomplish this objective, it is necessary to have a general understanding of skin anatomy as well as the physiology of drug absorption through the different parts of the skin. This will underline the forces, power and timescales that are required for liquid jet injection. The following section outlines the fundamentals of liquid jet injection based on work conducted by Portaro and Ng (2015).

1.3.1 Skin Anatomy and Physiology

The human skin is the body's largest organ and is composed of three main parts: the epidermis which comprises the skin's outermost layer, the dermis which lies beneath the epidermis and is a fiber-like network of protein, and finally the subcutaneous tissue composed mainly of fat (see **Fig. 1.3**). The skin has complex anatomical and physiological aspects, which vary greatly with location in the human body. For example, the thickness of the epidermis and dermis can change substantially from one location to another. This can be seen by observing the thickness of the

epidermis on the eyelid which measures just 0.1 mm and comparing it to the thickness of the epidermis on the sole of the foot which measures almost 1.5 mm (McGrath *et al.,* 2004). Understanding these variations is essential in developing an injector, that delivers adequate power and that has the capability to deliver medications to different parts of the body.
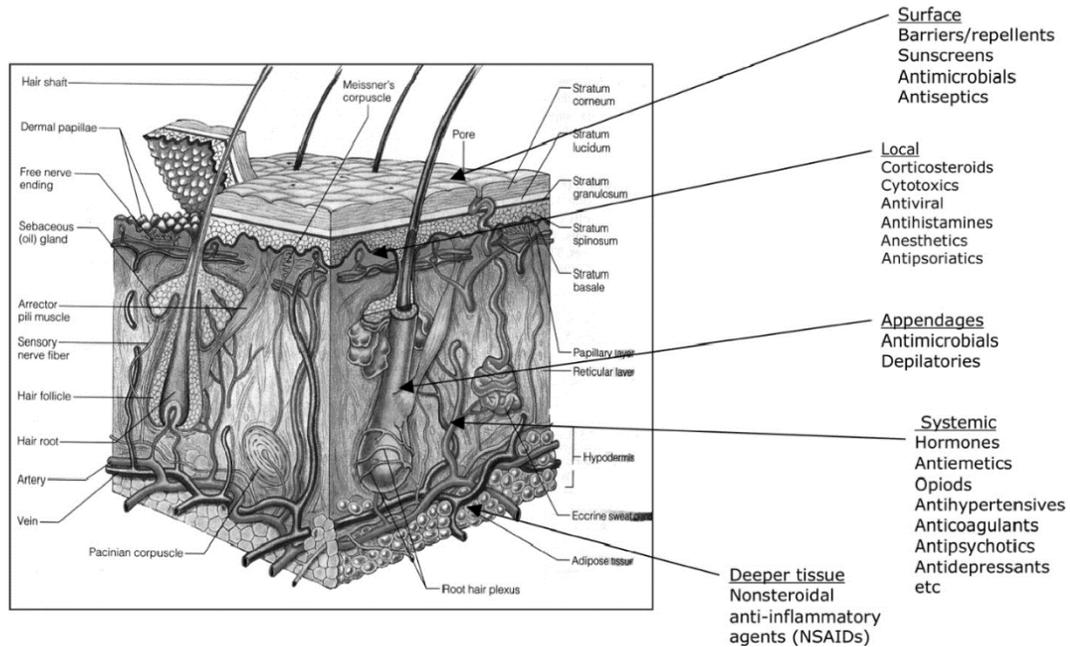
Figure 1.3 Skin anatomy and physiological aspects (Brown *et al.,* 2006)

1.3.2 The Epidermis

The Epidermis is the skin's outermost layer and is comprised of two types of cells, keratinocytes and dendrite cells. Keratinocytes comprise 80% of the epidermal layer and are long thread-like proteins which help protect the body against external chemical, physical and biological risks. The dendrite cells found in the epidermis take the form of Langerhans, which act as antigen processing units. Basically, when a foreign substance is detected the Langerhans cells become active and migrate to lymph nodes where they provoke an immunological response. The epidermis also contains other auxiliary cells such as melanocytes and Merkel cells which also play a protective role and help give the skin its pigmentation (Kolarsick *et al.,* 2011). **Figure 1.4** illustrates a cross-section of the epidermis, which is divided into four distinct layers, consisting of the cornified layer, the granular layer, the squamous and the basal layer.
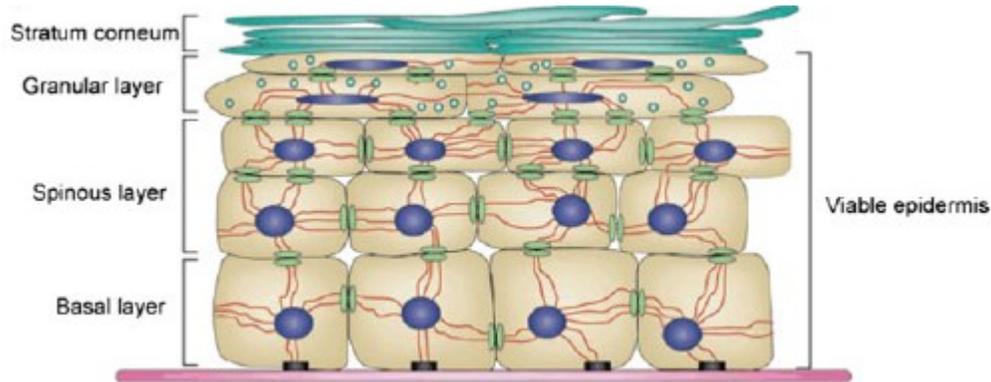
Figure 1.4 Cross-section of epidermis (Kendall, 2010)

The cornified layer (stratum corneum) is the most superficial layer of the epidermis and consists of corneocytes cells which provide mechanical protection against external elements. The corneocytes are dead skin cells due to the fact that they have lost their nuclei through a process termed "*terminal differentiation*". The cornified layer of the epidermis is extremely high in protein content due fact that it must exhibit mechanical toughness. Furthermore, the properties within the cornified layer vary greatly with depth. This is the case with the water-binding capacity of the corneocytes which increases as the cornified layer is traversed. Consequently, as the corneocytes make their way up to the surface they dehydrate and eventually flake off the skin. A needle-free injector must provide enough force to penetrate through the 15 to 20 layers of these dead skin cells. This is no trivial task as the thickness of this layer can vary substantially from 5 to 20 μm (Gad 2008). Further complicating matters is the fact that the breaking stress of this layer varies significantly with ambient humidity. In fact, studies have demonstrated that the breaking stress of this layer can vary from 22.5 MPa at 0% humidity to 3.2 MPa at 100% humidity. The breaking stress also decreases with increasing depth within the layer (Kendall, 2010).

The next layer of the epidermis beneath the cornified layer is known as the granular layer. This layer is proportional in thickness to the cornified layer and is the last layer of the skin to contain living cells. In fact, it is in the granular layer whereby the keratinocytes undergo a terminal transformation in order to become corneocytes, which is carried out in part by enzymes found in this layer. Furthermore, the granular layer also contains keratohyalin cells which are used in the synthesis of various proteins.

Immediately preceding the granular layer is the squamous layer, referred to as the stratum spinosum. This layer is composed of polyhedral-shaped keratinocytes approximately 5 to 10 cells in thickness. The main role of the squamous layer is in the synthesis of proteins such as cytokeratin. The cytokeratin combines with cytoplasmic proteins also found within the squamous layer, in order to form desmosomes. The desmosomes provide a strong linking agent between keratinocytes.

The final layer of the epidermis is known as the basal layer, this layer is characterized by long column-shaped keratinocyte cells that attach with their long axis perpendicular to a junction layer between the epidermis and the dermis known as the basement layer. The basal layer also contains mitotically active cells, which means the cell division and cell growth take place within this layer. It typically requires 14 days for a newly developed cell within the basal layer to undergo a complete cycle and become a corneocyte (Kolarsick *et al.,* 2011).

It is important to note the epidermis is constantly evolving and as such can be considered a "*dynamic layer*", cells are travelling from the basal layer up to the cornified layer and they eventually flake off the skin. This process of cell traveling through the various layers of the epidermis is termed keratinization. The cell first undergoes a period of synthesis while it travels through the basal and squamous layers. During this period the cell builds up a cytoplasmic supply of keratin that serves as the cell's cytoskeleton. The degradation phase takes place in the granular layer and cornified layer, whereby the cells do not synthesis rather they lose organelles until even the cell nucleus is removed. The cells are then considered dead and at this point have migrated to the outermost part of the epidermis. Each layer of the epidermis plays an important role in skin regeneration as well as protecting the body from external hazards.

It is of extreme importance to consider this dynamic behavior of the skin when designing a needle-free liquid injector. This is because for the injector to deliver medication it must wound the skin, in other words, it must make a hole which will not heal instantaneously, introducing an entry point for external elements to enter the body. It is important to understand the mechanisms the skin has in place for providing protection as well as the length of time it takes for wounds to heal and regain original skin properties.

1.3.3 The Basement Layer

The basement layer is a junction between the epidermis and the dermis; it is an extremely important part of the skin anatomy and has many specialized roles. It helps establish cell polarity and direction of growth, provides development signals and acts as a semi-permeable layer (Kolarsick *et al.*, 2011). The basement layer consists of a porous zone that allows fluid exchange between the dermis and epidermis and also forms a support structure that holds the epidermis to the dermis. Among the many cells found within this junction zone, the basal keratinocytes are of particular importance. This is because they are the cell which will form anchoring fibrils and microfibrils that will transfer shearing and tensile forces from the epidermis to the dermis.

1.3.4 The Dermis and Subcutaneous Tissue

The dermis is found beneath the epidermis and the basement layer; it comprises the bulk of the skin and is composed primarily of collagen (70% dry wt.) (see **Fig. 1.5**). Collagen has similar mechanical properties to nylon and aids in giving skin its pliability, elasticity, and tensile strength (McGrath *et al.*, 2004). Consequently, the dermis serves to protect the body against mechanical injury, in contrast to the epidermis which serves to seal the skin from external chemical and biological hazards. Moreover, the dermis exhibits a clear structural arrangement of components that are predictable in a depth-wise manner and the cells within the dermis do not undergo a differentiation process. Fibrous filaments, amorphous connective tissue, nerve endings and vascular networks can also be found in the dermis. Below the dermis it is possible to locate the subcutaneous tissue, which is composed mainly of fat. In this layer it is possible to find blood vessels, lymphatic vessels and even nerve endings. It is important to note that this is the layer of the skin that is targeted for the delivery of hormones using conventional hypodermic needles. This is because minimal pain is sensed by inserting objects into this region. The subcutaneous tissue can be considered the final layer of skin, directly beneath it is the muscular tissue. Therefore, needle-free liquid injectors must also exhibit the ability to penetrate these layers of the skin in order to deliver medication developed to function with these tissues.
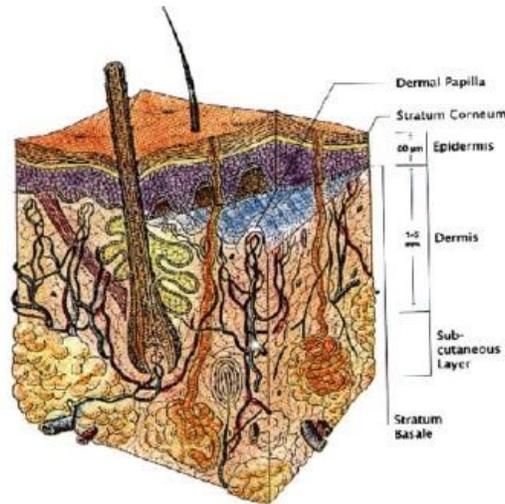
Figure 1.5 Detailed skin anatomy (Kendall 2010)

Understanding the structure of the skin is fundamental in creating a needle-free injector that will function efficiently and painlessly. The above description of the skin makes it possible to observe that it is possible to inject into the epidermis or basement layer causing only minor sensation of pain. This is because nerve endings are only present in the dermal layer. Moreover, once injected through the epidermis the medication will diffuse into the dermis and subsequently be absorbed by the body.

1.4 Drug Absorption by Needle Free Liquid Jet Injection across Skin

There are two routes by which drugs can be administered to the human body these are parenteral and enteral. A drug administered to the body which is absorbed in the intestinal tract is considered as an enteral route for absorption, while a drug administered from outside the body that makes its way directly to the bloodstream is considered parenteral. Consequently, an injection given by a needle-free injector is parenteral. This is because a liquid jet punctures the skin and makes a depot of medication at some specific depth where it then diffuses into the bloodstream (Gad, 2008).

The conventional hypodermic needles target three specific areas for drug absorption these include intra-dermal, subcutaneous, and intramuscular sites. Needle-free injectors can also target these specific zones and have the advantage of targeting sites which are much shallower than those used by conventional hypodermic needles. The drug absorption from these shallow injection depths is termed trans-dermal absorption. It is important to understand the intricacies of the more common injection sites as well as the newly targeted areas to design a versatile needle-free injector.

The typical injection sites include intra-dermal, subcutaneous and intramuscular regions. Intradermal injections consist of depositing medication into the dermis which is rich in capillaries. The medication then diffuses from the initial deposit site to the blood capillaries and then makes its way into systemic circulation. It is important to note that the maximum volume that can be administered via this technique is 0.1 ml. Subcutaneous injections are usually performed at depths just below the dermis into the fatty tissue. The maximum volume of liquid that can be injected within this region is 2 ml. Moreover, the absorption rate can be increased by massaging the injection region once the injection is performed. This forces the concentrated deposit of medication to spread out and make more contact with blood capillaries.

Intramuscular injections consist of depositing medication within the muscular tissue. Although this is a painful event due to the sensory nerves found within this region, there also exists quite an extensive blood supply which leads to very rapid absorption. The maximum volume that can be injected intramuscularly varies depending on the body site typically from 2 ml to 15 ml. Regardless of the injection site; there are only two mechanisms that govern drug absorption for these three regions. Once the medication has been delivered it can either travel through lymphatic vessels, or capillaries. The method of absorption is dependent on the molecular weight of the drug. If it is greater than 2000 Daltons the drug will be absorbed by the lymphatic system; if it is less then it will be absorbed by blood capillaries.

It is important to note that the surface of capillaries is covered with pores. The absorption rate of the drug into systemic circulation is dependent upon its ability to diffuse into these pores. The rate at which the medication diffuses into the pores is governed by Fick's law,

$$\frac{dQ}{dt} = \left(\frac{D * P * S}{L * V_a} + \frac{D' * S'}{\eta * L' * V_a} \right) Q_a \qquad \text{Eq. (1.1)}$$

where dQ/dt is the absorption rate of the drug, Q_a is the amount of drug in the injection region, and the other coefficients depend on skin properties.

Transdermal injections are performed by depositing medication into the epidermis, typically under the cornified layer, and relying on passive diffusion to transport the medication into systemic circulation. Although absorption is slower because drugs administered in this way must make their way into the dermis before entering the blood supply, there is much research into using this area

for vaccination purposes. This is because the epidermis contains Langerhans cells which provoke immunological responses (Gad, 2008). Consequently, it was established that vaccinations targeted in this region were much more effective than those administered in the intramuscular region. It is also very important to note that targeting these shallow depths via the use of needles is extremely difficult, however with the use of needle-free injectors it is possible not only to target conventional injection zones but to explore the development of more efficient vaccines and hormones designed to work at an epidermal level (Kendall, 2010)

1.5 Puncturing Tissue and Depositing Medication by Liquid Jet

In order to administer an injection a liquid jet must first puncture soft tissue and then deposit the medication within a target region. Thus, the injection process by liquid jet is made up of two distinct phases; an initial high-velocity phase whereby the liquid jet fractures the surface of soft tissue such as the skin and creates a hole, followed by a slow-speed phase where the injector deposits the medication in the target area. In the first phase the liquid jet emanating from the injector must have enough power to penetrate the tissue and create a hole yet avoid over penetration which can lead to bruising and pain. In order to determine the required jet velocities and stagnation pressures in the first phase, it is necessary to model the jet-skin interactions. A study conducted by Shergold *et al.* (2006) describes the fracture mechanisms at play when the liquid jet penetrates the skin, as well as the minimum stress required to puncture human flesh as a function of jet diameter.
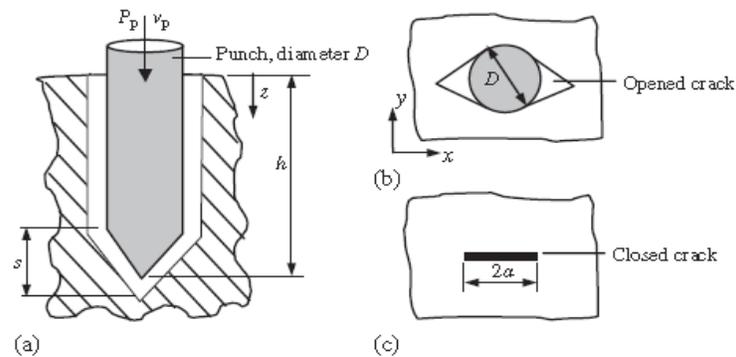
Figure 1.6 Skin crack model parameters (Shergold *et al.*, 2006)

The Shergold *et al.* (2006) sharp-punch model for skin fracture by liquid jet is analogous to a sharp-tipped punch creating a hole through a soft solid material. The study suggests that the hole formation is initiated by the appearance of a planar crack (see **Fig. 1.6**). In order to model crack

formation, it is assumed that skin behaves like a hyper-elastic, anisotropic, incompressible material. The Ogden equation, which describes strain energy density, can then be used to describe crack formation and forces necessary to puncture the skin. The equation describes the relationship between φ energy density per unit volume, μ shear modulus, α strain hardening exponents and λ_n principal stretch ratios, i.e.,

$$\varphi = \frac{2\mu}{\alpha^2}(\lambda_1^2 + \lambda_2^2 + \lambda_3^2)$$

Eq. (1.2)

The strain hardening exponents, shear modulus and stretch ratios for the model were determined experimentally by sampling human skin taken from cadavers. These parameters then make it possible to determine a relationship between jet diameter and the necessary pressure required for hole formation.
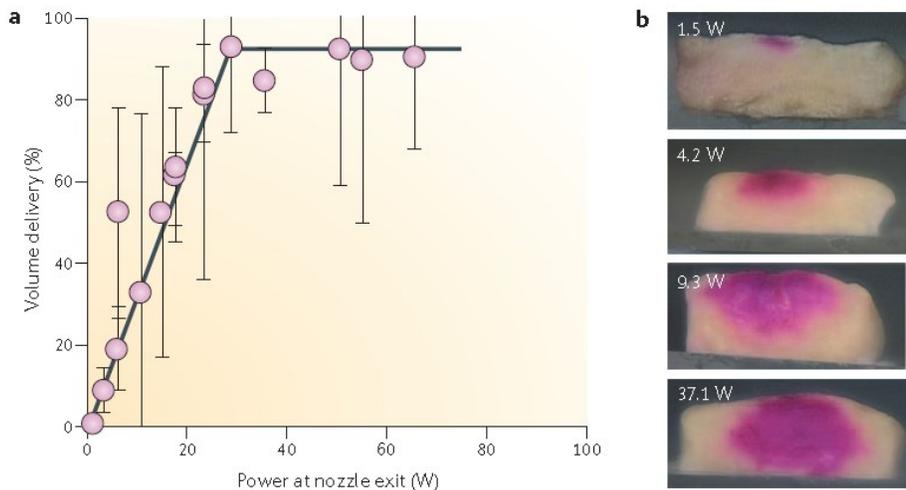
Figure 1.7 a) Delivery efficiency versus power; and b) penetration versus power (Mitragotri, 2006)

It is also important to note that inadequate jet power in hole formation will lead to incomplete injection delivery. The term "*completeness of injection*" is used to describe the amount of medication that is delivered to its target destination versus the quantity that splashes back during initial hole formation. Incomplete delivery occurs due to splash back of fluid upon its impingement on the skin, as well as hole formation rates which are smaller than volumetric flow rates. The latter of these cases causes an outflow of the medication from the hole. The skin can be thought of as a sponge with a hard surface. The jet must be strong enough to pierce this hard outer layer, and yet provide a flow rate that does not exceed the absorption capacity which would cause outflow.

Studies have shown that the completeness of injection varies linearly with jet power (Mitragotri, 2006). In fact, greater than 90% completeness can be achieved when a jet exhibits more than 30 Watts of power.

Figure 1.7 illustrates the relationship between the liquid jet power and subsequent completeness. It can be concluded that above 30 Watts of power no further gain in completeness is obtained. However, penetration depth increases as jet power is increased. The jet power is a critical parameter in the second phase of injection, whereby the medication is deposited in the target area. Commercially available injectors exhibit a high-pressure peak during the first phase followed by a rapid decline to relatively constant injection pressure. This behavior can be easily observed from a stagnation pressure trace of the jet as illustrated in **Fig. 1.8**. It is the power of the jet during this constant second phase which determines the depth at which the fluid will be deposited.

First Phase Hole: Formation at High Pressure

Second Phase: Drug Deposition

Stagnation Pressure (MPa)

Time (ms)
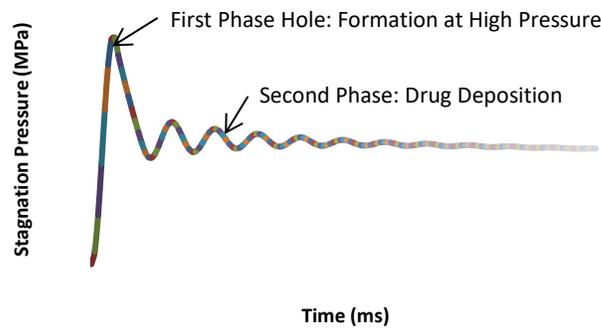
Figure 1.8 Stagnation pressure during injection phases (Portaro and Ng, 2015)

Shergold *et al.* (2006) demonstrated that a liquid jet of diameter *D*, traveling at velocity *U*, with a certain density *ρ* will impart a power given by the following formula:

$$Power = \frac{1}{8}\pi\rho D^2 U^3 \qquad\qquad \text{Eq. (1.3)}$$

It is possible to conclude that power can be increased by augmenting jet velocity, jet diameter as well as density. Nevertheless, in practice the jet diameter must be minimized in order to reduce pain and bruising, leaving velocity and density as the main parameters for increasing power. Although it is known that jet velocity will increase penetration depth, there is still a need to describe this relationship in a quantitative manner. This poses unique challenges as skin properties change between individuals as well as body site locations.

1.6 Mechanics of Needle Free Liquid Jet Injectors

The high-speed jets used for the delivery of medication are produced in several ways (e.g., see review articles by Ravi *et al.*, 2015; Baxter and Mitragotri, 2006; Barolet and Benohanian, 2018; Vadlapatla *et al.*, 2021; Han *et al.*, 2021). In commercially available injectors a power source, typically a spring or high-pressure gas, compresses a piston which in turn forces a column of fluid through a micro orifice on the order of 50 to 250 μm in diameter. The resulting compression of the fluid column creates a high-speed jet with a speed on the order of 100 - 200 m/s, with Reynolds numbers in excess of 100 000. Typically the pressure increase in the fluid column can peak in excess of 30 MPa within 0.5 ms. These pressure values are well above the minimum threshold of 3 - 15 MPa for fracturing skin. In fact, commercially available injectors that are capable of producing such pressure peaks can routinely deliver 0.1 to 1 ml of fluid at depths greater than 10 mm.

In an effort to improve the performance of conventional liquid jet injectors, the scientific community has developed models that can be used to predict parameters such as the stagnation pressure of a liquid jet based on process variables such as the jet diameter, power source and fluid viscosity. The fundamentals of needle-free injection were modeled in detail by Baker and Sanders (1999). In this study a one-dimensional continuum analysis assuming quasi-static incompressibility was conducted on a spring-powered injector. This resulted in a system of two ordinary differential equations, describing the pressure within the column of medication to be injected as well as the displacement and force of the injector piston.

$$\frac{dp}{dt} = \frac{(B+p)\dfrac{dx}{dt} - \dfrac{BA_o}{A_p}\sqrt{\dfrac{2p}{\rho_o}}}{L - x_p} \qquad\qquad \text{Eq. (1.4)}$$

$$\frac{d^2x}{dt^2} = -\frac{kx_p}{m_p} - \frac{A_p}{m_p} - \frac{dx}{dt}\frac{F_f}{m_p\left|\dfrac{dx}{dt}\right|} \qquad\qquad \text{Eq. (1.5)}$$

Equation 1.4 describes the pressure differential as a function of time using the bulk modulus of the liquid B, the initial density ρ_0, the piston area A_p, the exit orifice area A_o as well as the piston displacement x_p and fluid velocity u_o at the nozzle orifice. This equation considers the pressure

increase caused by the displacement of the piston as well as the pressure decrease caused by the mass flow exiting the injection chamber. Similarly, **Eq. 1.5** depicts a force balance conducted on the injector mechanics and takes into account, the piston displacement x_p, the fluid pressure acting on the piston face, the force generated by the driving power source as well as frictional forces F_f. Baker and Sanders (1999) also determined the most sensitive parameters governing injector stagnation pressure. These are illustrated in **Fig. 1.9**, which compares the effect of parameters such as: chamber length L, piston area A_p, initial piston velocity v_o, piston mass m_p, spring constant k, initial density of the fluid ρ_o, exit orifice cross-sectional area A_o and the initial displacement of the piston x_o on the maximum pressure that can be achieved as well as the time required to achieve this pressure.
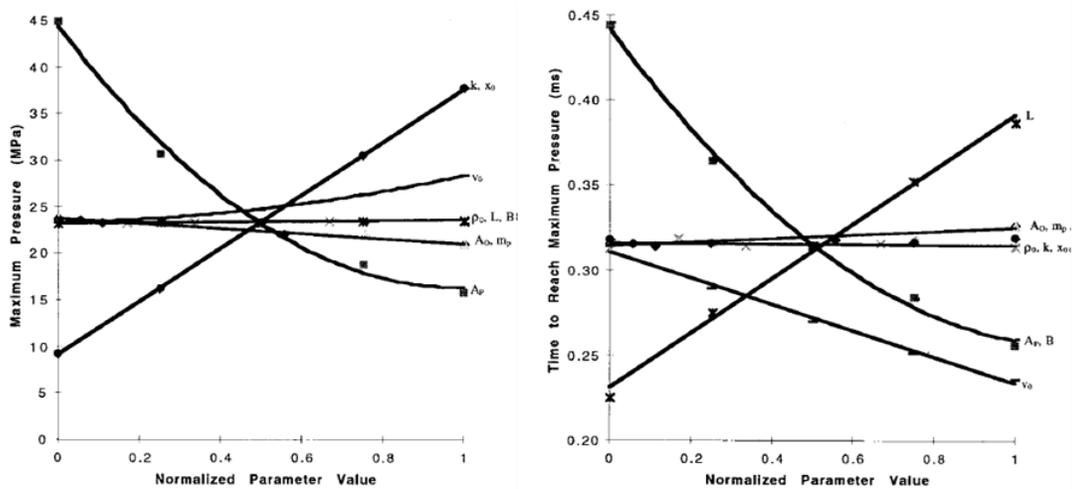
Figure 1.9 Effects of physical injector parameters on jet pressure (Baker and Sanders, 1999)

1.7 Power Sources

The power source driving an injection is one of the most influential and researched aspects of liquid jet injectors. The majority of commercially available injectors create high-speed liquid jets by compressing a liquid column using a piston driven by a power source. It is important to note that although this methodology is common throughout various types of injectors the power sources driving the injection vary greatly. Early needle-free injectors were spring-powered, driving the injection was accomplished by compressing a spring which is subsequently released to drive a plunger which forces fluid through an orifice (Baker and Sanders, 1999; Schramm-Baxter and Mitrogotri, 2002 and 2004; Baxter and Mitragotri, 2005; Brown et al., 2006; Chen et al., 2010 and 2011; Rohilla and Marston, 2019; Rane and Marston, 2021). In these types of injectors spring

compression was achieved using screw mechanisms or bulky levers. Spring-powered injectors provide a very cost-effective means of delivering injection because the spring powering the injection can usually last for the life of the injector (Schneider *et al.*, 2020; Mohizin and Kim, 2022).

Although spring-powered injectors are simple in construction and have an inexhaustible power source, they exhibit several problems. One of the major drawbacks deals with variable injection depth. Experimentation is often required to attain a target tissue region. This is due to the nature of the device, when the spring is released from its compressed state, the energy decreases non-linearly. The highest forces are produced at the start of the injection, which is necessary in order to breach the epidermis, however the subsequent jet power decays exponentially. Despite these drawbacks, spring-powered injectors are widely used.

The advent of gas-powered, needle-free injectors has helped deliver medication to target areas of the skin more accurately (Mohanty *et al.*, 2011; Portaro and Ng, 2015; Kim *et al.*, 2018; Shapiro *et al.*, 2019; Mohizin and Kim, 2020; Zeng *et al.*, 2020; Mohizin *et al.*, 2021). These injectors contain a highly pressurized cartridge of inert gas, usually helium or carbon dioxide, that propels a piston. The piston is locked in place by a trigger mechanism, when the piston is released it compresses a column of fluid which is then forced through an orifice to create a liquid jet. The basic mechanics of gas-powered injectors are illustrated in **Fig 1.10**. Gas-powered injectors exhibit greater stability throughout injection delivery due to more constant application of force on the driving piston. The pressure decay in the compressed gas cartridge is negligible during a typical injection, which is on the order of 100 ms (Portaro and Ng, 2015). Although there is still a pressure peak during the first few milliseconds of injection followed by an average injection pressure, the average injection pressure can be maintained at a specified level and does not decay as rapidly as spring-powered injectors. This makes it possible to target specific areas more easily as well as giving gas-powered injectors the ability to target deep subcutaneous tissues. It is important to note that although the gas-powered injectors are more accurate during a single injection, the accuracy decreases as the mass of compressed gas within the cartridge begins to diminish. This will cause the injection power to decrease and tissue depth targeted when the cartridge was full may no longer be obtainable.
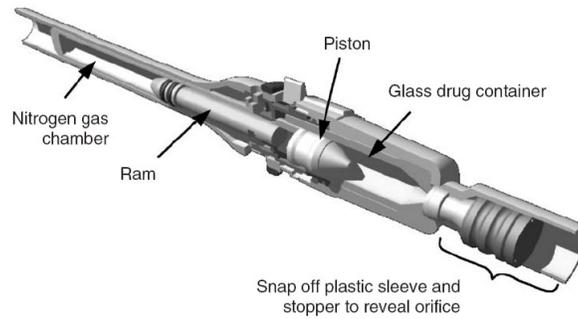
Figure 1.10. Schematic for gas-powered injector (Shergold *et al.*, 2006)

Manufacturer	Type	Power Source
Algorx	Powder Injector	Helium
Antares	Liquid Injector	Spring
Aradigm	Liquid Injector	Carbon dioxide
Bioject	Liquid Injector	Spring/ Carbon dioxide
Biovalve	Liquid Injector	Chemical gas generation system
Careteck Medical	Powder Injector	Gas
CrossJect	Liquid Injector	Air bag gas generation system
National Medical Products	Liquid Injector	Carbon dioxide
Powder Med	Powder Injector	Gas
Visionary Medical	Liquid Injector	Gas

Table 1.2. Commercially available injectors and corresponding power source (Mohanty *et al.*, 2011)

Table 1.2 illustrates that both gas-powered and spring-powered injectors form the majority of power sources for commercial injectors. However, both these types of power sources lack controllability. This implies that once they begin to drive the injection, there is no means of modifying the application of power such that variable factors like friction and fluid damping can be considered. Thus, the stagnation pressure profile produced by the injectors is fixed from its design stages and cannot be modified. Furthermore, because the power application is limited with these types of injectors, it is necessary to couple the orifice diameter with the total volume of liquid to be delivered. This usually results in the use of larger jet diameters to limit the time duration of the injection. The use of large diameter jets causes pain, bruising and hematomas which are several

reasons that have limited the widespread use of liquid jet injectors. Subtle improvements to the controllability of conventional injectors can be conducted. One method would entail the use of non-linear springs, which can be designed to produce a specific pressure profile at the exit of the injector.

1.7.1 Experimental Power Sources

In order to overcome the limitations of conventional liquid jet injectors, it is necessary to precisely control the pressure profile exhibited by the liquid jet. An early attempt to achieve this goal was conducted by Arora *et al.* (2007). In this study a custom piezoelectric crystal was coupled to an actuating piston and cycled at a frequency of 1 Hz from 0-140 V in order to create a pulsating liquid stream. The small-scale expansion of the piezoelectric crystal makes it possible to deliver doses as small as 2 nl. The pulsating nature of the liquid stream enables the injection to consist of several small doses that make up the total injection volume. This technique makes it possible to decouple the jet power from the completeness of injection. This can be attributed to smaller jet diameters and reduced quantities of fluid which require less power to penetrate tissue. These small quantities of fluid combined with smaller jet diameters (50 µm) not only increase injection completeness but also limit backsplash and reduce pain/bruising.

Although the study conducted by Aora *et al.* (2007) provides a good platform to illustrate some benefits of injection power source control, it did not provide an accurate means of describing jet pressure profiles. In fact, the system utilized a custom-built wave generator that would pulse the piezoelectric crystal to its maximum amplitude and allow for rise time adjustments. However, there was no way of controlling or monitoring the crystal's displacement and velocity. This resulted in an open-loop system that was susceptible to external factors such as variable friction and forces imparted by pressurizing a fluid column. Moreover, although small delivery quantities help decrease jet power and reduce pain and bruising, the injector was limited to delivering medication to epidermal tissue. This severely limits its applicability as most commercially available injectables are formulated to be delivered in milliliter dosages.

A fully controllable piezoelectric injector was constructed by Stachowiak *et al.* (2007). This power source consisted of a stack of piezoelectric injectors capable of a maximum displacement of 900 µm with a response time of 20 µs. The fluid pressurization time within the proposed prototype

needle-free injector is on the order of 100 μs and requires approximately 175 N of force to achieve jet speeds of 200 m/s. Thus, the piezoelectric crystal stack proposed by Stachowiak *et al.* (2007) can successfully produce the required dynamic changes to jet velocity during an injection. The control mechanism for specifying specific pressure profiles consisted of a PI loop, whereby an initial voltage profile would be sent to an amplifier via a Lab view program, and the exact position of the actuator would be monitored by a laser diode. This system allows adjustments to the voltage received by the piezoelectric stack so that the plunger position can precisely follow a prescribed profile irrespective of external factors. In order to determine the jet pressure profiles, the model proposed by Baker and Sander (1999) was invoked and the forcing term was modified to describe the relationship between voltage and force for a piezoelectric actuator. This modified model was then used to construct a frequency space transfer used to control the voltage profile sent to the piezoelectric actuator. **Figure 1.11** illustrates a desired jet velocity profile in grey and the predicted jet velocity using a modified version of the Baker and Sanders (1999) model. This figure also illustrates the predicted voltage profile required to produce the simulated velocity profile.
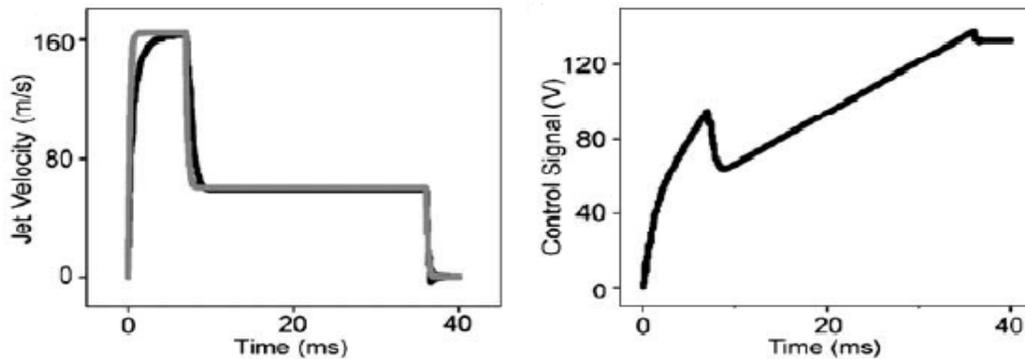
Figure 1.11. Jet Velocity and control voltage profile for piezoelectric actuator (Stachowiak *et al.*, 2009)

Prototype devices for larger volume controllable injections have also been investigated by Taberner *et al.* (2012). The prototypes in this study utilized voice coils to accurately control the plunger velocity as a function of time and better control the output pressure of the injector. Such system is subsequently used in many studies, e.g., Li *et al.*, 2016; Williams *et al.*, 2016; Ruddy *et al.*, 2017; McKeage *et al.*, 2018; Brennan *et al.*, 2019; and commercialization (e.g., Kojic *et al.*, 2017; Kelley *et al.*, 2021). Although they displayed some level of controllability, the power sources behind these devices were better suited to high-frequency response times rather than high force output. Ruddy *et al.* (2017) demonstrated that voice coils for larger volume and power would

not lead to practically sized injectors. The better solution, which is investigated in this thesis, concurrently with Do *et al. (*2017; 2018) invokes the use of permanent magnet synchronous motors to propel the plunger in a very precise manner. The study conducted by Do *et al.* (2017; 2018), focused on the optimization of the sizing of linear PMSM for use in delivering jet injections. The study only tested this concept under open-loop control. Consequently, it is difficult to judge whether this platform can tailor pressure profiles with adequate precision.

Electronically controlled actuators offer an elegant solution by which to tailor the pressure output of needle-free injectors, however, limitations exist in the ability to provide enough power at the onset of plunger motion. The high force requirements within the first 10 ms of injection, specifically when considering more viscous formulations, will still require exploring techniques that can generate high impulse forces in a predictable and practical package. One such prototype known as the Pyro-drive jet injector, produced by Actranza Labs (Daicel Corp.) and illustrated in **Fig. 1.12**, utilizes the burning of solid propellant to create the necessary forces for drug delivery. The study conducted by Miyazaki *et al.* (2019) characterizes the fundamentals of this technique. The injector utilizes two solid propellants, zirconium and potassium perchlorate, in powdered form, as the initial propellant (IP) and a combination of 98% nitrocellulose, .8% diphenylamine and 1.2% potassium sulfate arranged in a columnar shape, as the secondary propellant (SP). The IP serves as the ignition source and does not generate gas pressures upon burning and serves to ignite the SP which then generates a pressure that drives the plunger forward. Miyazaki *et al.* (2019) have demonstrated that varying the ratios of IP to SP, can reliably produce pressure profiles of varying peak and average stagnation pressures. In fact, the study demonstrated that peak pressures over 40 MPa can be achieved with a small amount of either propellant. This study illustrates the power and repeatability that can be achieved by using a reaction mechanism to generate a pressure wave driving the injection. More research is required into developing different power sources that utilize combustion and detonation as a means of powering jet injectors.
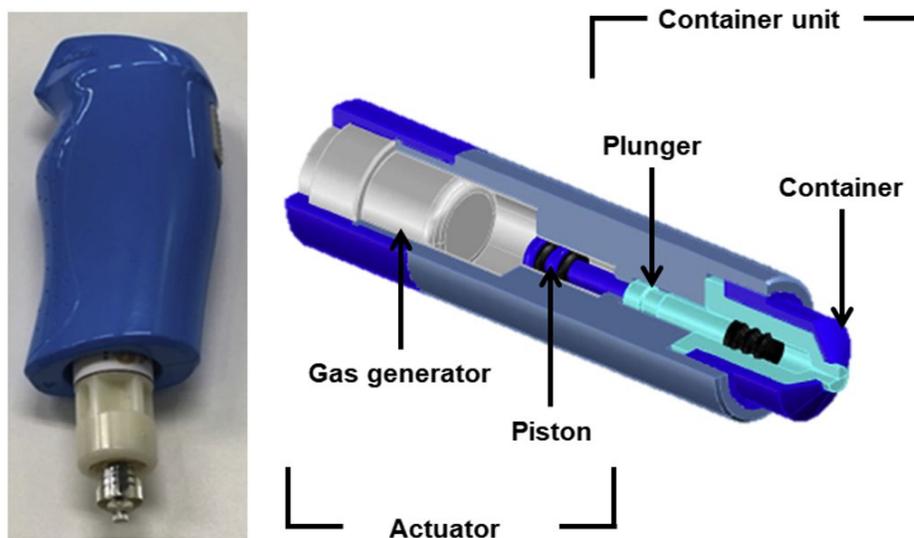
Figure 1.12 Schematic depicting the internal composition of Pyro-Drive injector (Miyazaki *et al.*, 2019)

Although the compression of a column of fluid with a piston is the conventional means of producing high-speed jets, there also exist methods that rely upon the expansion of vapor bubbles within the liquid to be administered. The common methods for the production of jets using this technique require laser radiation (Menezes *et al.*, 2006) or electrical current discharge (Fletcher and Palanker, 2001). In the laser technique, radiation is absorbed by the fluid and expanding vapor bubbles are formed (Tagawa *et al.*, 2012; Berrospe-Rodriguez *et al.*, 2016; Kiyama *et al.*, 2019; Krizek *et al.*, 2020; Miyazaki *et al.*, 2021; Lee *et al.*, 2022; Schoppink and Fernandez Rivaz, 2022). These expanding bubbles drive fluid through an exit orifice at a speed in excess of 90 m/s. The expanding vapor bubbles then collapse after reaching the limits of expansion, also expelling steam through the nozzle. Laser-driven injectors are useful for producing pulsed jets, whereby the laser is cycled at a given frequency. This enables medication to be administered as a series of short, nanoliter doses preventing splash back. However, there is no way of providing dynamic control over the pressure profile of the jet, and the laser radiation could potentially damage the medication to be administered. The use of electric charges has also been successfully used to create micro jets. A study conducted by Fletcher and Palanker (2001) utilizes a thin 25 µm electrode which is surrounded by an electrolytic solution that contains the drug to be administered. The solution and electrode are enclosed in a glass capillary tube with a grounded metal sheath applied to the outer wall of the electrode insulation. In order to produce the jet, electric pulses of 1 kV are sent through the central electrode, the charges then travel through the electrolytic solution and create high-

temperature plasma streamers. The latter causes the formation and expansion of vapor bubbles forcing liquid through the nozzle at speeds similar to those obtained using laser radiation. Although this experimental technique has shown promise for intravascular drug delivery, the safety aspects of utilizing high voltage currents as well as the thermal effects induced on the delivered medication have yet to be investigated.
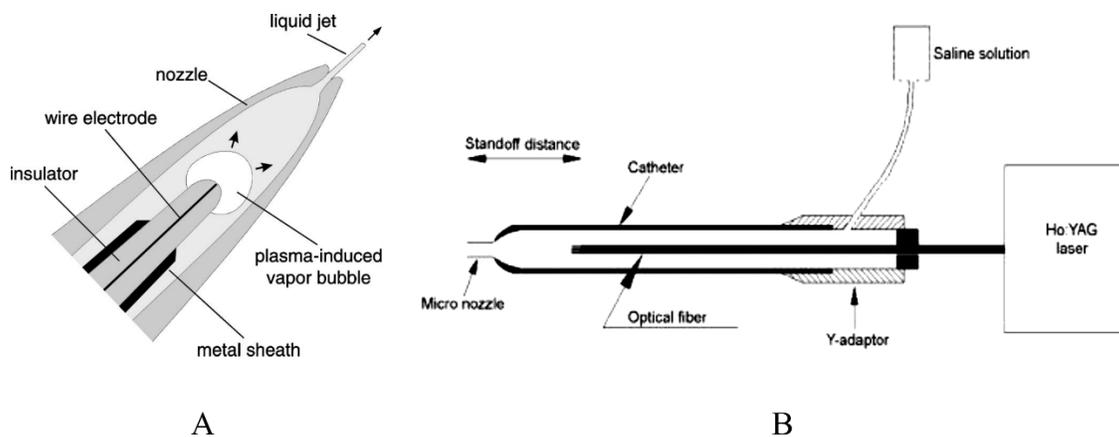
Figure 1.13 Liquid jet produced by electric charge; and b) liquid jet produced by laser radiation (Fletcher and Palanker, 2001; Menezes *et al.*, 2006)

1.8 Research Objectives for Improving Liquid Jet Injection

Given the many uses of liquid jet injection, the objective of this research is to improve current techniques for the controlled release of micro jets. Studies have illustrated that liquid micro jets offer a way of applying new forms of drug therapies as well as offering clinicians localized treatment of different diseases that cannot be accomplished using conventional methods. Commercial versions of such liquid jet injectors have suffered from a lack of pressure control, accuracy and repeatability. Prototype devices that exhibit dynamic closed-loop control are only in the experimental stages. Consequently, it is necessary to further develop the devices and fundamental science governing these jets to improve usability. This is essential for precisely controlling penetration depth as well as the volume of fluid that is delivered.

To further the current state of liquid jet injectors, the research work will focus on the following four objectives and contributions:

➢ Validation of a CFD model to characterize jet shape and pressure, based on fluid properties and injector design, and subsequently determine the effects of viscosity on power source requirements;

➢ Design and development of a prototype injector for full closed-loop control, which offers real-time pressure control and does not require the use of a model that considers forces acting on the plunger;

➢ Design and analysis of a combustion-driven injector, to characterize the use of a detonation wave as a means of overcoming the high initial impulse requirements of liquid jet injection and delivering medication with more viscous consistencies;

➢ Develop a conceptual screw driven injector which is capable of decoupling the power source from the plunger in order exhibit the energy release and scalability of a detonation driven device, with the controllability of and precision of closed loop servo control.

1.9 Author's Contribution

The research work presented in this thesis has led to the advancement of scientific knowledge pertaining to liquid jet injectors on four specific fronts, outlined in the aforementioned section. The work has resulted in various journal articles as well as conference proceedings. The contributions made in this research are described below.

Chapter 2 describes a study pertaining to the analysis of the requirements for power sources used for viscous liquid jet injections. This study resulted in a peer reviewed conference proceeding entitled "*Optimization of Drug Viscosity Used In Gas-Powered Liquid Jet Injectors*" at the 37th Annual International Conference of the IEEE Engineering in Medicine and Biology Society (Portaro *et al.*, 2015), as well as a conference bulletin at the 70th annual meeting of APS Division of Fluid Dynamics (Portaro *et al.*, 2017). In this study a CFD model was jointly developed by Portaro and Nakayama (Nakayama *et al.*, 2015), whereby Nakayama created a CFD model and Portaro created a model to characterize the delivery process of an air-powered liquid jet injector. This is subsequently used by Portaro to quantify the change in jet stagnation pressure as a function of viscosity. The results from this study are then compared by Portaro to experimental results to verify the validity of the numerical model and the role viscosity plays in the injection process.

Chapter 3 focuses on the development and analysis of a servo tube-powered liquid jet injector created by Portaro. This entails the design, analysis, manufacturing, and testing of the prototype injector presented in this study. The device made it possible to control the jet injector's delivery pressure in real-time. This study has led to a journal paper entitled "*Design and Analysis: Servo Tube Powered Liquid Jet Injector for Drug Delivery Applications*" accepted for publication in Applied Sciences (Portaro and Ng, 2022) and has also been presented at 70th Annual Meeting of the APS Division of Fluid Dynamics, entitled "*Analysis of high-speed jets produced by a servo tube driven liquid jet injector*" (Portaro and Ng, 2017).

Chapter 4 highlights the development and analysis of a combustion-driven, liquid jet injector. This prototype was created in response to the study conducted in **Chapter 2**, which illustrated an increased power requirement for viscous injections. This resulted in the creation of a simplified device capable of providing greater power than other gas-driven injectors, for delivery of higher viscosity injectables. In this study, Portaro conducted the design, analysis, manufacturing, and testing of the prototype injector. This resulted in a publication entitled "*Controlled release using gas detonation in needle-free liquid jet injections for drug delivery*" in Applied Sciences (Portaro *et al.*, 2019). The research was also presented as the "*Design and analysis of a detonation-driven mechanism for needle-free liquid jet injection*" at the 71st Annual Meeting of the APS Division of Fluid Dynamics, in Atlanta.

Chapter 5 presents a novel concept for a NFJI, that utilizes a screw mechanism, an ultra-low inertia servo motor as well an electromagnetic clutch to provide high powered liquid jets, with real-time controllability. This chapter utilizes the knowledge base acquired in the previous sections and provides a concept that displays the benefits of both technologies and is scaled in a practical form factor for clinical use.

Chapter 2 : Power Source Requirements for Viscous Liquid Jet Injection

2.1 The Importance of Viscosity for Liquid Jet Injection

Most studies conducted on liquid jet dynamics and corresponding power source behavior of liquid jet injectors deal with fluids which exhibit low viscosity. However, the injectable drug market is continually innovating to provide highly concentrated formulations with better efficacy. These new drug therapies, such as DNA therapy necessitate the delivery of fluids with viscosities much greater than 200 cP (Rohilla *et al*., 2019). Furthermore, nucleic acid vaccines, such as the mRNA vaccines developed to combat COVID-19, have different rheological properties than those of commonly used injectables. Consequently, it is necessary to conduct a study which examines the effect of liquid properties, on the dynamics of liquid jet injection. This will be accomplished by utilizing a CFD model to analyze the injection process with fluid of varying viscosity.

2.2 Physical Prototype and Numerical Model

The CFD model used in this study is based on the work conducted by Nakayama *et al.* (2015), which addresses the modeling of high-speed jets emanating from air-powered injectors using two fluid phases. The research focuses on the fluid dynamics of the high-speed jets emanating from an air-powered, needle-free injector and analyzes the effect of injector nozzle size, driver pressure and fluid viscosity on the jet injection process. The numerical simulations for this model are carried out using the OpenFOAM® CFD software package (OpenCFD, 2013). Furthermore, the geometry used in the CFD analysis is equivalent to that of a custom-built air-powered injectors produced by Portaro and Ng (2015). The premise behind using an air-powered device as the basis for this study is twofold. The air-powered device represents the majority of commercially available units, and the findings can then be applied to this market segment. Secondly, the prototype injector has already been well characterized in previous studies, which yields a higher degree of confidence when conducting experimental work. **Figure 2.1** illustrates the basic construction and dimensions of the prototype injector.
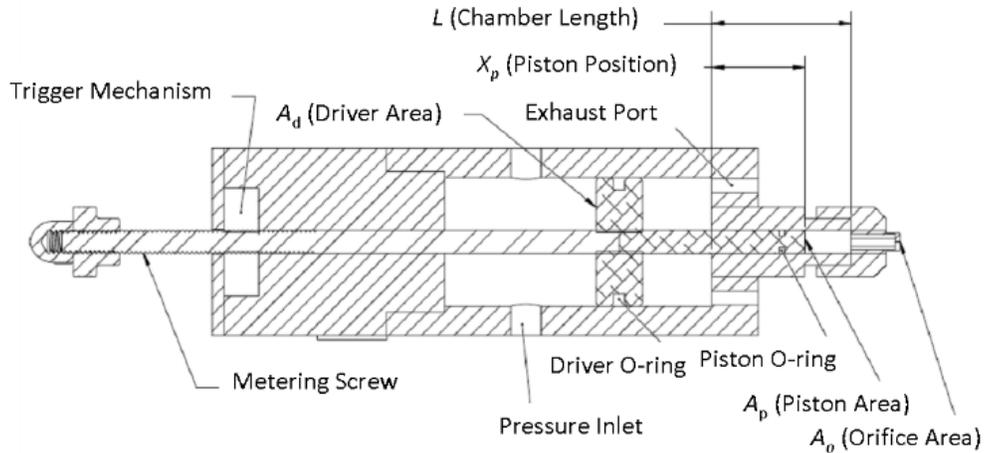
Figure 2.1 Schematic of custom air-powered injector (Portaro and Ng, 2015)

The device consists of a driver chamber containing high-pressure gas, a moving piston with O-rings, an injection chamber containing the liquid and an orifice-type nozzle. High-speed jets are emitted into the air through the orifice. Some important dimension and operating characteristics of the experimental prototype injector are summarized in **Table 2.1**.

Injector Parameters	
Nozzle Diameter	100 μm - 300 μm
Driver Pressure	3 bar - 10 bar
Injection Volume	0 ml - 1.2 ml
Piston Diameter	6.35 mm
Driver Diameter	38.1 mm
M_p (Mass of Piston-Driver Assembly)	80 g

Table 2.1 Properties of experimental air-powered injector (Portaro and Ng, 2015)

In this study an axis-symmetric geometry illustrated in **Fig. 2.2**, is used for defining the spatial geometry of the driver and injection chamber as well as the orifice and atmospheric region. The piston, driver chamber, and O-ring frictional forces are modeled as a two-dimensional moving wall, located at the left-hand boundary, with a dynamic model that utilizes the analysis of Portaro and Ng (2015).
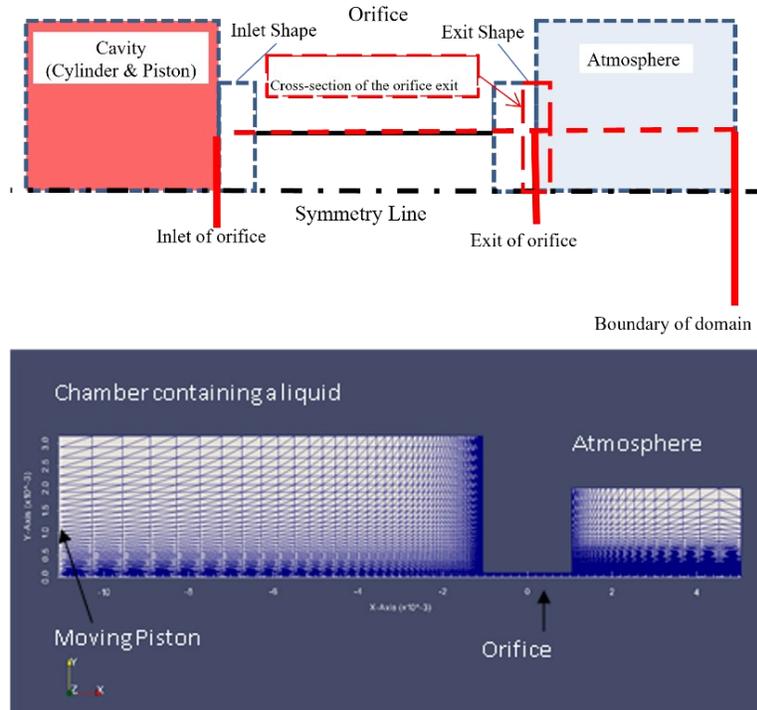
Figure 2.2 Axis-symmetric geometry of numerical simulation

2.2.1 Moving Wall Model

The dynamics of the injection process is realized by using grid movement to abruptly impact the boundary of the injection chamber. The grid motion is prescribed by the velocity imposed by the driver piston on the plunger, and is obtained by solving an ordinary differential equation derived from a force balance based on Baker and Sanders (1999) at each computational time step. For the numerical model utilized in this study the following assumptions are introduced:

 ➢ The piston is a solid body (i.e., no deformation occurs) and its mass is constant;

 ➢ The thickness of the piston is neglected (assumed as a two-dimensional object);

 ➢ Back leakage of liquid through the gap between the O-ring and the inner surface of the cylinder is neglected;

 ➢ Gravitational force is neglected.

During the injection process, the piston is pushed by the high-pressure gas contained in the driver portion, and impacts the liquid inside the chamber. However, the injection chamber liquid generates a backward force as the fluid is being compressed. Furthermore, the friction force between the O-

rings and the inner surface of the cylinder should be taken into consideration during the motion. As a result, the piston motion is determined by the sum of the driver force generated by the gas pressure inside the driver chamber, the pressure of the injection fluid, and the O-ring friction force (Chen *et al.*, 2011; Portaro and Ng, 2015), i.e.,

$$\frac{d^2 x_p}{dt^2} = \frac{F_D(t)}{m_p} - \frac{A_p p(t)}{m_p} - \frac{F_f(t)}{m_p}$$

Eq. (2.1)

where F_D and F_f are the driving force and frictional force, and $p(t)$ is the fluid pressure on the piston boundary. The mass and surface area of the piston are represented by A_P and m_p respectively. The initial conditions for the piston, which at the beginning of an injection is initially at rest, correspond to $t = 0$, $x_p = 0$, and $dx/dt = 0$. For an air-powered injection system, the driving force F_D which moves the plunger forward is produced by pressurizing the driver chamber. The pressure within the driver chamber can be modeled by using the ideal gas law and the initial driver chamber pressure. The pressure within the chamber can be computed as a function of driver displacement, i.e.:

$$p_d = \frac{mRT}{V_D(t)}$$

Eq. (2.2)

with

$$V_D(t) = (L_o + x_p(t)) A_D$$

Eq. (2.3)

Equation 2.3 underlines that this model represents a case where the injection chamber contains a fixed amount of gas, such as in a disposable air-powered injection device. The case of a reservoir or pressurized line fed injectors would be handled by assuming p_d = constant. As the driving force begins to move the piston forward, there is resistance created by the atmospheric pressure, p_a, acting on the opposite side of the driver face. This force can be assumed to remain constant throughout the injection process and is simply the product of atmospheric pressure and the driver area, yielding:

$$F_D(t) = A_D \left(\frac{mRT}{V_D(t)} - p_a \right)$$

Eq. (2.4)

The frictional forces within the mechanism counteract and dampen the movement of the driver/piston assembly. The friction is caused by the O-ring seals which make contact and rub against the inner walls of both the driver chamber and the injection chamber. In order to model the O-ring friction it must be broken down into two components: the first consists of the friction force

caused by the compression fit of the O-ring into its housing, the second is a result of the thin fluid film which is generated in the clearance gap between the two components that the O-ring must seal. The forces caused by the compression of the O-ring, in the barrel of the injector are also dependent on the force generated by the pressure of the fluid. Consequently, the two major forces causing O-ring friction must be coupled to accurately model friction. Using the concepts from tribology (Chen *et al.*, 2011; Portaro and Ng, 2015), the fluid pressure imposed on the O-ring can be approximated by applying the Reynolds equations.

$$\bar{p}_{O-ring} \approx \frac{1}{2} \frac{6\mu U(t)}{h^2} \frac{d}{2} + p(t) \qquad \text{Eq. (2.5)}$$

As a result of knowing the pressure imposed by the fluid on the O-ring seal, the resisting force caused by this pressure is simply the area of exposed O-ring multiplied by the corresponding pressure, i.e.,

$$F_{fluid} = \bar{p}_{O-ring} \pi Dh \qquad \text{Eq. (2.6)}$$

The amount of compression fit κ as a function of load that an O-ring will produce can be found in empirical charts (Darcoid Norcal Seals). In addition to the force caused by the compression of the O-ring into the barrel of the injector, it is also necessary to take into consideration the transfer of forces caused by the fluid pressure on the O-ring. The fluid pressure that acts on the seal also serves to further increase the compression loading. Studies conducted by Guang and Wang (1994) demonstrate that the transfer coefficient between the fluid pressure acting on a seal in relation to the increase of compression force of the O-ring can be estimated at unity. In other words, the pressure contained within the thin film acting on the seal almost entirely serves to increase the amount of compression forces on the sealing surfaces. Knowing that the coefficient of friction between aluminum and nitrile rubber is $\alpha = 0.2$ (Chen *et al.*, 2011; Portaro and Ng, 2015), the resisting force encountered by individual O-ring seals in the injector can be completely described through Eq. 2.7:

$$F_f(t)_{O-ring} = \left(\alpha \cdot \bar{p}_{O-ring}(t)\pi Db\right) + \left(\bar{p}_{O-ring}(t)\pi Dh\right) + \alpha \cdot \kappa \qquad \text{Eq. (2.7)}$$

During computation, the piston position/velocity as a function of time can be obtained by solving Eq. (2.1) together with Eq. (2.2) through Eq. (2.7), simultaneously with the CFD solution. These equations govern the equation of motion of the piston and are incorporated into a class in

OpenFOAM. **Figure 2.3** illustrates the behavior of the piston from sample simulations showing the maximum piston velocity occurring at the very beginning before the frictional forces and fluid forces can dampen the motion. The oscillatory nature of the piston displacement is expected as the system is underdamped. In the limiting case where there is no frictional loss (i.e. no O-ring force), the injection fluid pressure must exceed the driver chamber pressure for the piston to slow down. Hence, the piston location always reaches a local maximum when there is a net force backward and inversely for local piston location minima.
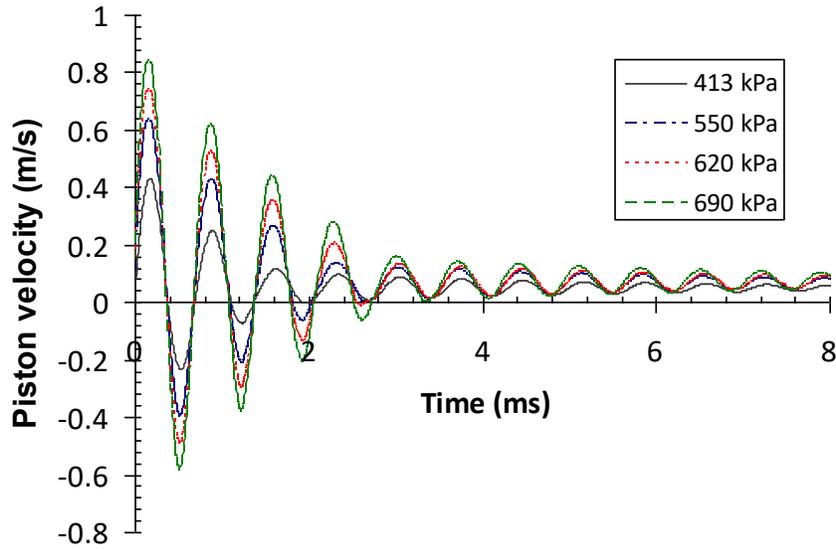
Figure 2.3 Piston velocity as a function of time

The O-ring frictional force is related to the magnitude of the piston velocity and cannot overdamp the system. Using the piston position/velocity as boundary conditions, a Laplace equation related to the mesh motion, as illustrated in **Fig. 2.4**, is solved to determine a new mesh using the dynamic mesh classes in OpenFOAM, i.e.,

$$\nabla \cdot \left(\gamma \nabla u_m \right) = 0$$
Eq. (2.8)

where γ can be considered constant or variable diffusivity and u_m is mesh motion velocity or mesh point displacement.

30
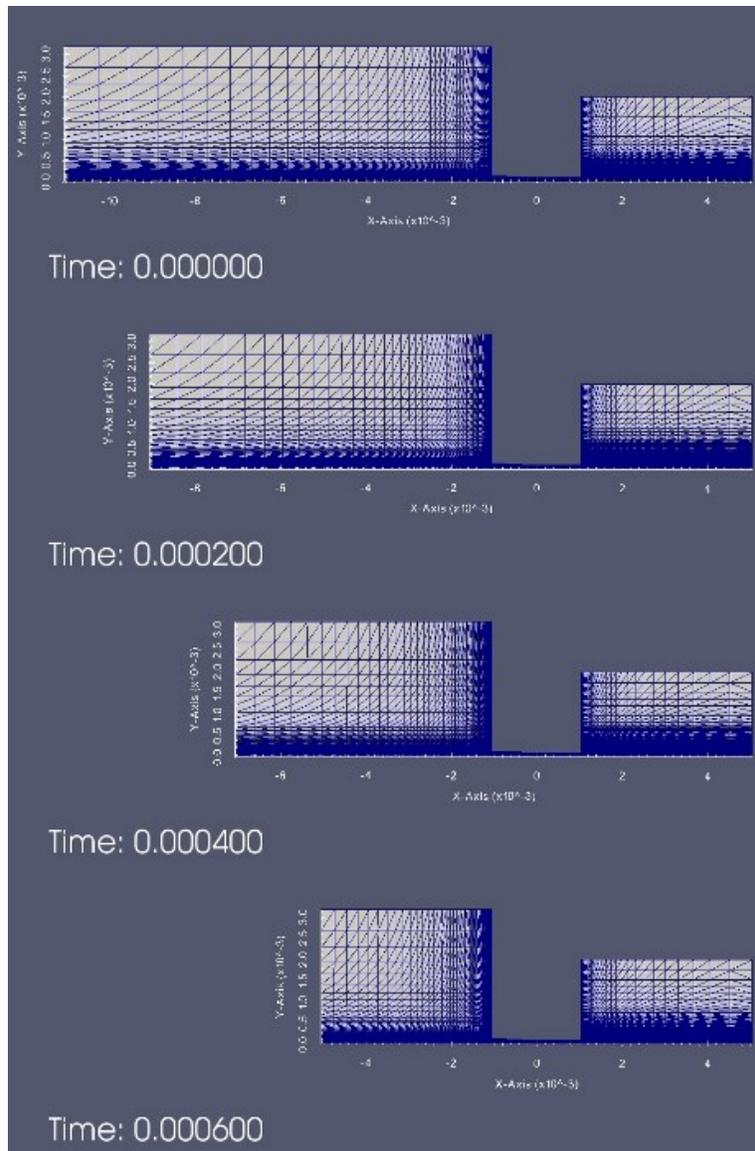
Figure 2.4 Piston mesh motion as a function of time

2.2.2 Fluid CFD Model Description

Physical dimensions and average gird size for each domain are summarized in **Table 2.2**. It is noted that the average cell size given in the table is for the base mesh case and the grid is in fact refined near the orifice inlet/exit to capture steep gradient of pressure, velocity and volume fraction of liquid. The structured mesh is generated by a built-in utility in OpenFOAM. The domain boundaries have zero gradient Neumann conditions for the liquid volume fraction, the sub-grid scale (SGS) stress, pressure, temperature and non-slip condition on velocity. The Dirichlet condition is applied for the SGS turbulent energy and a fixed total pressure (i.e., 101,325 Pa) is imposed on the atmosphere exit boundaries.

31

Domain Name	Radius (y- coordinate)		Length (x- coordinate)	
	Dimension	Average Cell Size	Dimension	Average Cell Size
Chamber	3.175	0.064	10	0.20
Orifice	0.1	0.001	2.1	0.04
Atmosphere	2	0.033	4	0.16

Table 2.2 Geometric grid properties of numerical simulation

For the fluid properties, the two fluid phases are initially divided into a liquid phase in the chamber/orifice and a gas phase in the atmosphere region. The gas density is simply specified by using the ideal gas formula for the air to cope with the compressible flow field. In the injection chamber and orifice, complications arise by specifying the water as a compressible liquid, thus variable density is specified. In Eq. (2.9), the variables p and ρ are the liquid pressure and density, respectively. The compressibility ψ and the bulk modulus of elasticity of liquid B are a function of pressure and temperature. These are updated after solving the energy equation (Eq. 2.10) at each time step. Then, the density is updated in the linearized equation (Eq. 2.11) during the simulation. Subscripts 0 and 1 denote the respective quantity at the initial and current time.

$$\frac{\partial \rho}{\partial p} = \frac{\rho}{B} = \psi \qquad \text{Eq. (2.9)}$$

$$\frac{\partial(\rho T)}{\partial t} + \nabla \cdot (\rho U T) - \nabla \cdot \left(\frac{k}{C_v}\right) \nabla T = \frac{p}{C_v} \nabla \cdot U \qquad \text{Eq. (2.10)}$$

$$\rho_1 \approx \rho_0 + \psi(p_1 - p_0) \qquad \text{Eq. (2.11)}$$

The Volume-of-Fluid (VOF) method is then used to update the position of the interface between two phases by computing the transport equation for the liquid volume fraction as the indicator function to locate the interface.

$$\frac{\partial(\rho \alpha)}{\partial t} + \nabla \cdot (\rho U \alpha) = 0 \qquad \text{Eq. (2.12)}$$

with the liquid-phase volume fraction α,

$$\alpha = \begin{cases} 0 & \text{for a cell inside the gas} \\ 0 < \alpha < 1 & \text{for a cell inside the transitional region} \\ 1 & \text{for a cell contained completely the liquid} \end{cases}$$

By determining the volume fraction α, the local properties of the fluid are computed based on the single state of each phase, i.e., the local density ρ and the local viscosity μ of the fluid are interpolated across the interface as follows:

$$\rho = \alpha \rho_l + (1 - \alpha) \rho_g$$
$$\mu = \alpha \mu_l + (1 - \alpha) \mu_g$$

Eq. (2.13)

where the subscripts l and g denote the liquid- and gas-phases, respectively.

The governing equations of the phenomenon consist of the transport equations for conservation of mass and momentum of a two-phase flow system, comprised of two immiscible, compressible Newtonian fluids, including surface tension (OpenCFD, 2013). The finite volume method with 2nd order accuracy is used to discretize the governing conservation equations. Large Eddy Simulation (LES) is applied for the turbulence model. The solver used to compute the solutions of the discretizing equations follows the PISO-SIMPLE (PIMPLE) algorithm (Barton, 1998; Ferziger and Peric, 2004). In the unsteady flow solution, the time step size, Δt, of $1 \times 10^{-8} \sim 5 \times 10^{-9}$ s is selected to obtain stable solutions. In OpenFOAM, the combination of compressibleInterFoam and oneEgEddy realizes the above models as multi-phase Navier–Stokes solver (thus simulating viscous fluids in the injection chamber and the air) and LES model, respectively.

The model delivered pressure traces which exhibit very close agreement to output from the custom-built, air-powered injector mentioned above. **Figure 2.5** depicts an overlay of both the experimental trace and the CFD counterpart, utilizing a 200μm nozzle and 4.13 Bar delivery pressure. The model captures the peak as well as the mean stagnation pressure. **Figure 2.6** illustrates a very good correlation between the CFD model and the prototype tested over a wide range of pressures and nozzle sizes.
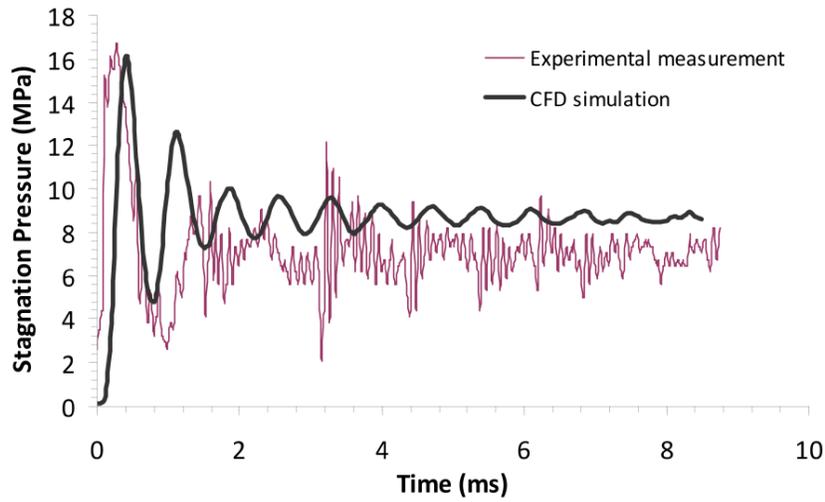
Figure 2.5 Comparison of experimental and numerical traces
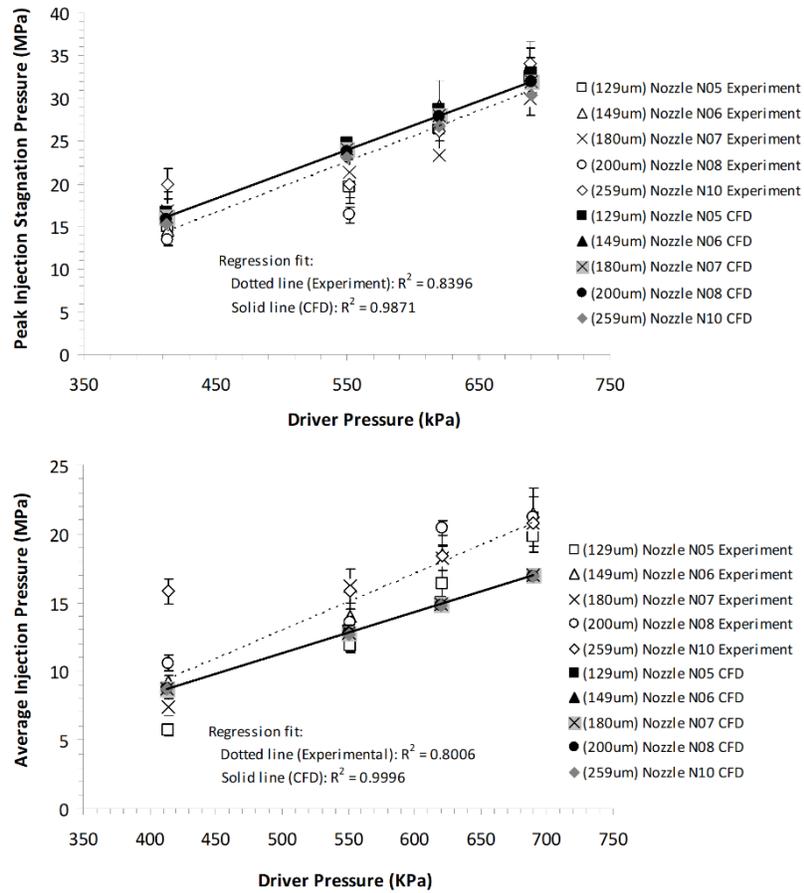
Figure 2.6 Correlation between experimental prototype and CFD model

2.3 Numerical Results

This study utilized the previous model to explore the effects of varying the viscosity of the fluid and observing the CFD results for changes in pressure trace behavior as well as physical jet shape. The viscosity was increased over 8 different values ranging from .9 cP to 87 cP and values of viscosity corresponding to the different physical equivalent of aqueous-glycerol solutions were chosen. This will later provide test points that can be verified numerically.
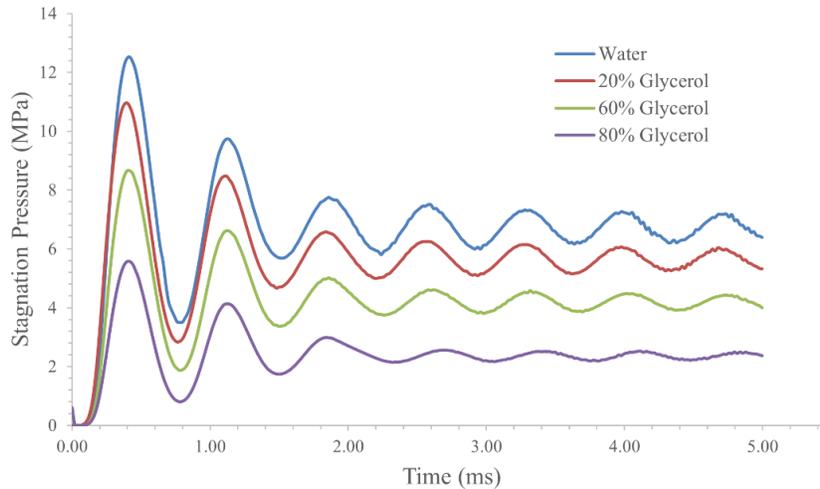
Figure 2.7 Stagnation pressure as a function of time for differing viscosity

The validity of the initial numerical results is verified by utilizing the custom-built, air-powered injector described in the previous section. In order to mimic fluids of differing viscosity, aqueous glycerol mixtures of different weight percentages were formulated. These were then tested then using a driver pressure of 6.9 bar, and a 200 μm nozzle. The pressure traces were captured via PCB Piezotronics force transducer, depicted in **Table 2.3**, coupled to a Rigol DS1102E digital oscilloscope with 1G Sa/s.

PCB 209C11 Force Transducer	
Measurement Range	.00979 kN
Sensitivity	494.60 mv/kN
Lower Frequency Response	.5 Hz
Upper Frequency Response	30 kHz
Temp Range	-54 to 121 °C

Table 2.3 Properties of force transducer used to capture pressure traces

The numerical model was analyzed for its ability to produce pressure waveforms similar in nature to those obtained by the air-powered prototype. **Figure 2.8** illustrates an overlay of an experimental and CFD injection driven at 6.9 Bar, with a fluid viscosity of 4.0 cP, which corresponds to approximately a 40% wt. aqueous solution of glycerol. The results demonstrate the model's ability to predict the peak and mean stagnation pressure. It also demonstrates, in this case, that it can also closely map the amplitude and frequency of the oscillations. If a time slight time shift of .5 ms is performed in **Fig. 2.8**, then the timing of the injection also seems to be well predicted.
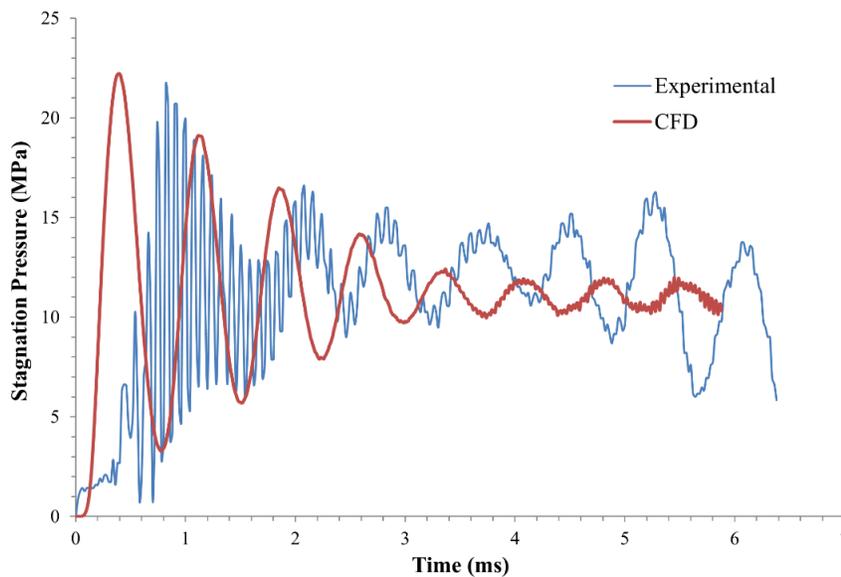
Figure 2.8 Comparison of CFD and experimental pressure output for 4.3 cP viscosity

Figures 2.9 and **2.10** illustrate the ability of the numerical model to predict both peak and average stagnation pressure. The model seems to accurately predict the mean with a maximum difference of 14% when compared to its numerical counterpart. The peak pressures exhibit more variability, although it follows the trend outlined by the numerical model, in general the maximum difference observed is approximately 23%. The results of the preliminary experimental study suggest that the numerical model developed by Nakayama *et al.* (2015), can be accurately used to observe the effects of fluid properties. It is also important to note that while predicting an accurate absolute value of stagnation pressure is important, the ability to use this model for guidance on the requirements of power sources for injecting various fluids is of greater value.
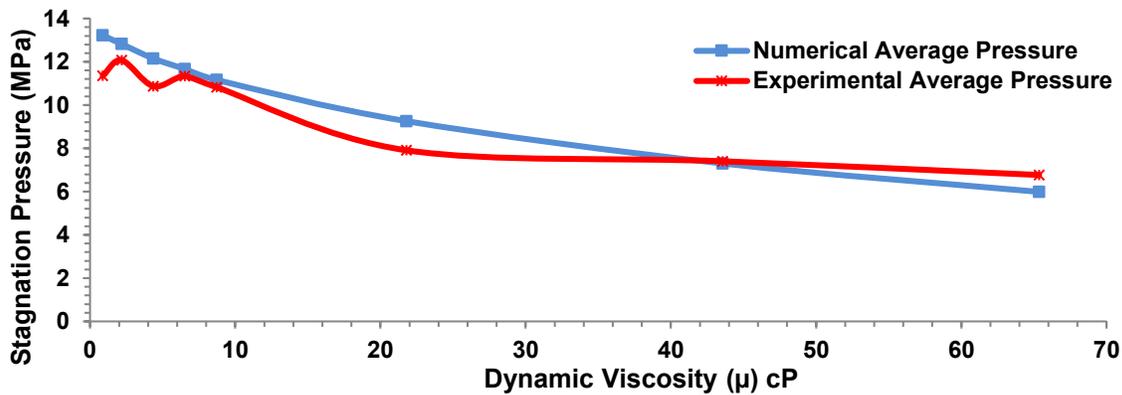
Figure 2.9 Comparison of CFD and experimental results for peak stagnation pressure
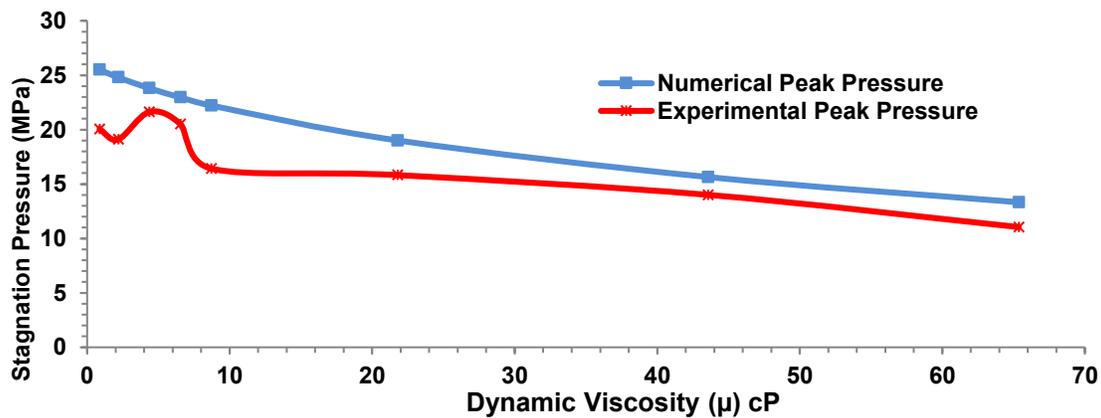
Figure 2.10 Comparison of CFD and experimental results for average stagnation pressure

Figures 2.7 through **2.10** make it possible to draw several important conclusions. As theorized, the stagnation pressure both peak and average decrease as the viscosity increases, and the pressure rise time seems unaffected by viscosity, which is an important aspect of creating enough initial pressure to puncture tissue. Furthermore, the magnitude of the oscillation seems to decrease with increasing viscosity, and can be explained by the additional damping the viscous fluid provides within the injection chamber. This phenomenon will however be difficult to verify experimentally, as the piezoelectric-based transducers seem to exhibit noise at the time scales illustrated above.
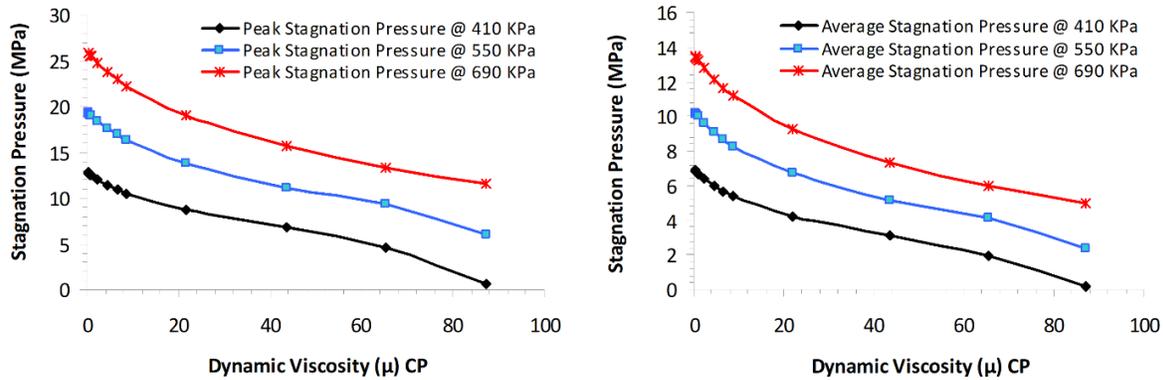
Figure 2.11 Peak and average stagnation pressure as a function of dynamic viscosity

Figure 2.11 depicts the variation of both peak and average stagnation pressure as a function of dynamic viscosity. These results indicate that for increasing viscosity the stagnation pressure decays in a non-linear manner. From the numerical results, it appears that both peak and average stagnation pressures exhibit a maximum of 16% decrease with viscosities 10 times those of water (0.87 cP). New emerging drug formulations can have viscosities in excess of 200 cP, this poses a particularly difficult situation for gas-powered devices. The maximum power available is predetermined by the pressurization of a fixed mass of gas, for safety reasons this is usually kept below 8 bar. Spring-powered injectors can however be altered to accommodate the added force requirement with springs exhibiting greater spring constants. This will however attain a practical limit as the devices necessary to initially charge the injector will be unpractical. One important attribute, displayed in **Fig. 2.12**, is the percent (%) difference in peak and average stagnation pressure as viscosity increases between different driver pressures. It is observed that as the driver force is increased the corresponding difference between peak and mean stagnations pressure is less sensitive to the increase in viscosity.
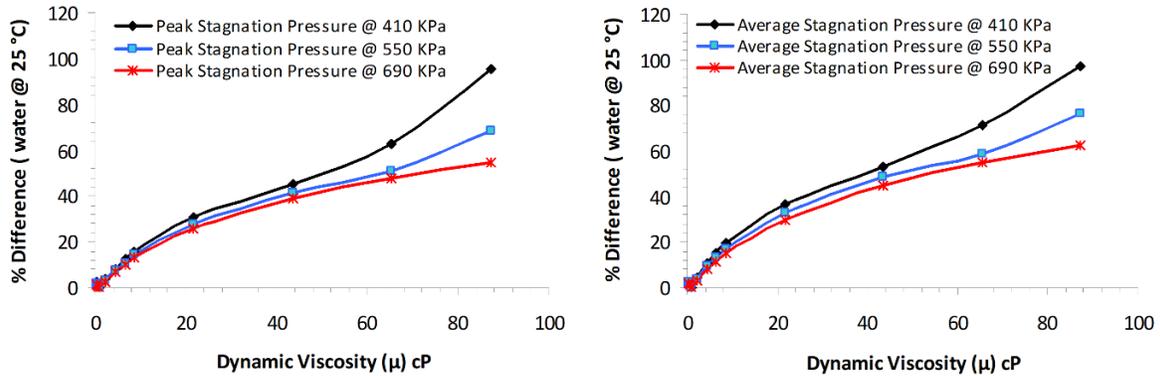
Figure 2.12 Percent difference in peak and average stagnation pressure as a function of viscosity

Figure 2.13 illustrates the behavior of the Reynolds number with increasing viscosity. The results seem to indicate that a tenfold increase in viscosity from that of water causes a significant decrease in the Reynolds number. This is indicative of the role that viscous forces play in counteracting the inertial force created by the driving pressure. This helps confirm the notion that power sources with greater instantaneous energy release must be explored as a means of delivering viscous formulations.
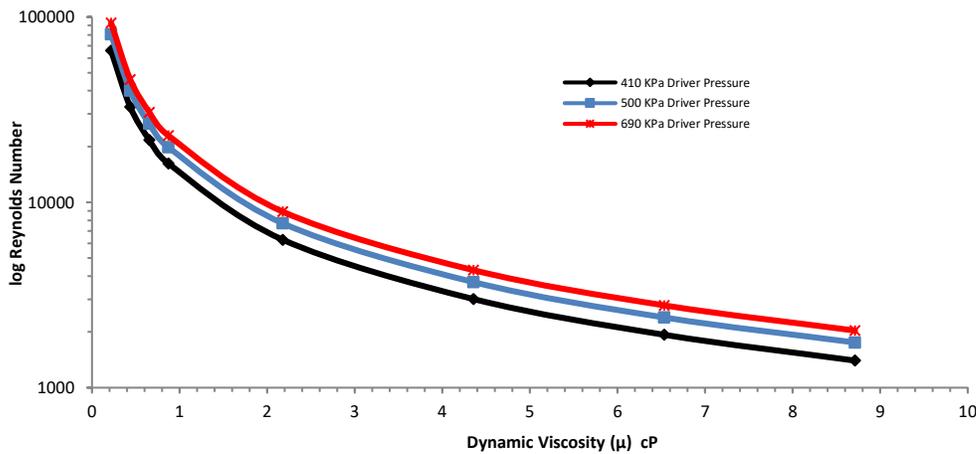
Figure 2.13 Reynolds number as a function of viscosity

The increase in viscosity also aids in jet confinement, this is observed in **Fig. 2.14**, whereby a jet with the viscosity of water at room temperature is compared to that of a jet with a 10 times greater viscosity. Both exhibit a similar frontal curvature caused by the shearing of the frontal portion of

39

the jet as it emerges into the atmosphere. However, the jet of greater viscosity exhibits greater confinement along its axis than its counterpart. This is an important notion, typically when administering a liquid jet injection, the frontal curvature is not present, due to its immediate contact with the skin, and only the jet's ability to resist shearing along its central axis is of importance. The viscous column will have less tendency to splash back due to greater shearing forces between the interface of the punctured hole and the free surface of the jet.
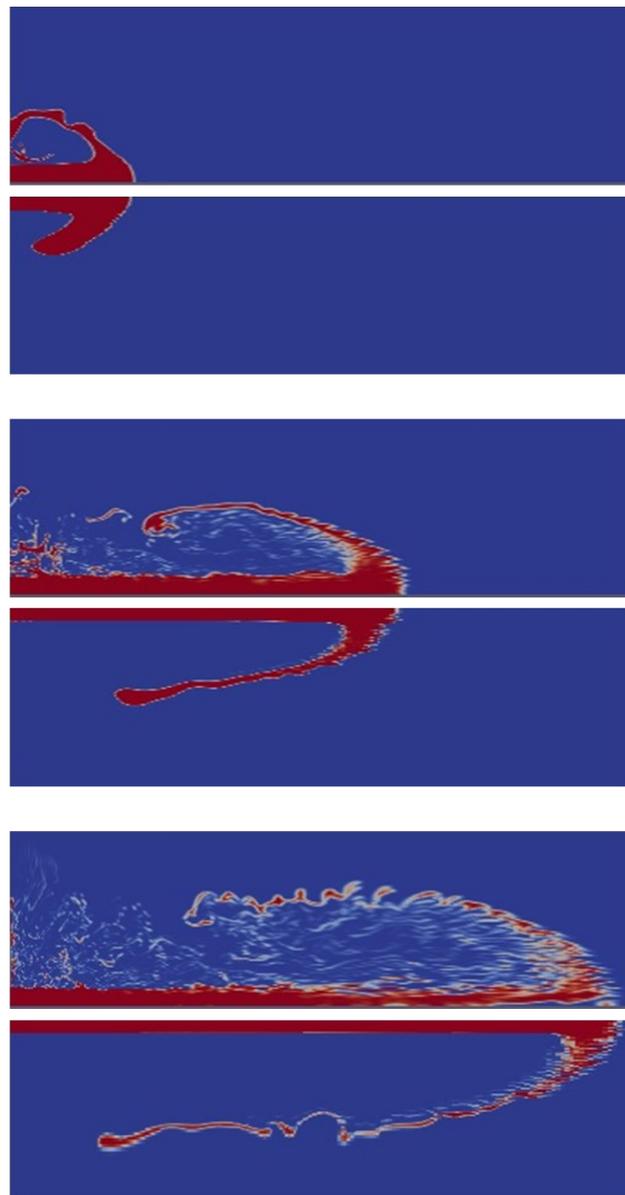
Figure 2.14 a) Time evolution of 0.87 cP; and b) 87 cP jet emanating from 200 μm nozzle at 410 kPa driver pressure

2.4 Summary

The numerical model utilized for this work has shown great promise in predicting both peak and average stagnation pressures. The results demonstrate that as the viscosity of injectate is increased the driver force requirements increase in a non-linear manner. Furthermore, this model can be used in future work to verify the effects of recently developed drug therapies, which not only exhibit viscosities greater than 200 cP, but also exhibit non-Newtonian shear-stress behaviour. The model can be easily tailored to account for the different rheological properties. It is also important to note that future iterations of the model should consider the temperature gradients across the nozzle orifice caused by intramolecular shear. The temperature increase has been studied by Williams *et al.* (2019), it was shown that increases of up to 65 °C were obtained on the nozzle wall, as well as an increase of up to 2.5 °C once the jet emerges from the nozzle. Considering the effect of temperature across the orifice, when dealing with viscous simulations can help increase the accuracy of the numerical simulations. The model also lends itself well for studying and validating different types of power sources. Although an air-powered injector was used in this model, the forcing term and the plunger velocity can easily be modified to model alternative types of power sources, such as controllable power sources described in **Chapter 3**.

Chapter 3 : Design and Analysis of Servo -Tube Powered Liquid Jet Injector

3.1 Importance of Dynamic Stagnation Pressure Control

The current state of commercially available needle-free liquid jet injectors offers no way of controlling the output pressure of the device in real-time, as the driving mechanism for these injectors provides a fixed pressure delivery profile. In order to improve the delivery efficiency as well as the precision of the targeted tissue depth, it is necessary to develop a power source that can accurately control the plunger velocity. The duration of a liquid jet injection can vary from 10 to 100 ms and generate acceleration greater than 2g, thus a platform for real-time control must exhibit a response time greater than 1 kHz and good accuracy.

The objective of this study will be to design and manufacture a prototype injector that can provide a platform capable of shaping the real-time jet injection pressure profile so that it can later be tailored for more efficient drug delivery. The success of this initial prototype and subsequent study will be based on the following criteria:

- The prototype injector must exhibit accurate real-time control of the jet stagnation pressure, as well as provide enough power to penetrate human tissue;
- The ability to dynamically react to external variables, such as friction, fluid viscosity, nozzle size and temperature deviations. This must be accomplished without the need to rely on mathematical models to predict the device's output, but rather compensate for them using a control loop;
- The ability to produce large volume, viscous injections and demonstrate a satisfactory level of completeness of injection with minimal backsplash.

3.2 Lorentz Force Injectors

A thorough literature review has led to the conclusion that <u>electronic linear actuators</u> provide one of the most practical and efficient methods for complete closed-loop control of liquid jet production. They offer real-time control and do not require high voltages or subject the fluid to electric charges or laser radiation as in other experimental techniques. This technology has been applied to an experimental device proposed by Taberner *et al.* (2011), whereby a Lorentz force

actuator, based upon a voice coil, is used to compress a column of fluid, using a plunger traveling at a specified velocity profile. The results of this study illustrated that a semi-closed-loop system consisting of a simple coil/ one magnet actuator coupled to a linear variable differential transformer (LVDT) could successfully be used to dynamically shape a pressure profile. Although the system produced controllable traces, there is a lack of information on its precision. In fact, a study published by Chen *et al.* (2011) seems to indicate that there is still a difference between the plunger velocity profile prescribed to the actuator and the expected pressure output at the nozzle.

The design of the Lorentz force actuators used in these studies is based on simple voice coils, which have some significant drawbacks. This is revealed by examining the fundamental principles governing the force output of these actuators. In its simplest form a voice coil can be considered a non-commutated DC motor, having one winding and one permanent magnet. In the case of the linear actuator utilized by Taberner *et al.* (2011) the permanent magnet is chosen as the stationary component, with the coil providing motion. The force output is prescribed by $F = B \times i$, where F is the force (N), B is the magnetic field flux (T) and i is the current (A) flowing through the coil. From **Fig. 3.1** it is possible to see that the magnetic field produced by the magnets permeates the air gap and is orthogonal to the coil, and thus produces a force, known as the Lorentz force, first described by Hendrick Lorentz in 1895, that is prescribed by the cross-product of the magnetic field flux and the current energizing the coil.
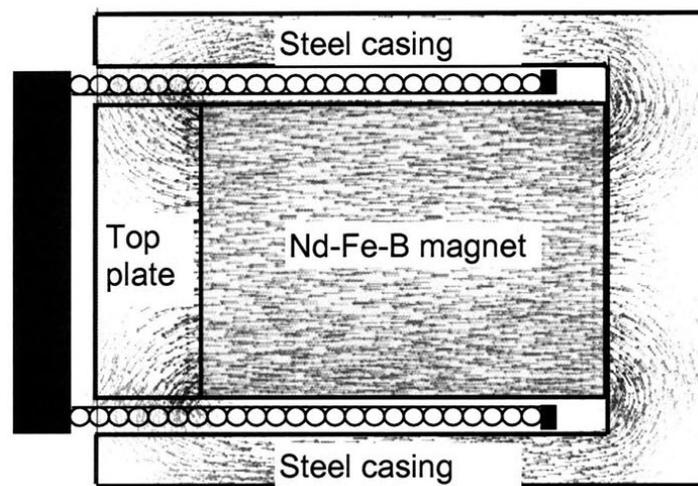
Figure 3.1 Magnetic field flux of voice coil actuator (Ball, 2007)
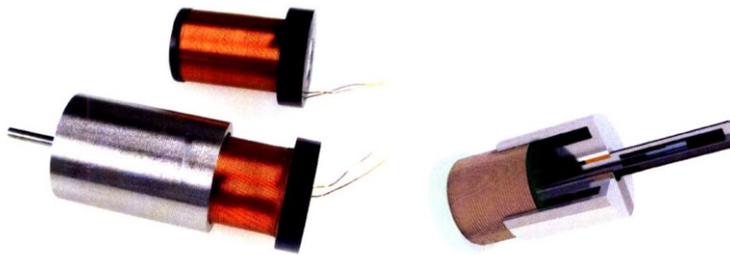
Figure 3.2 Typical construction of voice coil actuator (Ball, 2007)

In an ideal scenario the motor constants for liquid jet injection should exhibit an independent relationship between current, speed, position and temperature. However, because of the inherent construction of this type of motor, whereby only one coil can be energized, the velocity and force of the plunger on this type of actuator are dependent on the amount of current that is passed through the coil. This means that an increase in force will be accompanied by a proportional response in the speed of the plunger. When voltage is applied to the coil, the magnetic flux, forces the coil to move in the direction normal to current flow, this motion will happen so long as the coil is energized. In order to provide precise motion a control loop is created through the use of an LVDT, which returns the plunger's position as a function of time. The feedback from the LVDT is used in conjunction with a PID loop controlling both the magnitude and polarity of the voltage sent through the coil ensuring that proper plunger position is accomplished. The control loop must exhibit a relatively high-frequency response rate, in order to ensure the plunger is following the proper trajectory given that injections take place within milliseconds and the stroke of the plunger can be on the order of several centimeters depending on the volume of liquid delivered.

However, when precise velocity control is required and the voice coil encounters higher forces, due to the coupling between force and velocity it becomes difficult for the control loop to follow the proper trajectory. This is a very important notion as the health care industry moves towards adopting newer technologies such as DNA therapy, with more viscous formulations and larger injection volumes, the demand for the power sources for needle-free injectors will grow (Raviprakash and Porter, 2006; Kendall, 2006). Although voice coils exhibit very good high-speed response, increasing power output becomes difficult. Power output can be increased by either increasing current or the magnetic field flux. This is usually accomplished by using more powerful

and larger magnets, applying more current, which entails using larger coils, or diminishing the air gap between the magnet/coil. It should also be noted that optimizing a voice coil motor for power will inevitably affect the response times of the system, as larger magnets/coil assemblies represent larger moving masses of greater inertia, and higher currents. This will require more powerful electronics and as current increases the switching frequencies of control electronics decrease. Furthermore, Ruddy *et al.* (2017) found that the coupling between voice coil stroke, size, and efficiency interacts with the mechanics of pressurizing a fluid in a piston-cylinder apparatus to give a scaling law. For a given input power, the required voice coil mass grows faster than the injection volume, with $M \propto V^{6/5}$. As a result, hand-held injectors delivering volumes of over 0.5 mL are not practical using voice coil actuation Moreover, the voice coil design does not lend itself well for large travels meaning that providing repeated large volume injections as required by mass vaccination in the animal health industry would not be feasible.

3.3 Servo Tube Actuated Design

In order to improve on the shortcoming of voice coil motors and to provide a platform with greater controllability, it is necessary to use a linear actuator with a slightly different topology. This study will examine the use of a classical 3-phase linear motor consisting of three fixed coils and multiple permanent magnets, whereby each coil is controlled individually, i.e., commutated in respect to the permanent magnets. The motor chosen for the construction of a prototype injector is provided by Dunkermotren (https://www.dunkermotoren.com/), the specifications of this motor are outlined in **Table 3.1**.

Dunkermotoren STA-2508 Linear Servo Tube Specifications	
Peak Force	624 N
Peak Current	20 A
Force Constant (Sinusoidal-Comm)	44.1 N/A$_{rms}$
Pole Pitch	51.2 mm
Peak Velocity	4.7 m/s
Accuracy	+/- 12 μm

Table 3.1 Servo tube specifications

Figure 3.3 Dunkermotoren Inc. STA servo tube actuator (2022)

In this design magnets are enclosed within a circular actuator tube. The effective travel of this device can be increased or decreased as desired by lengthening the actuator tube. The core of the proposed actuator has two main components: a moving actuator rod and a fixed stator housing. The actuator rod consists of a non-magnetic stainless steel tube filled with 13 high-quality, 25mm circular neodymium NdFeB magnets. The actuator rod sits in a polymer (PTFE) bearing placed within the stator housing, which is encapsulated by a series of three windings that enable the actuator rod to be commutated. The process of commutation is an important attribute, despite adding an extra level of complexity, it aids in decoupling the relationship between the force output of the device and the velocity of the plunger. This means that for a fixed velocity, the amount of force applied to the plunger can vary independently, by increasing or decreasing the different phase currents. As illustrated in **Fig. 3.4** the process of commutation maintains an orthogonal relationship between the magnetic fields in order to maximize force output (Aerotech).
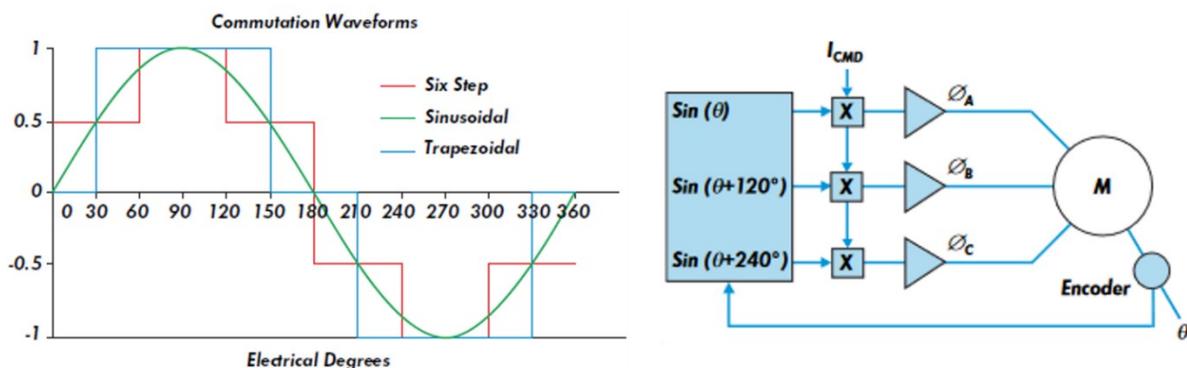
Figure 3.4 Commutation waveforms and winding electrical current (Aerotech, 2010)

The actuator chosen for this study is equipped with three hall effects sensors as well as a sinusoidal encoder. The hall effects sensors determine the relationship of the magnetic field flux of the permanent magnets within the actuator tube upon motor startup, and the sinusoidal encoder is then used to vary the phase angle as a function of actuator tube displacement, knowing the fixed pole pitch of the magnets.

3.4 Power Electronics

Commutation of the coils and precise actuator motion is accomplished via an inverter/amplifier servo drive. In this study the Parker Compax 3 was utilized due to its ability to accurately drive linear motors (Parker Hannifin Corporation). This unit converts an AC waveform into a DC square wave, **Fig. 3.5** below illustrates the basic construction of an inverter/amplifier. AC current is converted to DC using a bridge rectifier, the DC current is then fed to six internal gate bridge rectifiers (IGBT), which act as high-speed switches. The switching of the IGBTs is controlled via a micro-controller within the drive at a maximum frequency of 16 kHz, and utilizes a space vector modulation (SPVM) algorithm in order to obtain a three phase, AC waveform of desired amplitude and frequency. The micro-controller also receives a desired motion profile, and with the feedback from the sinusoidal encoder in conjunction with a PID loop will ensure the required motion ensues.
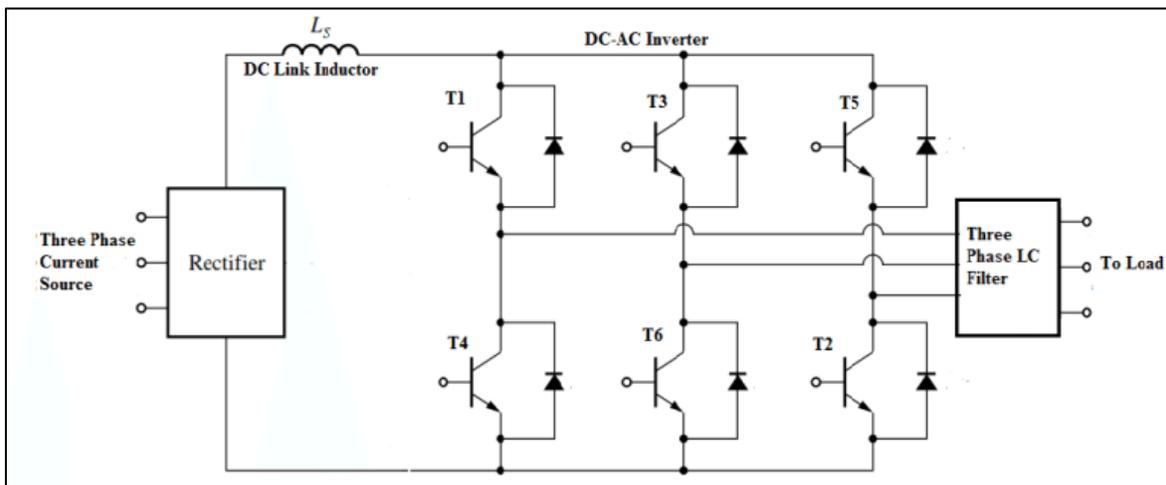
Figure 3.5 Three phase inverter circuit diagram (Parker Hannifin Corp. parkermotion.com)

Parker Compaq 3 T10 Drive	
Power Input	253 V.AC @ 60Hz/50Hz
Input Phases	3Ø
PWM Switching	16 kHz
Continuous Current Output (RMS)	15 amps
Peak Current Output (RMS)	30 amps
Commutation	Sinusoidal
Velocity Loop	125 µs
Position Loop	125 µs

Table 3.2 Servo amplifier specifications

In this study the Compax 3 will be used in position control mode, whereby a finite series of pulses are sent to the drive at a predetermined frequency. The pulse train sent to the drive must adhere to industrial standards, and therefore have a maximum amplitude of 24 volts, with a maximum frequency of 300 kHz. The drive then utilizes an internal map to correlate each rising edge of a pulse with a fixed linear distance of the actuator rod's pole pitch. The sinusoidal encoder provides real-time feedback of the actuator rod's displacement and a PID loop, illustrated in **Fig. 3.6** ensures that motor windings are energized appropriately to compensate for any following error (Parker Hannifin Corp. 2013). The exact values of the parameters used in the PID loop, depicted in **Fig. 3.6**, were established after consultation with Dunkermotoren, and optimized experimentally. This was accomplished using software provided by Parker (C3 servo Manager), whereby the system was tested under experimental load and optimized to decrease following error and whilst maintaining stability of the PID loop.
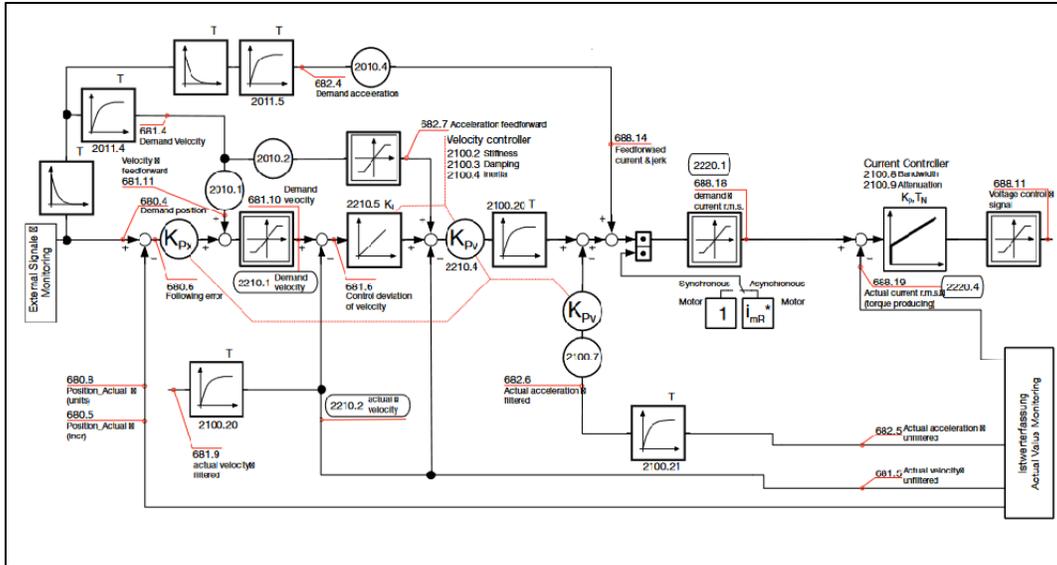
Figure 3.6 PID control loop for Compax 3 (Parker Hannifin, 2013)

PID Loop Relevant Parameters	
Pulses Per (cm)	1000
Permissible Deviation (increments)	20
Actuator Rod Weight (kg)	1.310
Stiffness Gain (%)	200
Damping Gain (%)	40
Mass Inertia Gain (%)	60
Velocity Feed Forward Gain (%)	100
Acceleration Feed Forward Gain (%)	100
Current Feed Forward Gain (%)	100
Tracking Error Filter (µs)	50

Table 3.3 Servo amplifier PID loop settings

The parameters depicted in **Table 3.3** represent the final tuning of the actuator. Tuning was performed by applying an oscillatory step response to the system at a speed of 4 m/s and a distance of 20mm, and then utilizing an oscilloscope to track the actual position, commanded position and following error versus time. The PID parameters were modified until minimal overshoot, minimal

flowing error and good vibration suppression about the target destination were achieved. **Figure 3.7** below demonstrates both the actual position and the flowing error. The time division on the horizontal axis is set to 400ms and the divisions for the error and position are 5 increments and 1000 increments respectively. As is normal with a step response input to a PID loop, a maximum deviation of 8 increments (80 µm) is observed, when the relative move is commanded the plunger deviates from its real-time target, but the error is recuperated in a timely manner. The tuning performed on the PID ensures that when the actuator is coupled to the injector head, the plunger will follow its outlined trajectory with +/- 20 increments, irrespective of the changing factors such as friction, nozzle size or fluid viscosity. This will greatly simplify modeling the output pressure of the device as the only relations ship that needs to be considered is that of the pressure increase in the injection chamber as a function of plunger displacement.
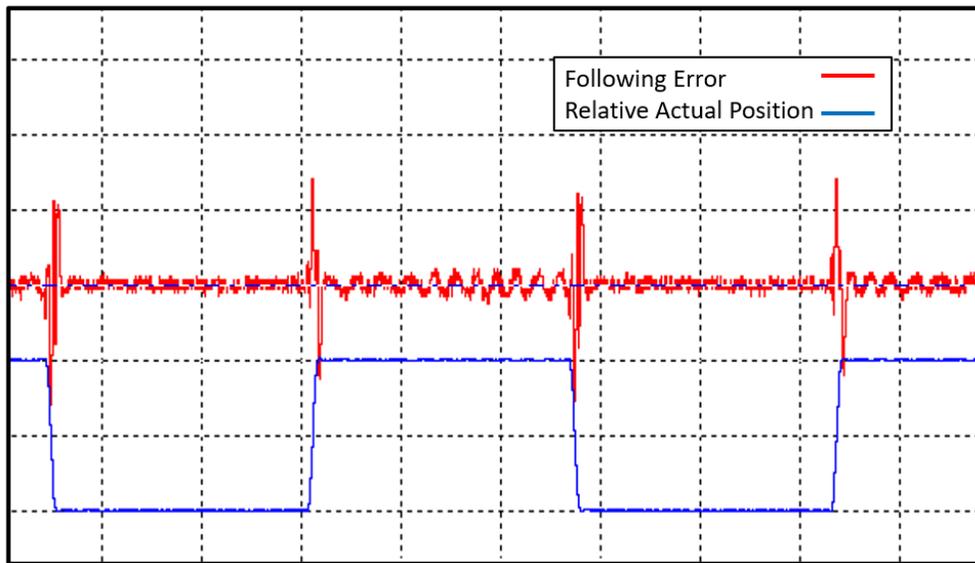
Figure 3.7 Following error as a function of displacement

3.5 Prototype Device
3.5.1. Experimental Setup

In order to produce the required liquid jets for experimental analysis an injection chamber, a small diameter plunger as well as a nozzle must be added to the actuator. The injection chamber is fitted to the servo actuator by utilizing an adapter block which mounts directly to one of the stator's end caps. This ensures concentricity between the actuator and injection chamber. Furthermore, in this manner, the device can be used for future works and different injection chamber geometries can be studied and verified for performance. The prototype consists of an injection chamber with a 6.35 mm bore that is terminated by a thread which receives a nozzle. The orifice-type nozzles manufactured by O'Keefe used in this experimental device have successfully been used in previous studies by Portaro and Ng (2015) to obtain confined jets with minimal divergence. This study will evaluate the performance of the device in shaping pressure profiles utilizing four different nozzles outlined in **Table 3.4**.

Nozzles Evaluated	
Nozzle Number	Orifice Diameter (µm)
6	150
8	200
10	250
12	300

Table 3.4 Nozzle sizes used with servo tube liquid jet injector

The injection chamber also contains one threaded port, which serves as a filler inlet, to recharge the chamber with fluid. The injection chamber also houses a plunger with an O-ring sealed tip. It is important to note that when the plunger is clear of the filling port, the size of the bore is increased to allow air to vent as the chamber is filled. The plunger is coupled to the actuator rod through a threaded coupling. The stator end cap on the opposing side of the injection chamber is capped by a block containing an OMRON D5A limit switch capable of 3 µm precision. The limit switch will enable the precise referencing of a home position, from which absolute measurements can be applied. **Figure 3.8** illustrates how these individual components are coupled together to produce the injector.

Servo Tube Injector Specifications	
Injection Chamber Diameter	6.35 mm
Injection Chamber Volume	2.5 ml
Oring-Seal	1/8x1/4x1/16 – 75 duro

Table 3.5 Servo tube liquid jet injector specifications
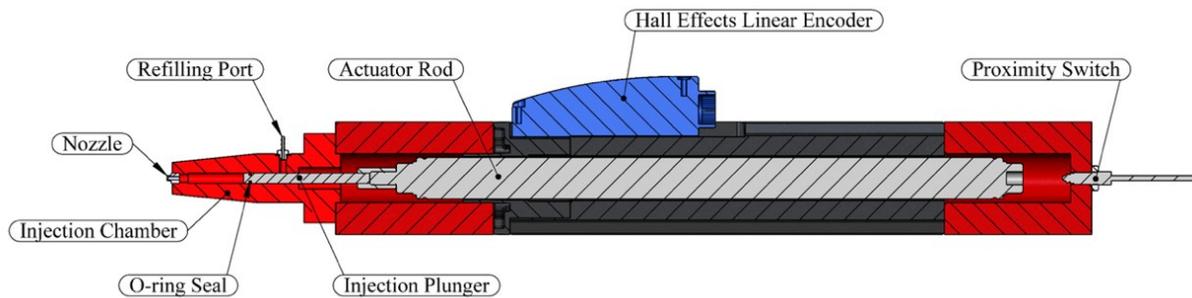
Figure 3.8 Schematic of complete servo tube driven injector

In order to accurately gather pressure traces the experimental prototype is fitted to a specially designed stand as shown in **Fig. 3.9**. This stand makes it possible to mount the injector in a vertical position and provides fine positioning of the injector height so that the standoff distance can be adjusted and accurately maintained upon subsequent runs. The stand weighs 75 kg and is constructed from a 12.7 mm thick plate, this provides the necessary stability to cope with the forces generated by the servo tube actuator.
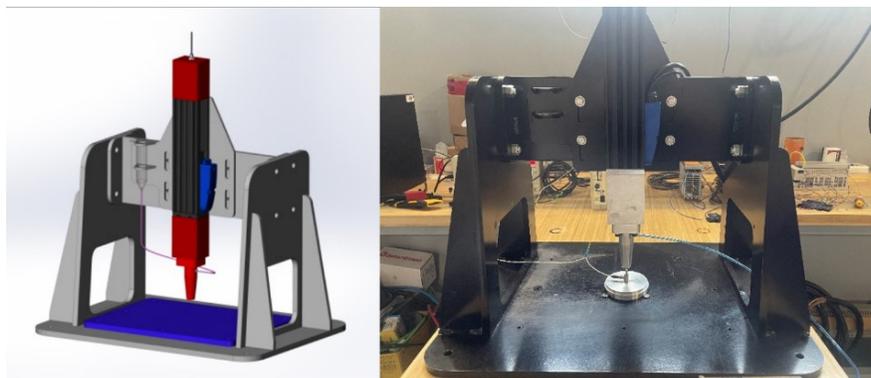
Figure 3.9 Test stand for servo driven injector

3.5.1 Actuator Motion

In order for the actuator to deliver an injection, a motion profile is required, illustrated in **Fig 3.10**. As previously mentioned, this must be produced in the form of a pulse stream. The pulse stream specifies the number of increments that the plunger will move downward as well as the velocity, this is controlled by the amount of pulses and the rising edge to rising edge frequency.
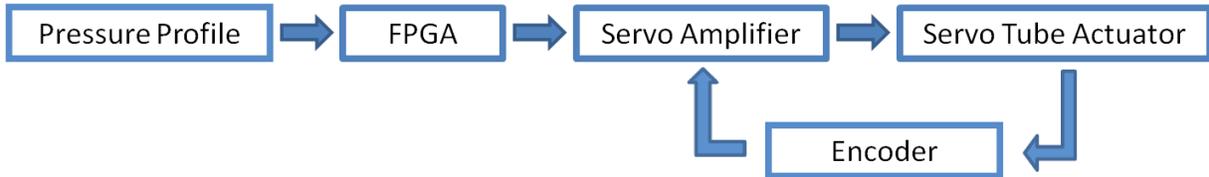
Figure 3.10 Block diagram of closed-loop servo tube injector

In this study a field programable gate array (FPGA), specifically a Xilinx ZYNQ SoC is used to construct a stream of varying frequency TTL pulses with an amplitude of 0 to 5 V. This device contains thousands of logic gates as well as many RAM blocks that can be configured using hardware descriptive language (HDL) in order to create complex digital circuits. In the case of this experiment an NC oscillator is developed, which outputs pulses based on a velocity lookup table, the system runs on a 100 MHz clock, which allows pulsing frequencies of up to 50 MHz to be generated. The FPGA is mounted on a development board provided by AVNET, which makes it possible to program the FPGA chip and gain access to all inputs and outputs via breakout connectors. The TTL (0-5V) pulse stream must then be converted using a high-speed optocoupler, into a 24 V pulse stream, a Weidmuller Optocoupler providing a push-pull output, and capable of 600 kHz switching frequencies is used for this task. **Figure 3.11** shows the setup outputting a pulse-stream of 35 kHz correlating to (0.35 m/s) produced at 24 V, with the addition of a 1 k ohm pull-up resistor between the 24 V and the digital pulse input of the servo amplifier.
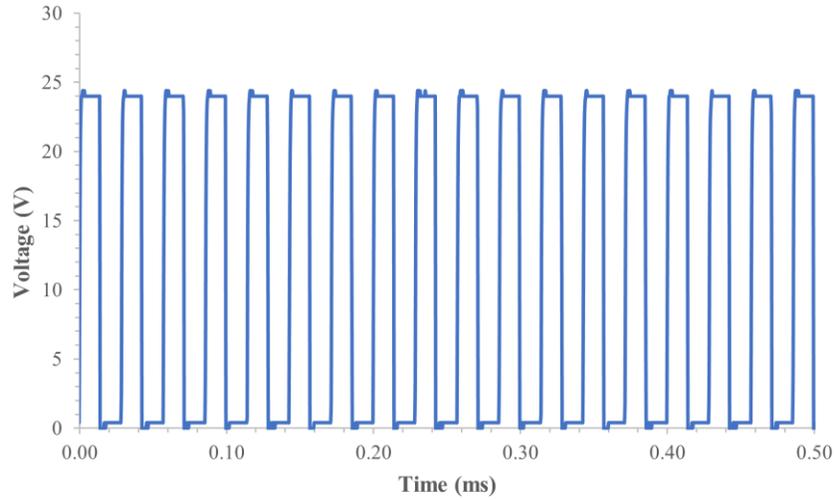
Figure 3.11 Sample pulse train from FPGA to input of servo amplifier

The pulse stream does not exhibit an acceleration or deceleration, as the servo amplifier has a built-in function which automatically counts the number of increments and input frequency and then applies a trapezoidal trajectory planning, whereby the increments/s^2 (accel/decel) and increments/s^3 (jerk) can be defined by the user.

3.5.2 Jet Production

As previously illustrated the jet stagnation pressure emanating from a jet injector depends on a force balance between the driving force imparted on the plunger by the power source and the resistive force of pressure buildup in the chamber due to the bulk modulus of the working fluid as well as any friction the device exhibits. This has been well modeled by Baker and Sanders (1999). The equations are:

$$\frac{dp}{dt} = \frac{(B+p)\dfrac{dx}{dt} - \dfrac{BA_o}{A_p}\sqrt{\dfrac{2p}{\rho_o}}}{L - x_p}$$

Eq. (3.1)

$$\frac{d^2x}{dt^2} = -\frac{F_P}{m_p} - \frac{A_p}{m_p}\frac{dx}{dt}\frac{F_f}{m_p\left|\dfrac{dx}{dt}\right|}$$

Eq. (3.2)

where B is the bulk modulus of the fluid, ρ_o is the initial density, p is the pressure and A_p and A_o are the piston and orifice area determined from the diameters of the piston and nozzle orifices, respectively. For water, $B = 2.18$ GPa and $\rho_o = 1,000$ kg/m^3) are used. x_p and dx/dt are the position and velocity of the piston, respectively, and $L = 80$ mm is the length of the liquid column inside the injector. m_p is the mass of the piston. F_p and F_f are the driving force and frictional force, respectively (Portaro and Ng, 2015).

Utilizing a servo-controlled actuator makes it possible to decouple this set of ordinary differential equations, and therefore it is no longer necessary to consider Eq. 3.2 as the PID loop for position and velocity within the amplifier will ensure that it is possible to attribute any desired plunger velocity (dx/dt) to shape the pressure output of the device according to Eq. 3.1. For a given velocity profile the corresponding pressure and pressure changes can be easily obtained. The effects of changing friction due to O-ring seal wearing or increased power demands for more viscous fluids no longer need to be considered. The errors caused by outside factors will be compensated at 8 kHz. If the speed of sound in water is considered along with the chamber length then changes to the plunger velocity under 2 kHz, can be traced at the output of the nozzle. **Figure 3.12** illustrates the stagnation pressure behavior of the injector under a given velocity mapping with time.
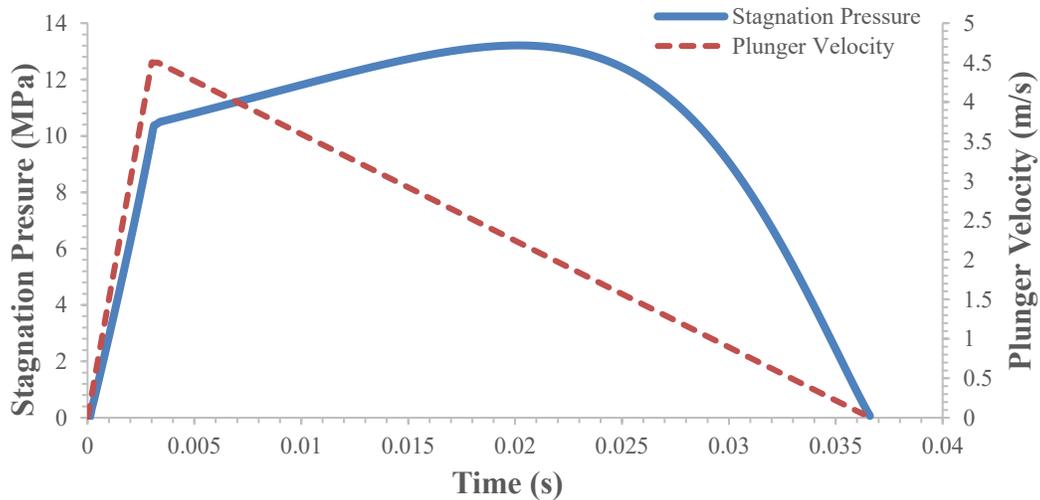
Figure 3.12 Pressure output as a function of theoretical plunger velocity

The velocity map depicted in **Fig. 3.12** was tailored to yield a pressure pulse with a peak of 13 MPa and have constant pressure output rather than a noticeable peak in order to show the controllability of the device and its ability to overcome the back driving forces present within the injection chamber. The 13 MPa peak will illustrate the ability of the device to puncture human tissue as it is the upper limit of what is prescribed by Shergold *et al.* (2006).

3.5.3 Capturing Pressure Traces

The pressure traces in this study are captured through the use of a force transducer. As previously mentioned, the force measurements are then converted to pressures by utilizing the nozzle orifice area, given that there is negligible divergence at the standoff distances used to gather the data. Furthermore, the time frame of the phenomenon is such that the high response rate of piezoelectric sensors is required to properly map the pressure output. In this experiment the 209C11 force transducer from PCB Piezotronics is used.

PCB 209C11 Force Transducer	
Measurement Range	.00979 kN
Sensitivity	494.60 mv/kN
Lower Frequency Response	.5 Hz
Upper Frequency Response	30 kHz
Temp Range	-54 to 121 °C

Table 3.6 Specifications of force transducer used to capture pressure traces

The force transducer is linked to a PCB Piezotronics ICP 482A22 signal conditioner, which is monitored by a Rigol DS1102E digital oscilloscope with 1G Sa/s. The scope is triggered from the pulse stream sent by the FPGA to the servo amplifier, this aids in avoiding false triggers due to the noise generated by the power electronics of the servo amplifier. Furthermore, the force transducer is mounted on an aluminum back plate as is illustrated in **Fig. 3.13** which is secured to the testing apparatus via 3 magnets, this facilitates removal and ensures proper positioning of the sensor. The standoff distance used in the experiments corresponds to .8 mm as it resulted in waveforms that were not greatly affected by the overspray of the impinging jet.
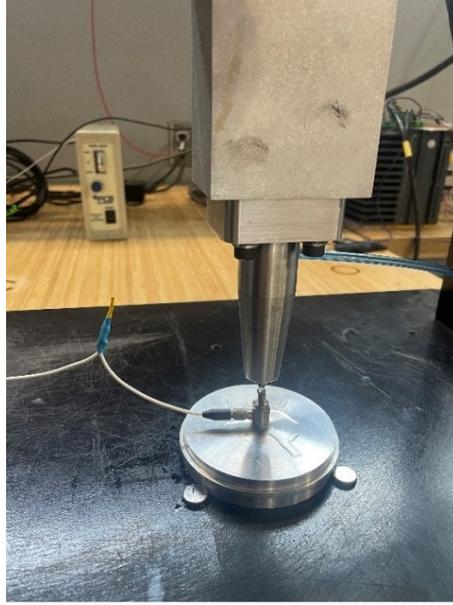
Figure 3.13 Close-up of force transducer and jet injector nozzle

3.6 Results and Discussion

In order to accurately demonstrate the feasibility of using permanent magnet synchronous linear motors as a power source for liquid jet injection, the ability to provide enough stagnation pressure and penetrate human tissue will first be examined. This must be accomplished without reaching the stalling current of the motor, or deviating excessively in position tracking error, such that the servo loop can no longer recover. Although the power of a liquid jet can be modeled by Eq. 3.3, and yields a jet with a force of approximately 188 W, under the largest nozzle size (300 µm) and greatest density (1230 kg/m³), far greater power is required to provide the impulse force necessary to pressurize the chamber for proper liquid jet formation. According to the plunger velocity map depicted in **Fig. 3.12**, a theoretical power of 9.1 kW is required. This lies below the 13kW the Compax 3 can provide, and will be the threshold for the peak injection pressures.

$$Power = \frac{1}{8}\pi\rho D^2 U^3 \qquad \text{Eq. (3.3)}$$

3.6.1 Penetrating Power

The first set of data illustrates the ability of the servo-driven injector to produce a pressure output great enough to puncture tissue. For this experiment a pressure curve with an average stagnation

57

pressure of 13 MPa was desired, and the corresponding velocity profile illustrated in **Fig. 3.12** mentioned above was programmed into the FPGA.
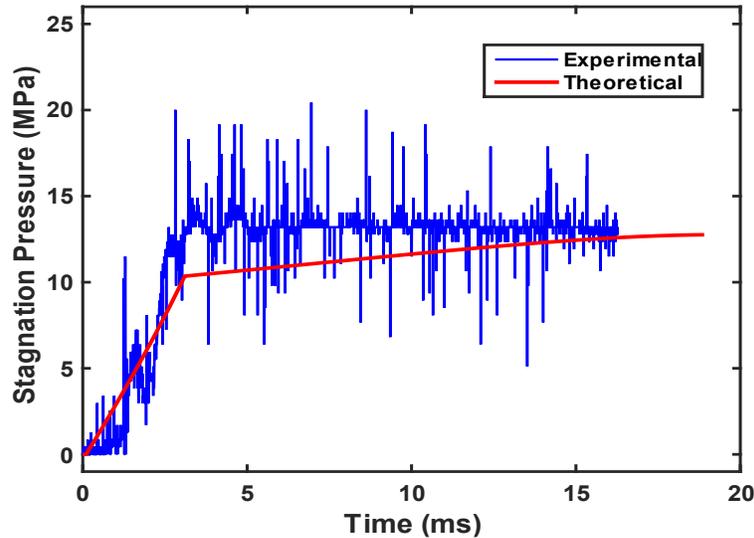
Figure 3.14 Experimental and theoretical overlay of stagnation pressure for initial velocity profile

Figure 3.14 depicts an overlay of the experimental trace to the desired pressure output of the device, the initial pressure spike oscillates about the desired values as the desired output climbs to 10 MPa, and then the experimental trace overshoots by approximately 3 MPa, at which point the velocity of the plunger begins to decrease and the PID can begin to diminish the error. The overshoot in this situation represents 30% of the target value, improving the error can be done by increasing the response time of the servo loop, however, there are a few factors that limit what can be achieved with this amplifier. The first is the control frequency of the PID loop which is set to 8 kHz, ideally this should be on the order of 30 kHz, to respond faster than the transmission of the pressure wave in the injection chamber. In the current experimental setup, the switching frequency is also limited by the maximum switching frequency of the IGBTs and their ability to energize the motor windings with the appropriate amplitude and frequency of AC current.
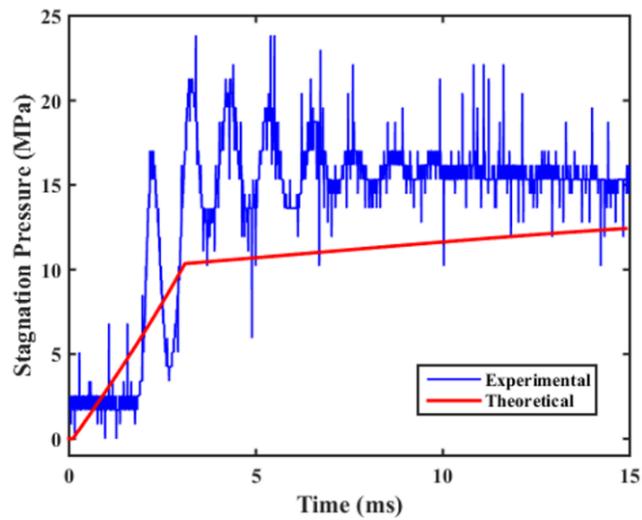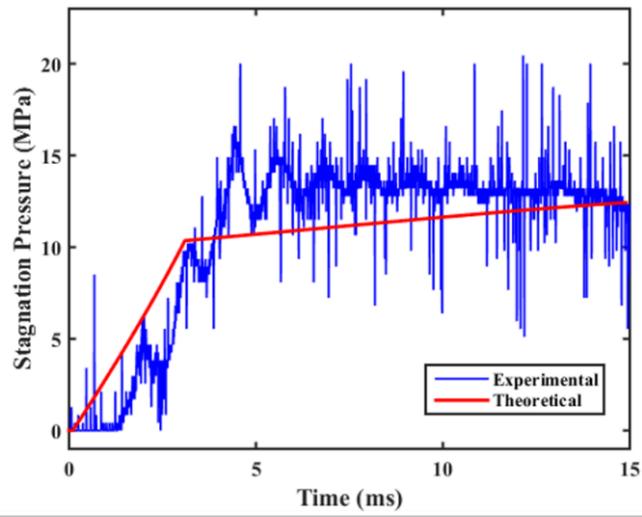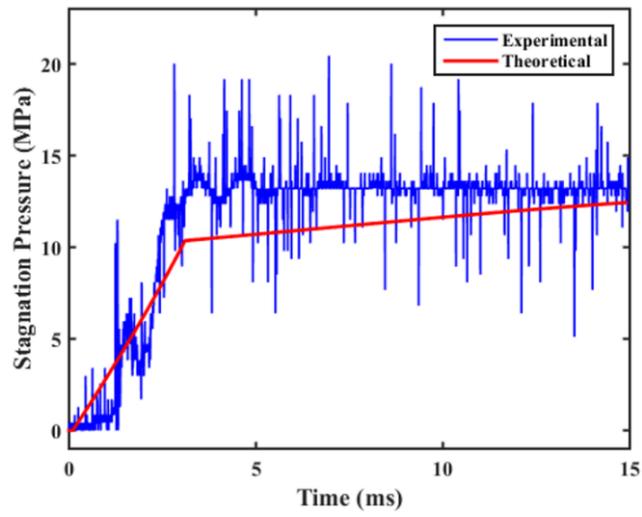
Figure 3.15 Test trials illustrating repeatability of servo tube injector in shaping pressure pulse

Nevertheless, it was observed from **Fig. 3.15** that the traces remained relatively consistent over repeated trials, thus concluding that the device seems to display an acceptable level of repeatability. Moreover, a high-speed photo sequence of the jet, taken penetrating 10% ballistic gel, with the use of a PCO high-speed camera, illustrates that the injector can penetrate human tissue and overcome the initial forces required to produce a high-speed pressure pulse, see **Fig. 3.16**.
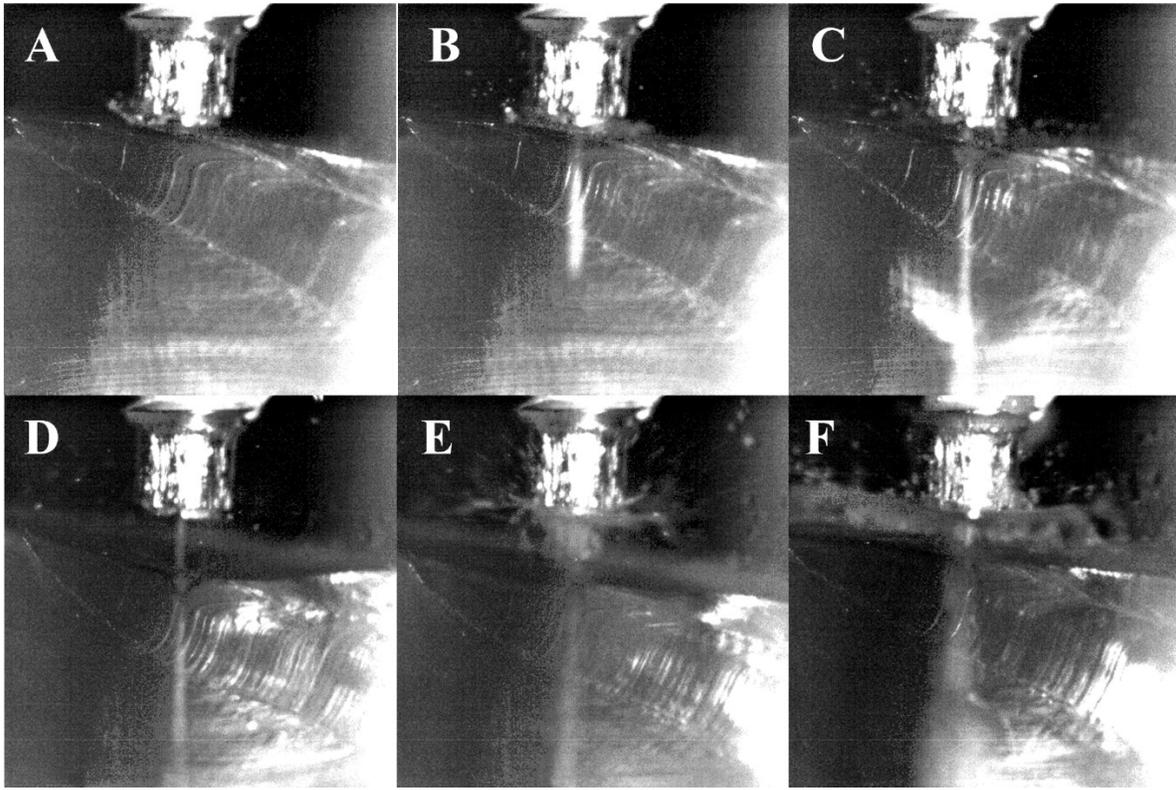
Figure 3.16 High-speed sequence of servo tube injector penetrating 10% ballistic gel

Although the pressure waveform that was programmed into the device did not display a typical peak followed by an average stagnation pressure, it penetrated the ballistic gel cleanly upon initial contact. It is possible to observe the typical traits of the high-speed liquid jet injection, as the jet penetrates the gel. The liquid jet reaches a target depth and then begins to deposit more fluid at this depth, whereby a bulbus is seen forming. It should also be noted that the backsplash observed in **Fig. 3.16f** is due to the fact that ballistic gel does not absorb liquid as tissue, as described by Shergold *et al.* (2006), hole formation is due to a crack propagation through the gel, and as the injection makes its way to the end the crack closes forcing the liquid to the surface.

3.6.2 Device Accuracy

One of the key elements in illustrating the prototype's feasibility, is the ability to shape a pressure output and consistently maintain that result with respect to changing nozzle size and fluid viscosity. Therefore, it was decided to reproduce a similar pressure output that is in line with commercially available units. **Figure 3.17** depicts a stagnation pressure wave, with a peak of 15 MPa occurring at 5ms and an average delivery pressure of 6 MPa reached at approximately 7.5 ms and utilizing the servo amplifier's maximum rates of accel/decel.
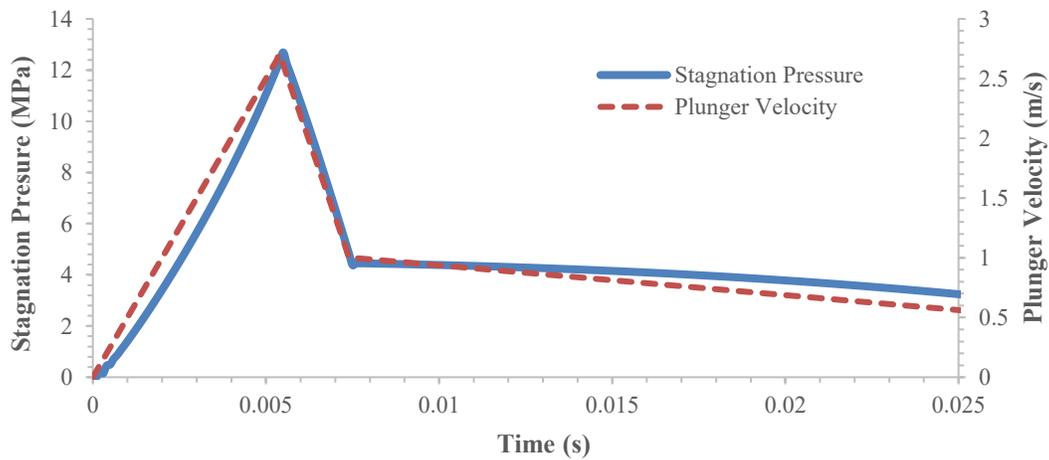
Figure 3.17 Pressure profile representing typical behavior of commercially available injectors

This velocity profile is tested under seven different viscosities and four different nozzle sizes. The fluid viscosity is varied by utilizing glycerol and making aqueous solutions of different weight percentages. **Figure 3.18** shows the variation of both density and viscosity as a function of weight%, the seven different test conditions correspond to 0, 20, 30, 40, 60, 70, 80 wt% glycerol respectively. Each nozzle size and viscosity combination is run with a minimum of 12 repetitions to ensure meaningful conclusions can be drawn from the data sets. It should also be noted that 90 and 100 wt% were also considered, the test device could create a liquid jet without attaining the stalling current of the linear motor, however, after approximately 3 injections, the nozzles would show signs of blockage. It was impossible to dislodge the blockage without heating the tip of the nozzle with a propane torch which would cause deformation of the orifice. Consequently, it was decided to test only up to 80 wt%, to extend the longevity of the nozzles.
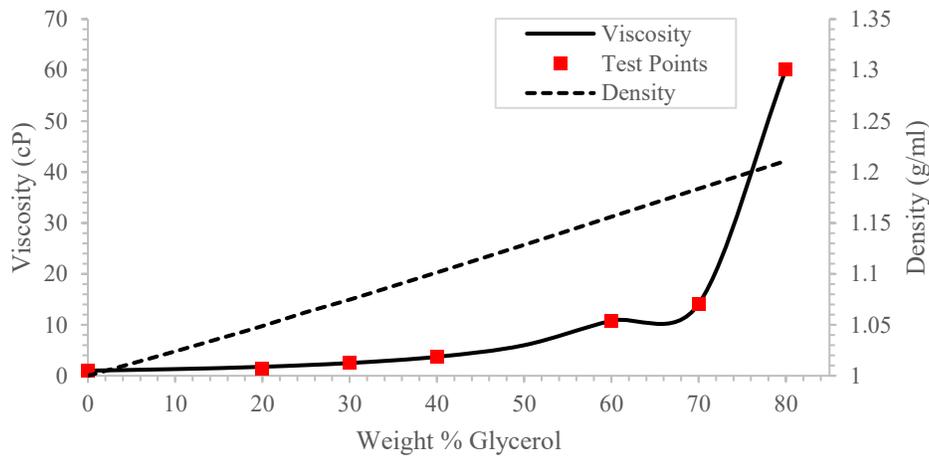
Figure 3.18 Density and viscosity as a function of weight% glycerol

Figure 3.19 depicts an initial pressure trace, which illustrates the system's ability to dynamically shape a pressure profile. One of the positive aspects of the gathered results, shows that the system can accurately reach the desired peak and mean injection pressures. Discrepancies can be found in the time required to reach the peak, which was targeted at 5 ms, but occurred at approximately 2.5 ms, a trend that seems to be consistent with all the profiles that were tested, further investigation into this phenomenon needs to be conducted. As previously mentioned, the response time of the fluid at 20 kHz seems to outpace the servo loop. Oscillations about the mean injection pressure were also observed, this is in line with pressure plots from other needle-free devices. Although the oscillations are present, they settle toward the tail end of the injection. The oscillation can partly be attributed to the rapid loading and unloading of the piezoelectric force sensor.
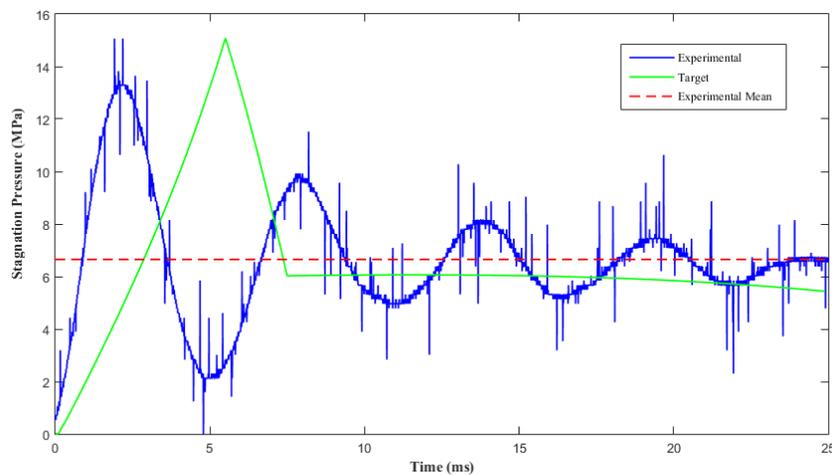
Figure 3.19 Experimental and targeted pressure profile tested under various viscosities and nozzle sizes

Comparisons between the experimental values displayed in **Fig. 3.20** through **Fig. 3.23**, and the theoretical values, corrected for change in density of the fluid and nozzle size, yields a maximum deviation of approximately 5.5 MPa when comparing pressure peaks and 1.37 MPa when comparing mean stagnation pressures. It should be noted that the theoretical differences for peak and mean pressures as a result of differing densities correspond to .5%, from 1000 kg/m^3 to 1210 kg/m^3.
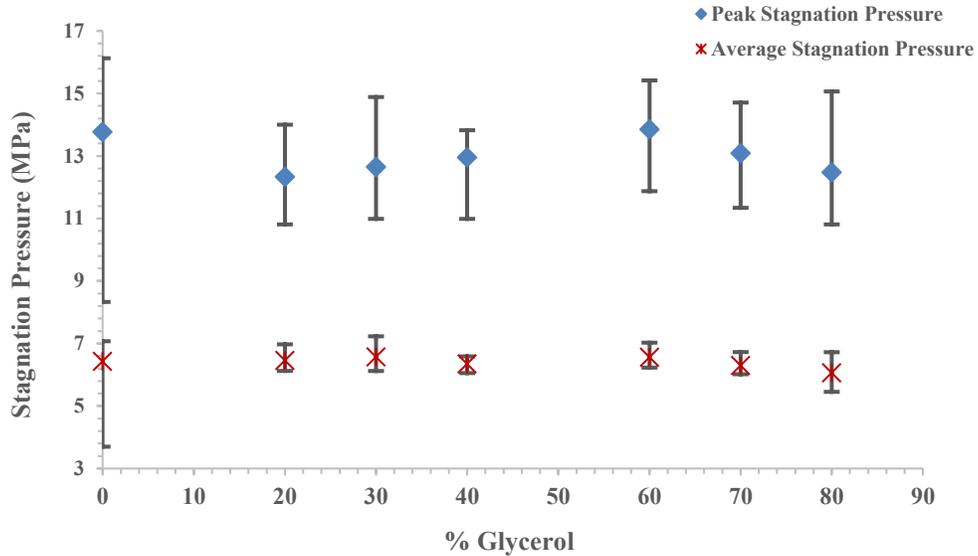
Figure 3.20 Peak and average stagnation pressure as a function of %glycerol for size 6 nozzle
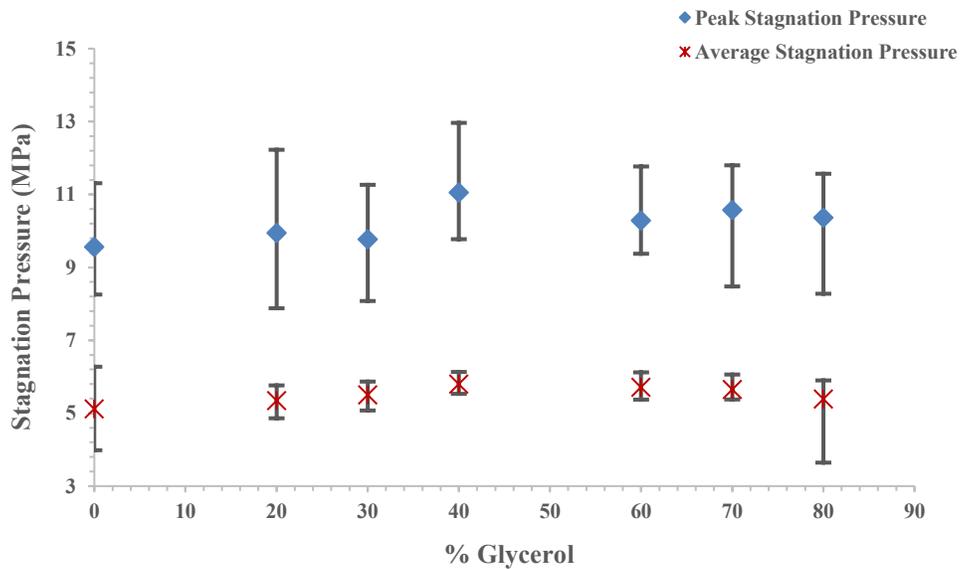
Figure 3.21Peak and average stagnation pressure as a function of %glycerol for size 8 nozzle
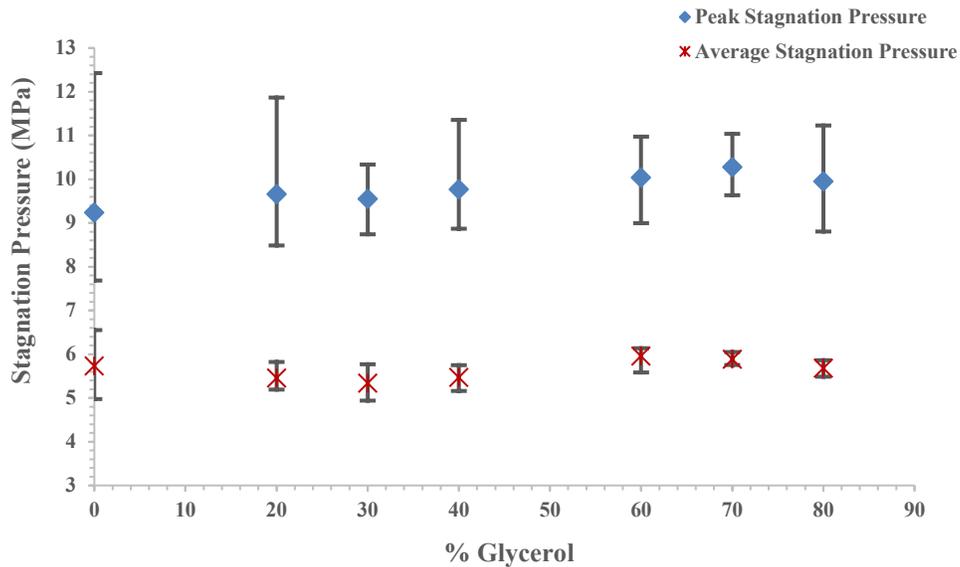
Figure 3.22 Peak and average stagnation pressure as a function of %glycerol for size 10 nozzle
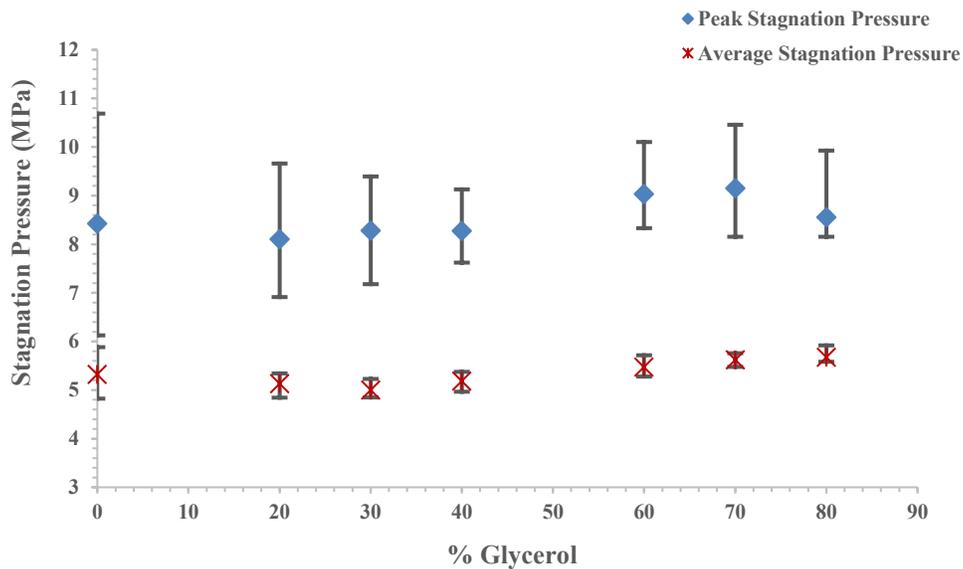
Figure 3.23 Peak and average stagnation pressure as a function of %glycerol for size 12 nozzle

3.6.3 Pulsating Injection Delivery

The device was also verified for its ability to produce large volume, pulsed injections. It is hypothesized that this technique can offer additional benefits as it will not overload the tissue with one large does but rather deliver it in a gradual manner. This aids in increasing injection

completeness as well as the accuracy of targeted tissue depth. **Figure 3.24** illustrates the injector delivering a two-pulse injection with the first phase at 15 MPa and the second phase at 7.5 MPa, corresponding to half the pulse frequency of the first, but on the same interval duration.
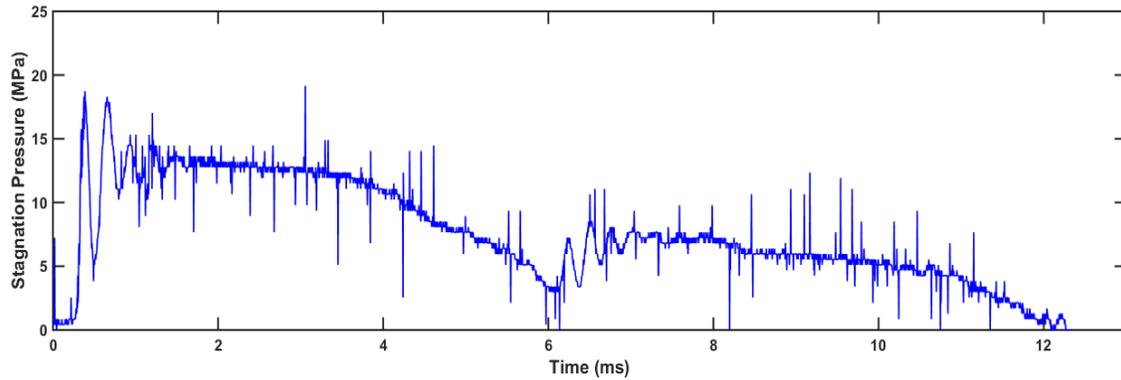
Figure 3.24 Twin pulse injection delivery

Figures 3.25 through **3.27** illustrate the system's ability to deliver an injection corresponding to an injection volume of approximately 0.2 ml per pulse. In order to obtain the pulsing action, a delay of 50 ms was added in between each pulse, and the pulse magnitude as well as the duration remained consistent throughout the multiple profiles. Hence, the pulsed injections were delivered at a frequency of approximately 10 Hz. The chamber was filled once to its complete volume at the beginning of the pulse sequence and therefore, the subsequent pulsed jets constituted a fraction of the total chamber volume, and consequently, the jet behavior was shown the same for each pulse.
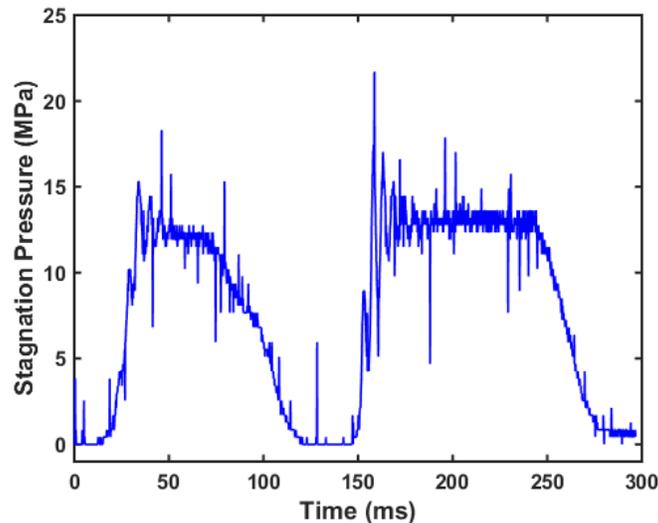
Figure 3.25 Twin pulse injection
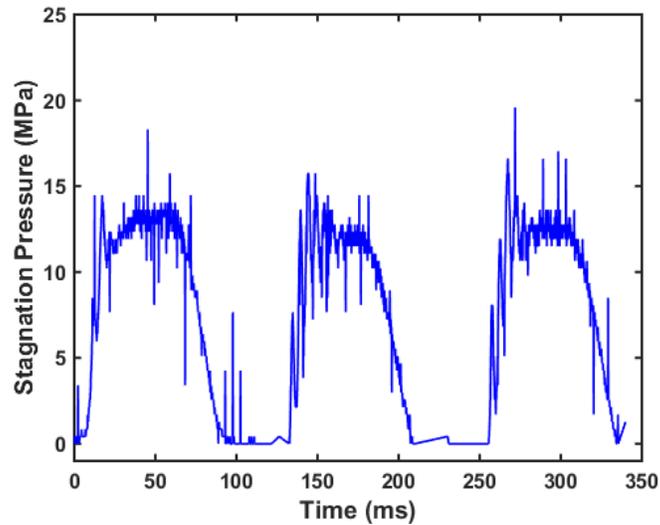
Figure 3.26 Triple pulse injection
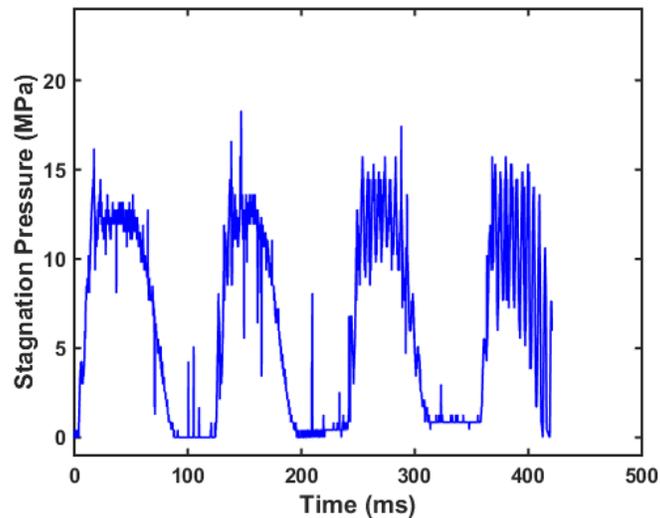
Figure 3.27 Quad pulse injection

The device exhibited a good level of repeatability, attaining a mean pressure of 13 MPa per pulse. Further investigation is necessary to determine the maximum frequency at which the pulses can be delivered without blending, in the current study a gap of 30 ms was the minimum that could be used to exhibit distinct peaks. Moreover, the accuracy of the pulse length will also depend on the precision and speed displayed by the control loop and linear motor combination.

Overall, the device appears to perform well in shaping a pressure profile, with very repeatable average stagnation pressures. The peak pressures display greater variation, and future studies should focus on quantifying the effect of servo response time vs fluid response. This can be

achieved by building a custom amplifier that not only makes use of high-power-high frequency IGBTs, and control hardware capable of working on the order of MHz, but also considers the real-time pressure output, to build a feed-forward model for the device so that it can be used more accurately.

3.6.4 Completeness of Injection and Real Tissue Trials

It was also possible to examine the device's ability to penetrate and deposit medication in real tissue. This short series of tests made it possible to verify if different targets could be attained by utilizing two different pressure curves, pure water as a test fluid, and a 150 μm nozzle. The volume chosen for the initial penetration study was .4 ml, which corresponds to 10 mm of downward travel. In order to ensure the proper volume of fluid was delivered for each sample, the chamber was filled and then primed once, at that point the sample was placed underneath and the injection was performed. Test samples of 40 mm to 45 mm thick pig thigh, obtained from the consumer market, weighing from 26 gram to 35 grams were created and brought to room temperature, the samples were then placed as illustrated in **Fig. 3.28**, under the injector utilizing a spacer to compress the samples up against the orifice so there would be no standoff distance. The first set of tests looked at the injector's ability to achieve different depths with the out skin removed, as the tensile strength of pork skin increases substantially as the tissue dries.
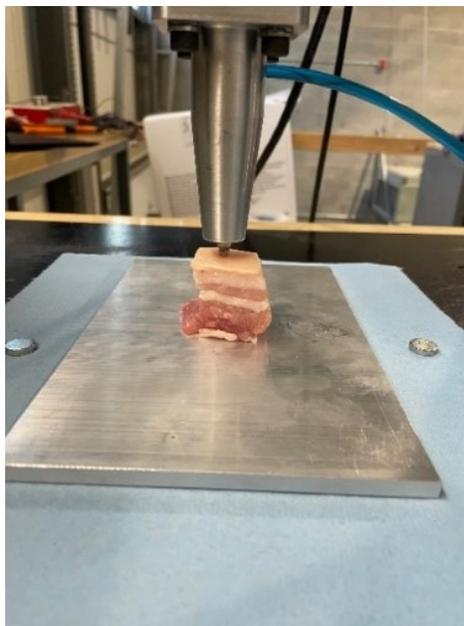
Figure 3.28 Porcine test specimen placement

The penetration of the pork tissue delivered promising results; the two different profiles were able to deposit at different depths. Furthermore, the samples were weighed pre and post-injection in order to determine the level of completeness. For figures in **Table 3.7** the pre-injection weight for the first profile corresponds to 31.7g and post injection at 32.1g, this yields a delivery efficiency of 100%, however it should be noted that the weight of the sample could only be obtained within .1g, thus a more accurate weight in should reveal a delivery efficiency of less than 100%, this is expected as there was backsplash, although minimal.

Penetration Test (Porcine Tissue)		
Profile	Test 1	Test 2
1		
2		

Table 3.7 Porcine penetration test

Figures in **Table 3.8** illustrates the injector's ability to deliver an injection into the epidermis of pork shoulder. The thickness of the epidermis varied from approximately .7 mm to 1 mm. The first profile was able to puncture the skin whilst the second profile was not included as it was not able to create a puncture point. The 15 MPa injection, deposited some liquid as is observed in the figures

below, however most of the injection volume remained on the surface of the skin. It is important to note that the porcine skin thickness is substantially thicker than human skin, and due to the age of the sample, the outer layers tend to lose moisture thus increasing the amount of force necessary to penetrate.

Porcine Skin Injection Tests	
Cross-Section	Puncture Point
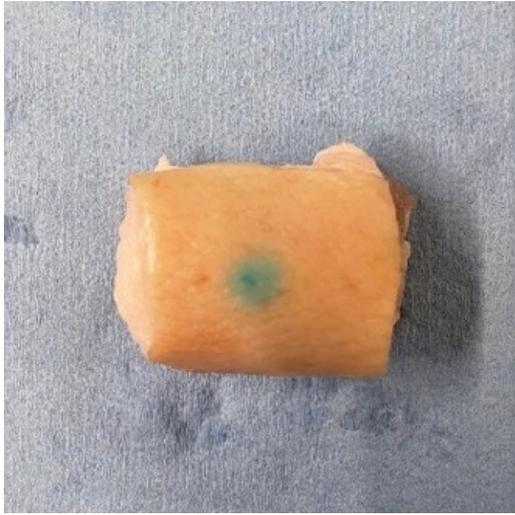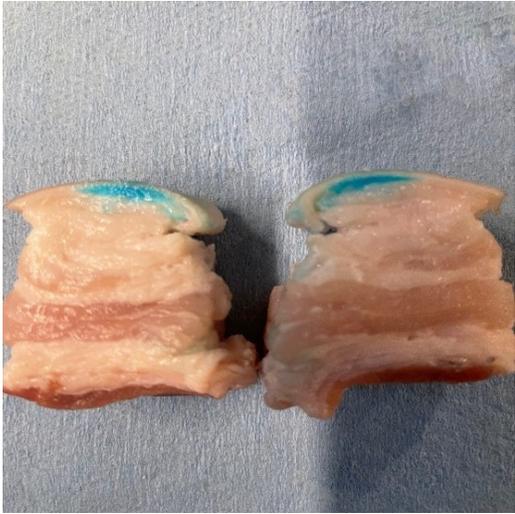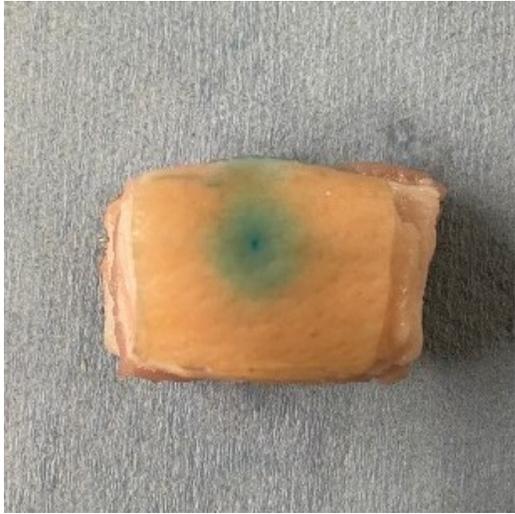
Table 3.8 Penetration of porcine samples with skin

It is worth noting that due to the current experimental limitation and facility constraints, the results in the porcine model are provided mainly for illustration purposes to demonstrate the injection capability of the present prototype. A more systematic investigation of the present needle-free jet injector prototype in a well-controlled porcine tissue model, similar to the study by Ruddy *et al*., (2019), is required in future work.

3.7 Sources of Error

Although the prototype created in this study exhibited the ability to accurately shape pressure profiles of high-speed liquid jets, there also exist some sources of error which can be addressed to further improve the quality of experimental results. One of the contributing factors, is the tracking error produced by the PID loop and displayed in **Fig. 3.7** which can deviate up to 80 μm, this error can yield different peak stagnation pressures due to the rapid rise time in pressures and the large majority of the error occurring at the onset of the injection process. This is clearly illustrated in **Figs. 3.20** to **3.23**, where the error bars correspond to both the maximum and minimum pressure values obtained for each test condition. In order to address this issue and produce a device with better accuracy, custom power electronics can be constructed which will suit the characteristics of the servo-tube used to drive the injector rather than using a generic commercially available unit.

It should also be noted that the pressure measurements obtained from the PCB force transducer contained some noise. This was a result of harmonics generated by the high-speed switching of IGBTs, which made its way back to the oscilloscope as both the power supply for the oscilloscope and that of the servo amplifier share a common phase. Although minimal, future work should consider the addition of an appropriately sized line reactor to attenuate this noise. Furthermore, the pressure measurements were obtained with a standoff distance from the force transducer, evidently there exist some divergence of the jet in this air gap. Although the high-speed photography suggests that this is not substantial within the test regions, future studies should be conducted to characterize the variation of jet size, for the different test nozzles, and required standoff distances for more accurate stagnation pressure conversion.

3.8 Summary

The prototype injector created in this study shows promising potential, it can shape a pressure profile in real-time, deliver large volume injections in single or pulsating modes and create the necessary force required for needle-free drug delivery. Future studies can now focus on developing

power electronics that can operate at faster speeds, to help improve the accuracy of the device, as well as scaling down the size of the actuator, reducing its inertia and further improving response times and usability. This prototype can also be used to provide researchers with a platform on which to study the effects of different pressure profiles on injection depth and completeness. Nevertheless, it should be noted that there are limitations to the maximum peak pressures that can practically be achieved utilizing linear actuators. The pressure profiles provided in this study were generated utilizing the maximum current capacity of the servo amplifier, and although the actuators themselves can hand a very large amount of inrush current, even as they are scaled down in size, the amplifier drives will require larger power electronics, which might not be ideal for a clinical setting. Consequently, research should not only be limited to electronically controlled injectors, but also focus on developing and characterizing power sources that can deliver high power output with less complexity, such as is the case in the next chapter which deals with combustion-driven, needle-free injectors.

Chapter 4 : Combustion Driven Liquid Jet Injection

4.1 Relevance of Combustion Driven Injectors

New emerging trends in needle-free technology are creating a need for delivering greater volumes as well as highly viscous injections (Mitragotri *et al.,* 2006; Rohilla *et al.,* 2019). The needle-free injector's precision as well as its ability to target deep areas of tissue such as muscle, provide good building blocks for use with new drug therapies (DNA Therapy). Moreover, as explored in the previous section, the controllable electronic actuators that can provide enough initial energy release to produce the necessary pressure rises required by viscous liquid jet injection, make it difficult to practically scale these devices for clinical use. Consequently, there is a need for power sources that are sufficiently strong, easily scaled and which can be accurately controlled in order to provide a liquid jet with velocities on the order of 100–200 m/s, predictable penetration depth, large-volume delivery efficiency, as well as cope with an increase in drug viscosities observed with new drug formulations used for emerging medical treatments McKeage *et al.* (2018), Williams *et al.* (2016).

Apart from drug delivery in humans, needle-free liquid jet injection technology also attracts significant interest in animal vaccination Rao *et al.* (2006), Chase *et al.* (2008), Mousel *et al.* (2008), Chen *et al.* (2017). It provides an efficient means to achieve repetitive injection for mass vaccination of farmed livestock. It is worth noting that different livestock such as cattle or swine have rather different skin properties and often require different vaccine doses, therefore, flexible power output must be provided to the needle-free injection system.

This study explores the use of combustion to generate the required power in order to drive the needle-free injector. The detonative combustion mode is specifically considered in this work. It makes use of the pressure increase across a detonation wave in order to drive the injection and pressurize the medication. The present study serves to highlight the feasibility of using gaseous detonation-driven power sources as a convenient and efficient means of powering liquid jet injections.

4.2 Fundamentals and Methods

A detonation is a supersonic, combustion-driven compression wave across which there is a significant pressure increase (Lee, 2008). It has been suggested that by properly harnessing the potential of the detonative combustion, the energy release from such a process can be used for power generation and propulsion applications Wolanski (2013), Vasil'ev (2013). The previous work by Golub *et al*. (2013) and Krivokoritov *et al.* (2012) have demonstrated the potential of using detonation waves in stoichiometric hydrogen-air mixtures at atmospheric conditions for needle-free injections and delivering 0.2 ml of liquid water at a drop speed on the order of 70 m/s by means of a deformable diaphragm. In this study, a conventional piston-driven jet generation mechanism is employed. The reason is two-fold: to design a device capable of large volume drug delivery and to compare other types of injector systems (e.g., gas-powered, Lorentz-force, servo-tube actuated) which use the same impact mechanism. A more sensitive combustible mixture, namely, pre-mixed stoichiometric acetylene-oxygen mixture at sub-atmospheric initial pressure in the range of 25 to 60 kPa is used to provide safe operating conditions. The combustible is prepared using the method of partial pressures in a separate mixing tank.

A schematic of the experimental detonation-driven liquid jet injection prototype is shown in **Figs. 4.1** and **4.2**. The setup combines a detonation tube made of a 590-mm long, circular, steel tube with an inner diameter $D = 26.4$ mm with a custom-made needle-free liquid jet injector module. The injector module is made of a moving plunger and a metering screw used to adjust the drug delivery volume. An orifice micronozzle (O'Keefe Controls Co.) is threaded at the end of the injector for the jet generation. **Table 4.1** illustrates the important physical characteristics of the injector module.

Injector Parameters	
Orifice nozzle diameter, D_o	200 μm
Driver diameter, D_d	44.4 mm
Piston diameter, D_p	6.35 mm
Mass of the piston, M_p	150 g
Liquid column, L	20 mm

Table 4.1 Injector module parameters.

The injector is filled with water as its working fluid, density ρ_o = 1,000 kg/m³ and fluid bulk modulus B = 2.18 x 10⁹ N/m². In this investigation, the delivery volume is set at 0.6 ml. A Chapman–Jouguet (CJ) detonation is initiated at the closed end of the tube via a high-voltage capacitor spark discharge and propagates along the tube until it impacts the injector's piston, which in turn generates the high-speed liquid jet through the orifice nozzle. A PCB Model 209C11 miniature force sensor is used for the jet pressure measurement. This is accomplished using the orifice nozzle diameter, i.e., by dividing the force sensor reading of the jet impact stagnation surface by the exit orifice area. The force sensor is clamped perpendicular to the injector's nozzle exit. The output of the transducer is amplified and gathered using a RIGOL DS1102E oscilloscope with 1G sample/second.

PCB 209C11 Force Transducer	
Measurement Range	.00979 kN
Sensitivity	494.60 mv/kN
Lower Frequency Response	.5 Hz
Upper Frequency Response	30 kHz
Temp Range	-54 to 121 °C

Table 4.2 Force transducer specifications

A sketch of the detonation reflection gas dynamic process is shown in **Fig. 4.3**. Properties across a detonation wave can be computed thermodynamically using an equilibrium control volume analysis. By solving the one-dimensional conservation equations together with the tangency requirement between the Rayleigh line and the equilibrium Hugoniot curve, (i.e., Chapman–Jouguet criterion), the detonation velocity D_{CJ} and its thermodynamic equilibrium states can be computed. Chemical equilibrium software such as the NASA Computer program, Chemical Equilibrium with Applications (CEA) Gordon *et al.* (1994), provide such calculations. For the stoichiometric acetylene-oxygen mixture at different initial pressures, the CJ detonation pressure is plotted in **Fig. 4.4** (dotted line).
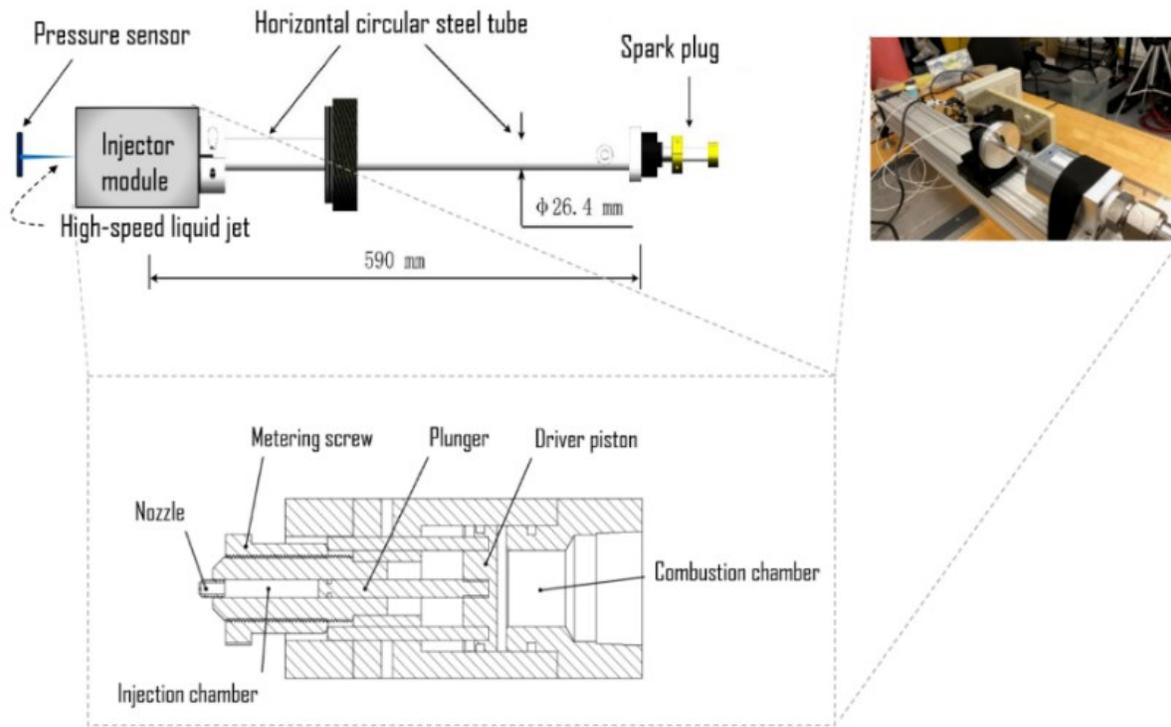
Figure 4.1 Schematic of the experimental setup consisted of the detonation tube and the needle-free liquid jet injector module
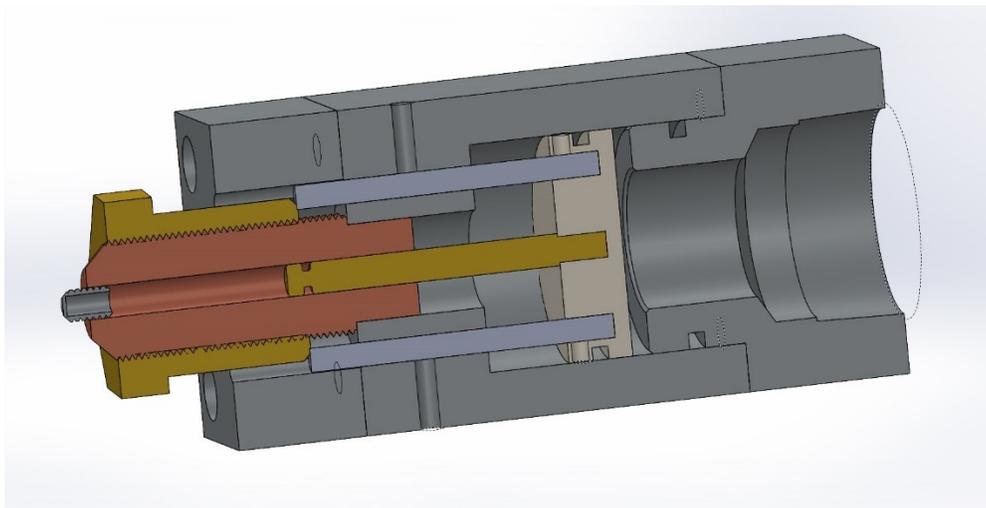
Figure 4.2 Three-dimensional cross-section of injector module
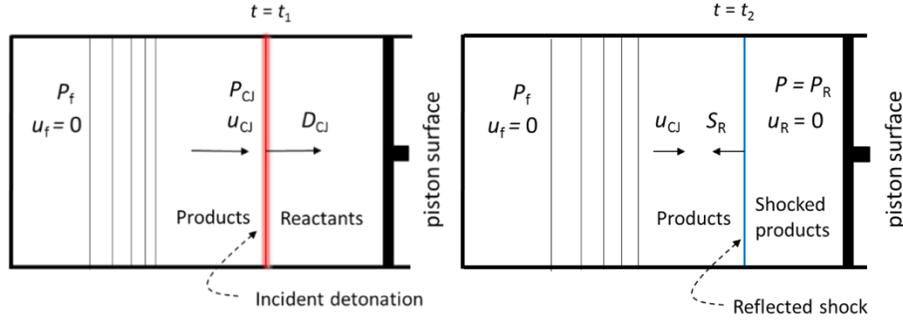
Figure 4.3 A sketch showing different gas dynamic states of the detonation reflection process

The detonation propagates at D_{CJ} into the unburned reactants and impinges upon the plunger of the injector module at $x = L$. The detonation wave reflection results in an even higher pressure on the injector's piston. The resulting maximum pressure occurring at the moment of reflection can be estimated using a simple gas dynamic analytical model based on the Rankine–Hugoniot equations for a constant-γ ideal gas Stanyukovich (1960), Shepherd *et al.* (1991), i.e.:

$$\frac{P_{R0}}{P_{CJ}} = \frac{5\gamma + 1 + \sqrt{17\gamma^2 + 2\gamma + 1}}{4\gamma} \qquad \text{Eq. (4.1)}$$

where P_{CJ} is the CJ detonation pressure, P_{R0} the immediate reflected-detonation shock pressure, γ the ratio of specific heats. Taking an average $\gamma = 1.275$ at the detonation CJ state, $P_{R0} \approx 2.54 \, P_{CJ}$. The CJ pressure and reflected pressure versus initial pressure of the combustible are plotted in fig. 4.4 shown by dotted and solid lines, respectively.

Due to the solid boundary at $x = 0$, a non-steady expansion wave—also referred to as the Taylor–Zel'dovich wave—follows behind the detonation lowering the pressure and temperature to match the boundary conditions. As shown in studies conducted by Karnesky *et al.* (2013), Beltman *et al.* (2002) and more recently by Damazo *et al.* (2017), the immediate reflected pressure P_{R0} will decay exponentially toward the final expansion pressure, i.e.:

$$P_R(t) = \left(P_{R0} - P_f\right)exp\left[-\frac{t}{\tau}\right] + P_f \qquad \text{Eq. (4.2)}$$

where τ is a time decay constant and $P_R(t)$ asymptotes to P_f within the typical injection period. P_f is the pressure behind the Taylor–Zel'dovich wave, which can be calculated using the isentropic relationship across the expansion:

$$P_f = P_{CJ} \left(\frac{c_f}{c_{CJ}} \right)^{2\gamma/(\gamma-1)} \qquad\qquad \text{Eq. (4.3)}$$

where the sound speed c_f can be obtained by noting $u_f = 0$ at $x = 0$ end wall and using the Riemann invariants along the C^- characteristics for the detonation:

$$\Gamma_- = u_{CJ} - \frac{2c_{CJ}}{\gamma - 1} = -\frac{2c_f}{\gamma - 1} \qquad\qquad \text{Eq. (4.4)}$$

where u_{CJ} is the flow velocity immediately behind the detonation. According to the Chapman–Jouguet criterion, u_{CJ} is equal to the detonation velocity D_{CJ} minus the sound speed at the CJ state, c_{CJ}. Hence:

$$c_f = \frac{\gamma + 1}{2} c_{CJ} - \frac{\gamma - 1}{2} D_{CJ} \qquad\qquad \text{Eq. (4.5)}$$

The expansion pressure P_f is also plotted in **Fig. 4.4**, given by the dashed line. The initial reflected shock pressure P_{R0} provides a sufficiently large driving force to punch the skin and generate the injection jet with high inertia and pressure after the expansion process P_f for the rate constant drug delivery.
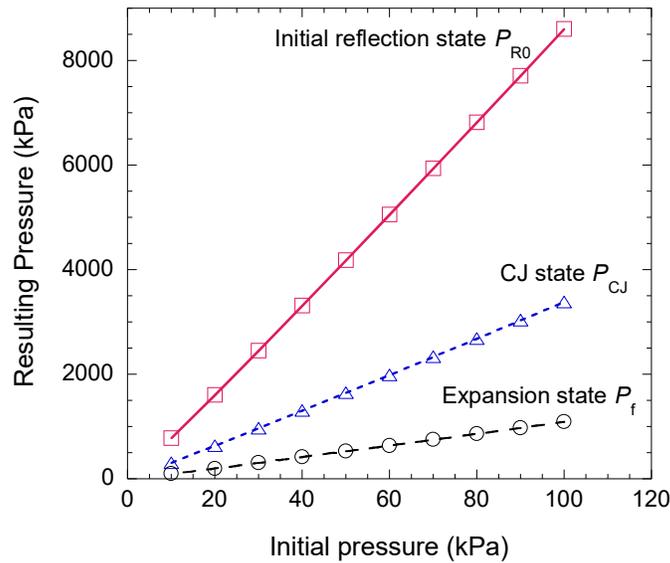
Figure 4.4 Incident Chapman–Jouguet (CJ) detonation pressure, reflected pressure and expansion pressure for stoichiometric C₂H₂/O₂ mixture at various initial pressures

To model the jet evolution and obtain its flow properties, a model was developed by Baker and Sanders (1999) by performing a mass balance and force analysis on the injection device. Assuming that the water is incompressible, the jet pressure can be described by integrating the following expression:

$$\frac{dP_{jet}}{dt} = \frac{(B + P_{jet})\frac{dx_p}{dt} - \frac{BA_o}{A_p}\sqrt{\frac{2P_{jet}}{\rho_o}}}{L - x_p}$$

Eq. (4.6)

where the piston acceleration driven by the detonation wave reflection is given by the following equation of motion derived from a force balance:

$$\frac{d^2x_p}{dt^2} = \frac{A_d P_R(t)}{M_p} - \frac{A_p P_{jet}(t)}{M_p} - \frac{F_{O-rings}(t)}{M_p \left|\frac{dx_p}{dt}\right|}\frac{dx_p}{dt}$$

Eq. (4.7)

It consists of the driving force generated by the reflected shock pressure in Eq. (4.2), the fluid pressurization, as well as frictional losses due to the O-ring sealing in the plunger, $F_{O\text{-rings}}(t)$. The latter term is difficult to model because the frictional forces due to O-ring sealing consist of a complex phenomenon as there are many factors in play that have reciprocal influence Portaro and Ng (2015), Nakayama *et al.* (2015). To simplify the modelling, $F_{O\text{-rings}}(t)$ is obtained through the following phenomenological approach:

$$F_{O-rings}(t) = F_s \cdot H(t_R - t) + \beta \cdot P_R(t) \cdot (1 - H(t_R - t))$$

Eq. (4.8)

where $H(t_R\text{-}t)$ is the Heaviside function and t_R is a time constant. The frictional force takes on this simple expression with the first term modeling the separation friction F_s, which consists of an initial force that is overcome under the initial high load in order to break static friction and generate piston movement. The second term is required for diminishing friction after the piston reaches the sliding value once static friction is overcome.

4.3 Results and Discussion

The results of the injection process using the combustible mixture at an initial pressure ranging from 25 kPa and 50 kPa are given in **Fig. 4.5**. Overall, the pressure profiles shown in the figure reveal a typical needle-free liquid jet evolution with a damped oscillatory behavior. For comparison, a black-colored pressure trace obtained in study conducted by Portaro and Ng (2015) using an air-powered injector is shown in **Fig. 4.6** and similar damped harmonic oscillations can be seen between these two results. However, due to a more severe piston driving condition by the gaseous detonation wave, the damping rate primarily due to friction forces by the O-ring seal and other losses is slower. The more pronounced oscillatory dynamics when compared to the air-powered injection system can also be attributed to the resonant oscillations induced by the multiple wave reflections transmitted from the piston to the water column and impedance mismatch. Nevertheless, a pressure peak is seen upon the detonation wave impacting and driving forward the injector's piston. Subsequently, the jet pressure decays but oscillates. As previously described by Arora *et al.* (2007), it is the initial pressure peak which is important in the formation of a fracture in the skin and the subsequent stabilization to the average delivery pressure determines the depth at which the medication is delivered.
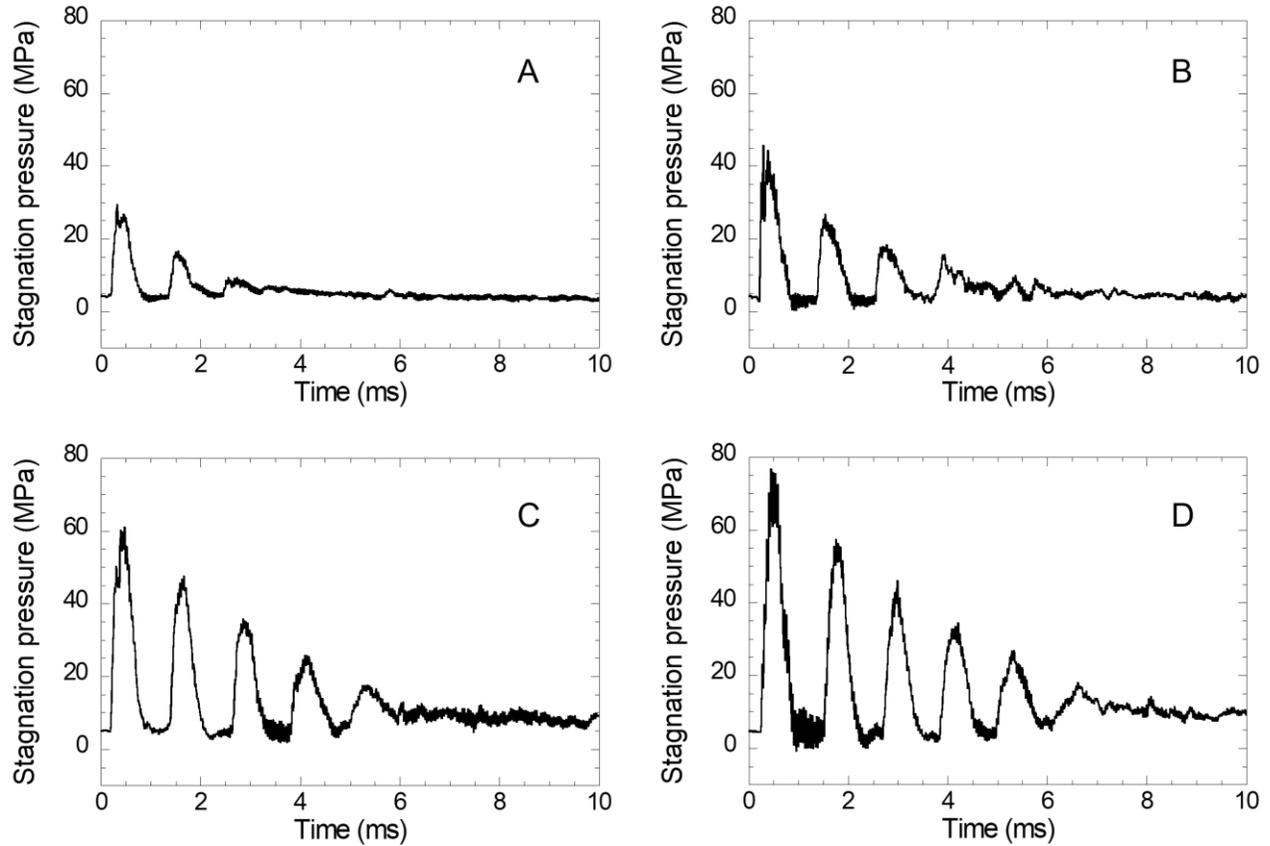
Figure 4.5 Sample pressure traces from the experiment with combustible initial pressures of (a) 25 kPa; (b) 30 kPa; (c) 40 kPa and (d) 50 kPa

By increasing the initial pressure of the combustible, hence the pressure across the detonation wave and the reflected detonation-shock, some change in the dynamic behavior of the jet pressure can be observed. Clearly, a longer injection duration can be achieved by increasing the initial pressure also shown by an increasing number of oscillation cycles. At high initial combustible mixture (i.e., above 40 kPa), the injection pressure can be maintained at a sufficient level for a reasonable time duration, at least 5 ms for the present setup. The pressure oscillates with decreasing amplitude around a mean value over a long period of time, which is referred to as the average injection pressure.

By numerically approximating the solutions of Eqs. (4.7) and (4.8) and using experimental data to determine necessary fitting parameters (i.e., $\tau = 300$ µs similar to the value given by Karnesky *et al.* (2013); $t_R = 0.4$ ms; $F_s = 1000$ to 2800 with increasing initial pressure and $\beta = 2.0 \times 10^{-4}$ for O-ring seals), Figure 4.5 depicts the jet pressure evolution predicted from the analytical model for

the combustible initial pressures of 30, 40 and 50 kPa. The experimental results (plotted as dotted curves) are also included for comparison in **Fig 4.7**. In general, the model result demonstrates good agreement with the experimental data. The oscillatory evolution, as well as the two main jet properties namely the peak and average stagnation pressures were captured clearly by the model and the values are quantitatively close to the experimental measurements. However, it is important to note that due to the simplicity of the empirical friction model for O-ring seals used in this work, the oscillations cannot be simulated precisely. In order to capture these oscillations (or experimentally eliminate these oscillations), all sources leading to the damping need to be carefully investigated and modeled.
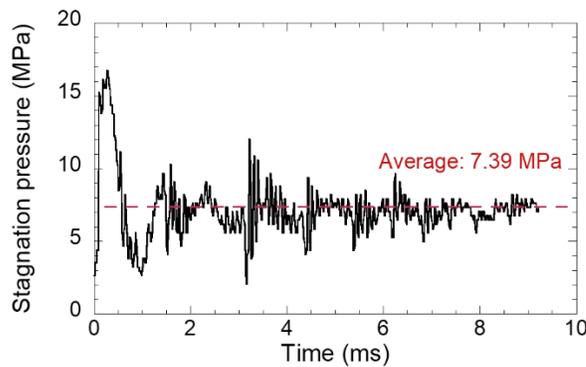
Figure 4.6 A picture of the in-house air-powered injector and sample pressure trace taken from the study conducted by Portaro and Ng (2015) with a driving pressure of 413 kPa and orifice nozzle diameter of 200 μm. The pressure was obtained using a different force sensor
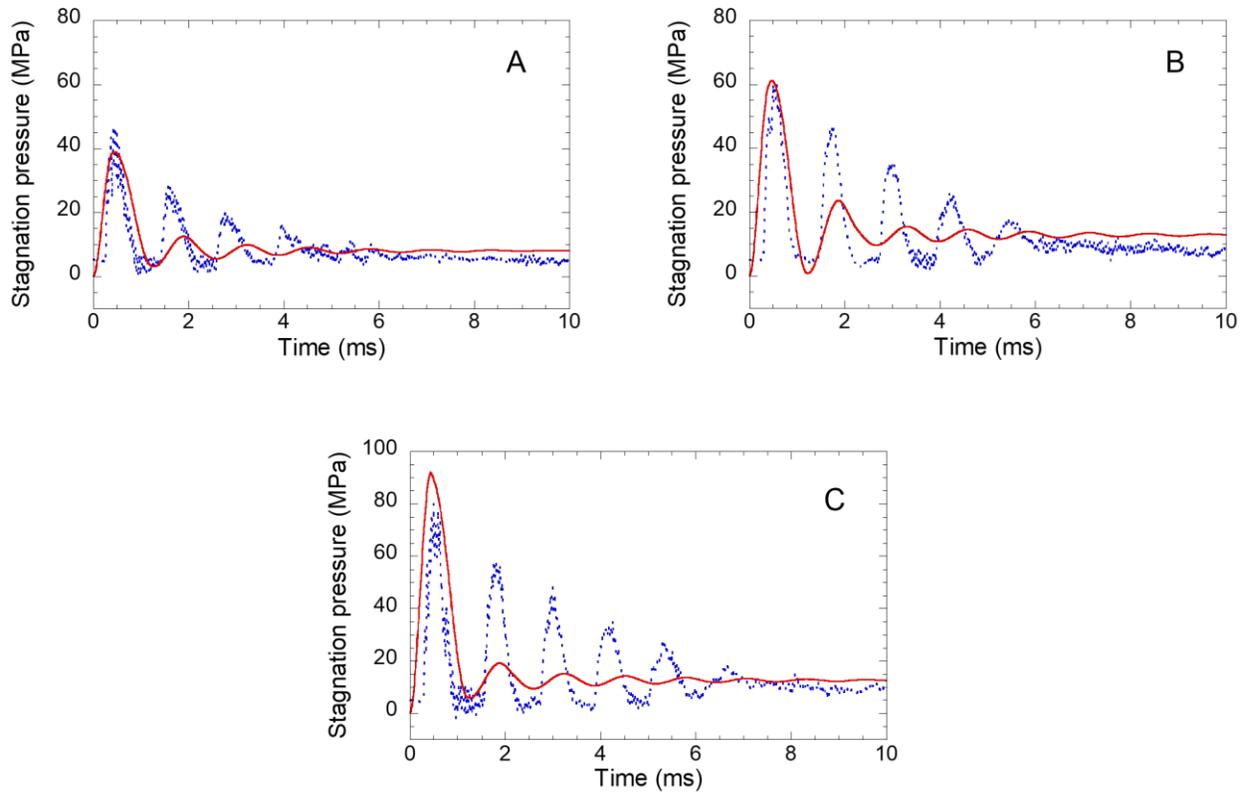
Figure 4.7 Stagnation pressure evolution from the analytical model with combustible initial pressures of (a) 30 kPa; (b) 40 kPa and (c) 50 kPa

It is worth noting, that unlike the water hammer effect proposed by Ghidaoui *et al.* (2005) and Kumar *et al.* (2018), which describes pressure variations in a pipeline of which the pressure wave dynamics and damped oscillatory behavior can be accurately obtained using the method of characteristics, the present liquid jet injection phenomenon also involves a detailed analysis of complete system dynamics, i.e., the fluid-structure interaction between the rapidly moving piston, water column and the flow behind the reflected shock, after the detonation impact. Typically, the water hammer effect is a result of a rapid closing of valves in a flow stream, causing a pressure wave to propagate upstream in the pipe. For such a situation, the numerical solutions to the water-hammer equations governing the propagation of the pressure surge can predict the wave velocity and damping of the pressure oscillations. It is worth mentioning that an equivalent analysis has been considered by Baker and Sanders (1999), referred to as "*wave analysis*". This study illustrates that the wave analysis results were only valid over a very short time span, i.e., the short duration over which the first pressure spike occurs and when piston movement is negligible and assumed to be zero. Unlike the water-hammer effect, the present phenomenon involves piston acceleration

to a high velocity which is no longer negligible, and the water-hammer equations are not sufficient to describe the full dynamics of the injection pressure profile evolution. The continuum analysis detailed by Baker and Sanders (1999) has become a standard model with continuous improvement for different types of needle-free liquid injection devices driven by a high-velocity plunger, examples of this can be found in studies conducted by Chen *et al.* (2011), Portaro and Ng (2015), Williams *et al.* (2016) and Chen *et al.* (2017), and is also used in this work. It is important to note that the oscillatory behavior, i.e., both the amplitude and damping of the jet pressure variation are not simply wave dynamics within the liquid column, moreover, they do not solely depend on the liquid acoustic and thermodynamic properties. The oscillatory behavior is a result of system dynamics, which must be modeled considering piston movement caused by the driving force and subsequently countered by the frictional and fluid forces which arise due to the piston movement. These effects are taken into consideration in the continuum analysis, although more accurate quantitative sub-models, e.g., O-ring seals and piston driving force by the detonation wave, are needed to precisely capture the damping of the jet pressure oscillation. Despite the simplicity, the model does capture the two main jet properties, namely, the peak and average stagnation pressure values, and the period of oscillations correlate well to experimental observations. Qualitatively, in previous work conducted by Portaro and Ng (2015) the effects that strongly influence damping are identified. The friction from sealing is found to be dominant and the oscillations are caused primarily by the piston dynamics. Nevertheless, the liquid viscosity, as can be seen in this study, is also another damping parameter which affects the oscillatory behavior, this has been previously discussed in **Chapter 2**. In order to further improve the continuum analysis and obtain more accurate predictions of the jet pressure oscillation, future work will implement an improved quantitative description of the arising frictional force due to the O-ring seals and the detonation reflection process interacting with an accelerating piston.

The pressure traces from both the experimental measurement and analytical results depict both the peak and average jet pressures for different acetylene-oxygen gas mixtures and initial pressures, as can be seen in **Fig 4.8**. The solid line represents the analytical model results. For each initial pressure condition, at least five experimental shots were performed. From **Fig. 4.8**, it is easily observed that using a detonation-driven controlled release mechanism, the peak stagnation pressure values achieved are much larger than those obtained by air-powered or spring-loaded injectors, that are typically limited in the range below 50 MPa. It is also worth noting that Shergold

et al. (2006), reported a threshold of 15 MPa is required before the jet is able to penetrate into human skin. The present detonation-driven injector easily reaches this threshold and in fact provides initially a much stronger penetration capability compared to the conventional air-powered or spring-loaded devices. The stagnation pressure also makes the computation of jet velocity over the diameter of the orifice possible by using the Bernoulli's equation $V_{jet} = (2P_{jet}/\rho_o)^{1/2}$. The peak jet velocity and average injection velocity correspond to approximately 250–420 m/s and 130–190 m/s range, respectively.

As discussed previously, modeling the frictional losses due to the O-ring seal is very challenging. The high-pressure loading condition due to the detonation reflection, experienced by the piston mechanism, makes it difficult to establish an exact expression for the level of friction involved and explain the noticeable discrepancy observed in **Fig. 4.8** at higher initial pressures. In fact, the average injection pressure is closely related to the piston displacement and a better agreement can perhaps be achieved by modeling the dynamic friction as a function of the piston velocity. This constitutes future work to improve the accuracy of the present modelling approach.
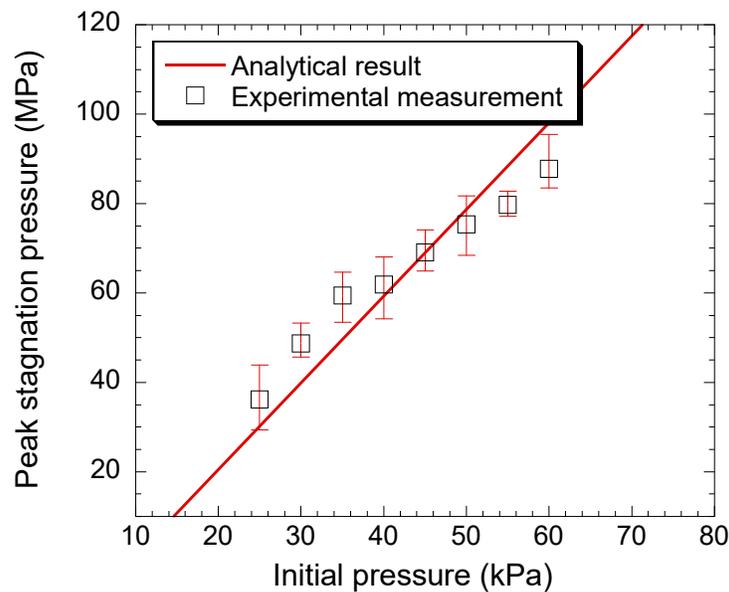
(**a**)
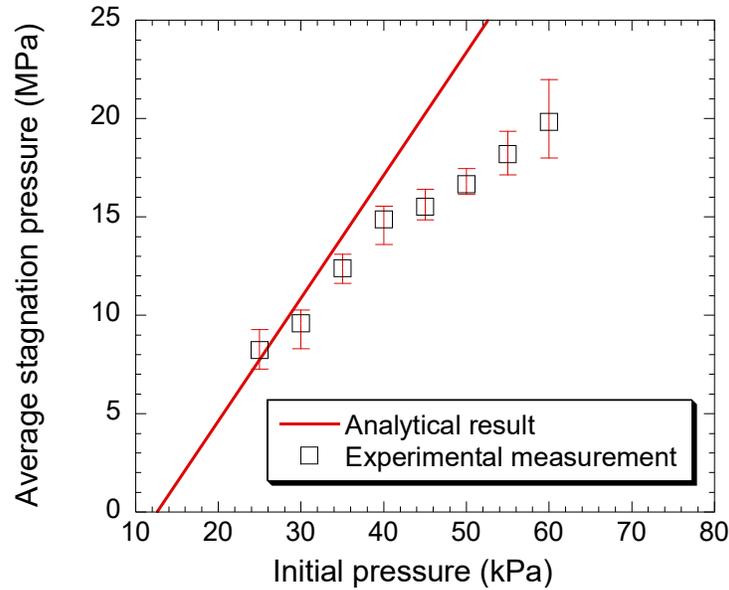
(b)

Figure 4.8 Results of the (a) peak pressure; and (b) average stagnation pressures as a function of the combustible initial pressure, respectively. The solid lines represent the model results

Furthermore, for the average stagnation pressure driven later, by the state behind the Taylor wave expansion, the experimental measurement in general agrees well with the modeled results in the initial pressure range of 25–40 kPa. Note that in the present study, a constant value of the time decay τ is used to obtain the model solutions (see Eq. 4.2). The reflection time decay may differ and also should be a function of the injector dimension (i.e., length) and initial pressure of the combustible mixture. Further pressure measurements inside the tube are also needed to accurately determine the time decay constant.

Injections into a 60-mm thick ballistics gel with a bloom number of 250 are also performed to visualize the resulting injection and demonstrate the ability of the detonation-driven injector device for deep penetration. Similarly, five experimental shots at each initial pressure are carried out. The results are shown in **Fig 4.9**, which seem to depict a linear trend for penetration into the ballistic gel as a function of initial mixture pressure. It is worth noting, that in this study, all the liquid dose in the injection chamber is administrated. The consistent penetration depths from each shot and each condition provide an indication that repetition of injection dosage into the gels is achieved.
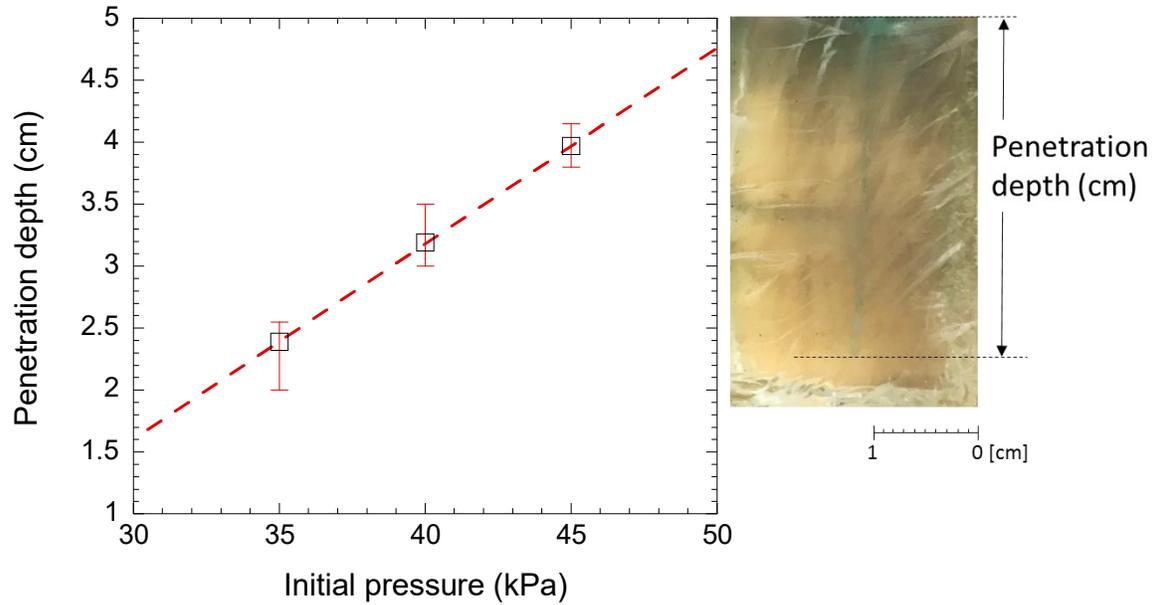
Figure 4.9 A liquid jet injection by the present detonation-driven injector device into a bloom 250 10% wt. gel as a function of mixture initial pressure

It is worth noting that the motivation for this study is to design an injector capable of injecting highly viscous liquid. In order to verify the viability of using the present detonation-driven needleless injection concept, tests using mixtures of glycerol/water in the injection are performed. The tested solutions are 30%, 50% and 70% glycerol by weight. Sample jet stagnation pressure evolutions using a combustible initial pressure of 40 and 45 kPa are illustrated in **Fig. 4.10**. Overall, the injection dynamics do not vary significantly when compared to water (see **Fig. 4.5**), despite a decrease in the peak stagnation value. Similar dynamic behavior is also observed by further increasing the glycerol content and when using a high initial combustible pressure for detonation, as shown in **Fig. 4.11**. The main effect of viscosity with the increase of glycerol only decreases the jet stagnation pressure. The variation of peak and average stagnation pressures as a function of % glycerol in the tested liquid solution are plotted in **Fig. 4.12**. It illustrates that the addition of glycerol content decreases the jet stagnation pressure approximately linearly due to the effect of increasing viscosity as verified numerically in chapter two.
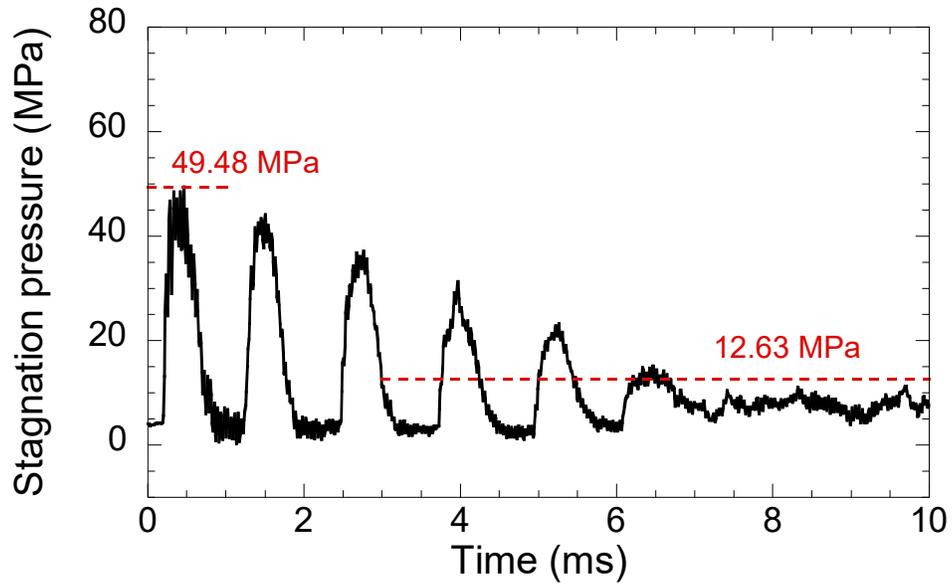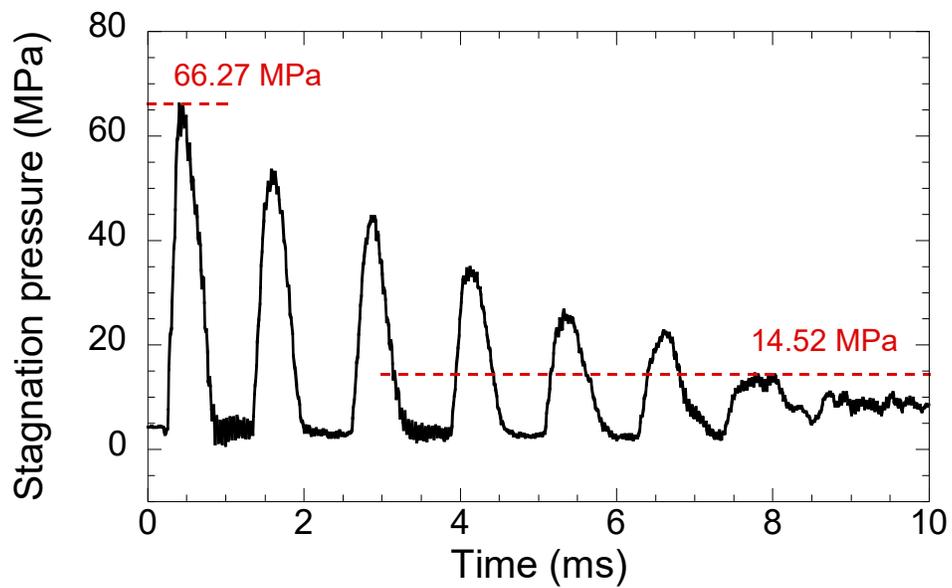
Figure 4.10 Injection of a solution with 30% (by weight) glycerol using the present detonation-driven injector device with (a) 40kPa and (b) 45 kPa initial combustible pressure.
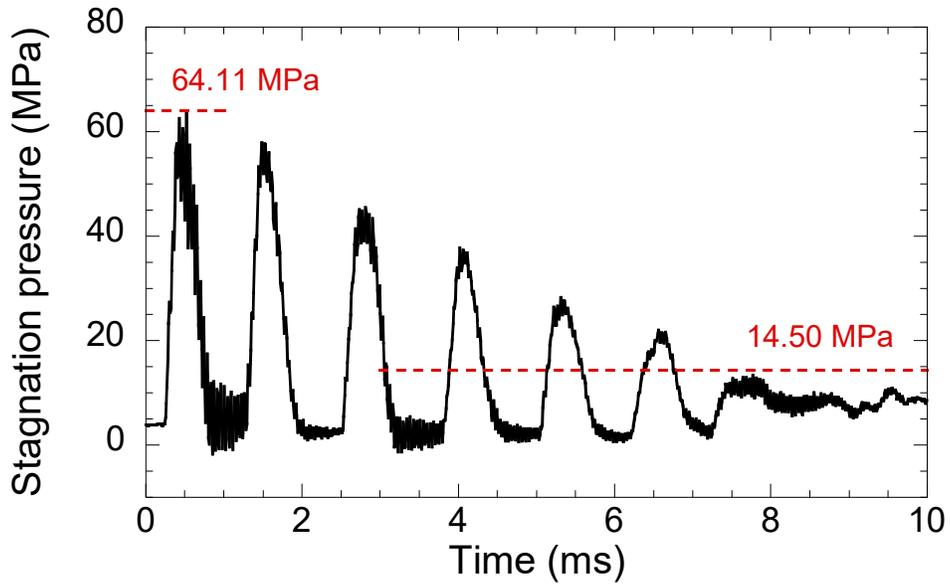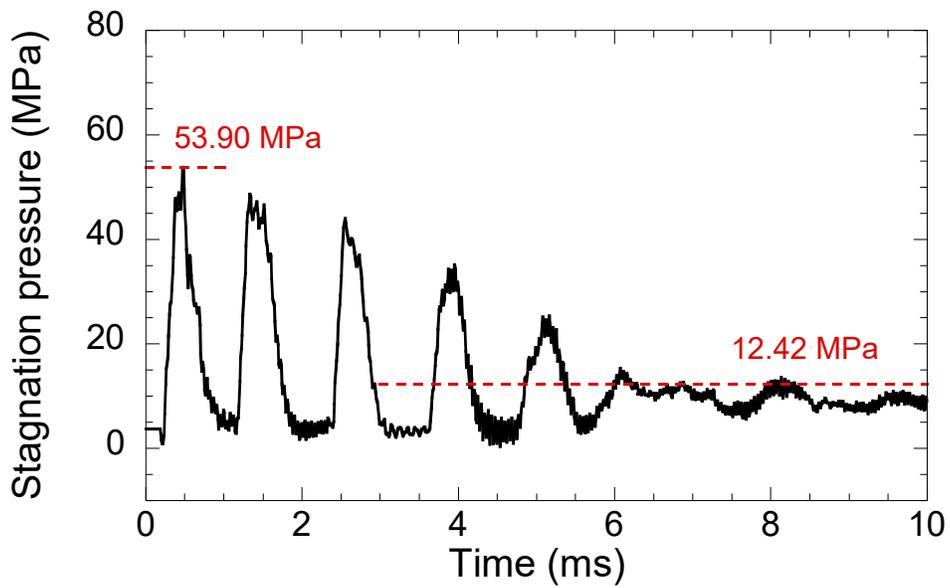
Figure 4.11 Injection of a solution with (a) 50% (by weight) and (b) 70% glycerol using the present detonation-driven injector device with an initial combustible pressure of 45 kPa.
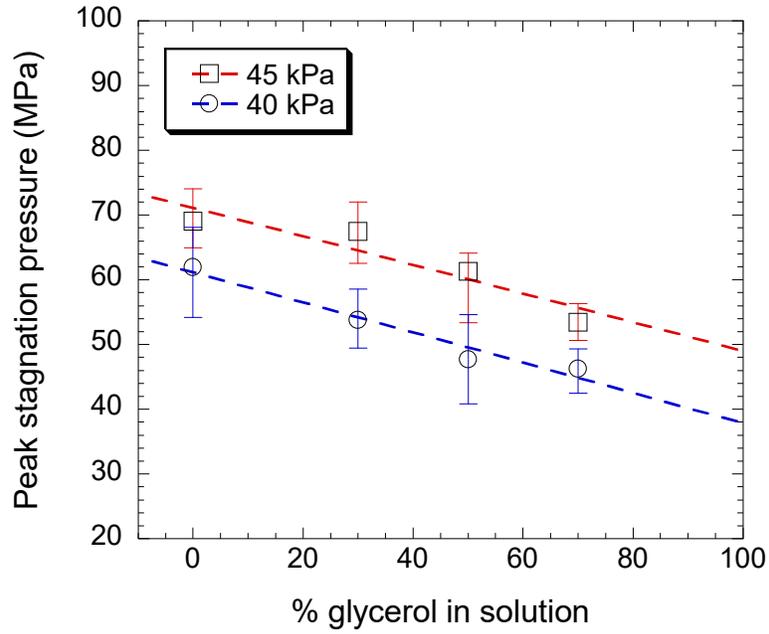
(**a**)
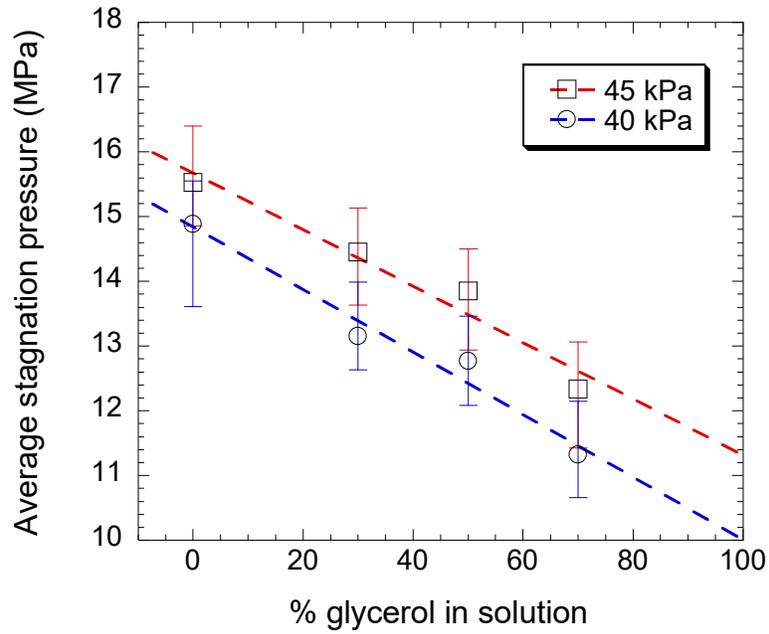
(**b**)

Figure 4.12 Results of the (a) peak pressure; and (b) average stagnation pressures as a function of the % glycerol in the solution, respectively. The dashed lines show the trend lines of the experimental results

4.4 Sources of Error

Although the experimental results illustrate a good agreement with theoretical modeling, there exist a few sources of error which can be addressed in future work. It is important to note that the error bars displayed in the various figures consider minimum and maximum values of both peak and average stagnation pressures. One of the primary sources this error can be contributed to the difficulties in modeling friction. Separate studies should be conducted in order to properly quantify the variation of frictional forces caused by the O-ring seals in the device. The O-ring seal of the driver piston should be particularly examined, as the circumference of this component is significant when compared to the overall scale of the device and as such will impart large amounts of both static and dynamic friction. It was observed that the seals required lubrication daily due to the heat from the detonative combustion, burning off the lubricant film on the wall of the driver chamber over time. Slight changes in fitment and wear on the O-ring resulted in large discrepancies in stagnation pressures.

Similarly, as explained in **Chapter 3** the measurement of pressure traces also contributed to mismatch between experimental and modeled results. The force transducer must be operated with a standoff distance in order to avoid flutter in the resulting waveforms. This implies that the jet will experience divergence, upon impinging on the force transducer, although the use of high-speed photography made it possible to observe that the divergence was minimal, quantifying the amount was not possible. Therefore, the nominal nozzle orifice diameters were used when converting from force values obtained by the transducer to stagnation pressures. Future work can consider a study which characterizes the jet diameter over a range of standoff distances in order to reduce the conversion error from force to stagnation pressure.

4.5 Summary

This study highlights the use of the detonative combustion phenomenon as a novel, alternative energy source to power a conventional mechanical piston-type NFJI. The comparison with jet pressure measurements of standard air-powered needle-free injectors, illustrates that the detonation-driven device provides equivalent jet injection evolution. However, taking advantage of the pressure rise across a detonation, the combustion-driven device can provide driving forces much larger than those obtained by typical air-powered or spring-loaded injection devices.

Moreover, this study provides promising evidence that a gaseous detonation wave can generate sufficient power to drive a needle-free injector, producing a strong liquid jet applicable to highly viscous injectables, and meeting the requirements of recently emerging medical treatments. Ongoing work includes the characterization of the jet as a function of the detonation properties, using a number of combustible mixtures at different initial conditions and its evolution with increasing fluid viscosity. Furthermore, in order to improve both the device performance and modelling output, it is crucial to investigate in more detail the damping caused by various sources and develop a more complete model to describe all the friction losses in the system.

For proof of concept, this study relied on the initiation of the detonation wave via direct initiation by a high-voltage capacitor discharge and the use of a large-scale device. The feasibility of scaling or miniaturizing such a device for practical applications is possible. Recent studies conducted by Wu *et al.* (2007; 2011) and Han *et al.* (2017), which describe the flame acceleration and the deflagration-to-detonation transition (DDT) in microscale tubes provide techniques to develop a miniature detonation-driven NFJIs. Consequently, minimizing the influence of viscous effects and heat losses to the walls becomes the key issue for practical use of this proposed technique. Although the detonation wave provides ample power output to cope with increasing viscous injectables, and varying the initial amount of detonative mixture allows control over peak and average stagnation pressures, real-time control of the pressure output cannot be obtained. The development of future power sources should also consider methods of combining the rapid energy release, power and scalability of detonative techniques with the ability to exhibit real-time control over jet stagnation pressure.

Chapter 5 : Conceptual Design of Servo Screw Driven Injector

5.1 Rotary Motion for Driving Liquid Jet Injectors

The delivery of medication by liquid jet injection explored in this research work has been accomplished with power sources that create linear motion via the rapid release of energy, such as gas-powered and combustion-driven devices, or using linear motors. Although the production of liquid jets by the rapid release of energy lacks real-time controllability, the liquid jet injectors utilizing these power sources can be scaled well for practical applications. Moreover, as was illustrated in chapter three, the use of linear motors combined with modern-day power electronics provides an accurate way of controlling an output pressure. However, the forces required for liquid jet injection, as well as the delivery of larger volumes, can make it difficult to practically scale these devices for clinical use. Consequently, it would be of great interest to develop a controllable power source that can provide the same accuracy as linear motors and exhibit the rapid energy release and scalability of gas/combustion-driven injectors. An interesting concept that has been explored by Zhang *et al.* (2014), illustrated in **Fig. 5.1**, utilizes a brushless DC motor that drives a lead screw, which in turn converts the rotary motion of the motor to linear motion.
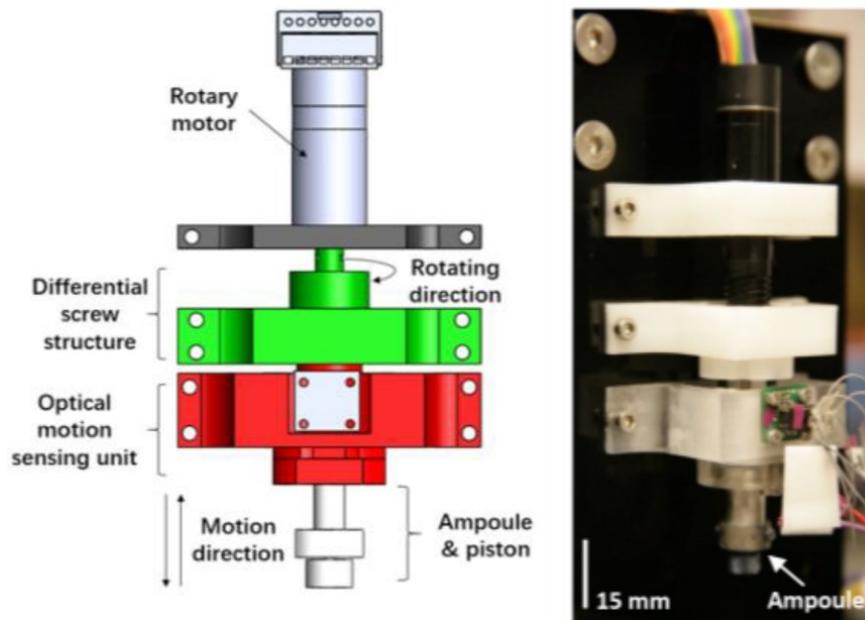
Figure 5.1 Screw driven prototype (Zhang *et al*., 2014)

This preliminary prototype is controlled using six-step PWM modulation as well as an optical sensor to track the displacement of the drug ampoule, and correspondingly change the motor frequency to obtain a desired jet stagnation pressure. Preliminary results from this study demonstrate that the device could deliver small volume injections and produce jets with up to 300 m/s velocities. However, the study did not provide results that underline the accuracy of the device. Furthermore, 450 watts of power with and an initial inrush current of 15 amps was required to provide injections with delivery volumes of less than 10 µl. The large currents and power requirements for a relatively small device and delivery volumes make it difficult to scale for larger volumes and viscous injectables. Nevertheless, the concept of using a rotary motor and a mechanical drive to create linear motion is a powerful tool that can be utilized to provide both power, accuracy, and scalability to future liquid jet injector designs. The following section will focus on the design of a screw-driven injector that builds on the work proposed by Zhang *et al.* (2014).

5.2 Development of Servo Powered Rotary Liquid Jet Injector

One of the key attributes of a power source used to drive a liquid jet injection, is the ability to deliver a sudden impulse force that creates accelerations typically exceeding 2G. Power sources that store energy such as gas-powered, air-powered, and combustion driven, can release a sudden burst of energy when triggered, however the electronically controlled counterparts must accelerate from rest in a very rapid and controlled manner. This creates complexities which lead to larger motors, control electronics capable of handling large in-rush currents and complex control techniques necessary for accurate jet production. Decoupling the startup phase from the initial plunger motion would make it possible to reduce the size of the power electronics as well as the power requirement of the motors. Controlling the interaction between the plunger motion and motor rotation will make it possible to utilize smaller motors and gently accelerate them to a desired operating speed which can also be optimized for maximum torque delivery.
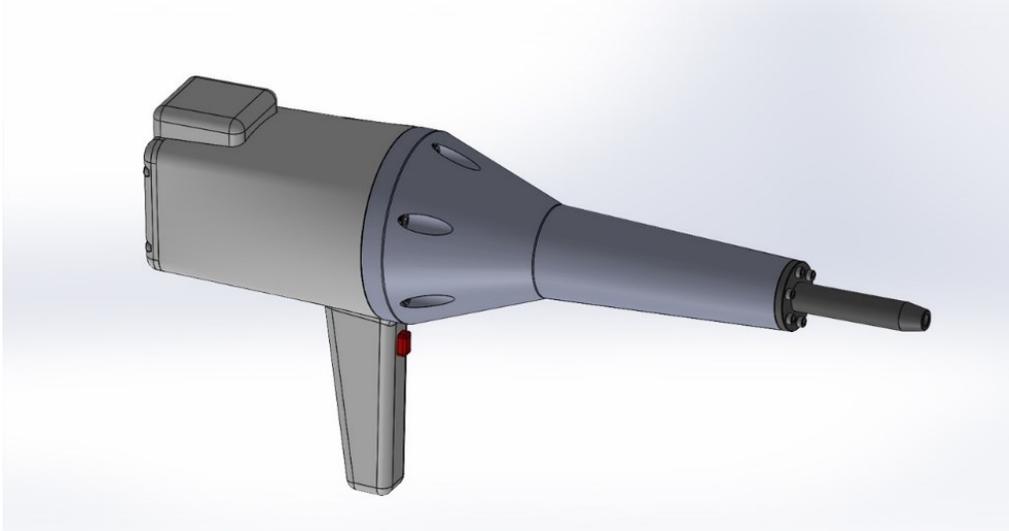
Figure 5.2 Novel high-power screw driven injector

Figure 5.2 illustrates a novel prototype screw driven injector, using electromagnetism to decouple a high-speed low inertia servo motor from a drive screw. In so doing, it is possible to achieve the controlled application a sudden impulse force as is characteristic of conventional jet injectors.
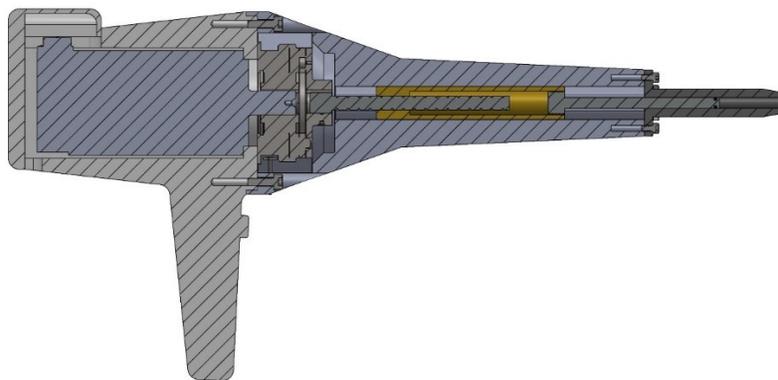
Figure 5.3 Cross-section of screw driven injector

Figure 5.3 depicts an exploded view of the proposed screw-driven injector, it consists of four major subgroups: AC servo motor and control electronics, an electromagnetic clutch, a linear motion group containing a drive screw, drive nut and guiding mechanism, as well as an injection

group containing a plunger and injection chamber assembly. In order to decouple the initial motor startup, an electromagnetic clutch is added between the motor and the screw used to drive the injection forward in a linear manner. The clutch allows the servo motor to ramp up to the desired operating speed without producing any displacement of the lead screw or plunger. The clutch accomplishes this action by separating the motor and drive the screw through an air gap. Once the operating speed is obtained the clutch's armature, containing an electromagnet is energized, making use of the Lorentz force principle to pull in a rotor coated with friction material and connected to the drive screw. This establishes a rigid coupling between the motor and screw allowing torque transfer to occur and the injection process to proceed.
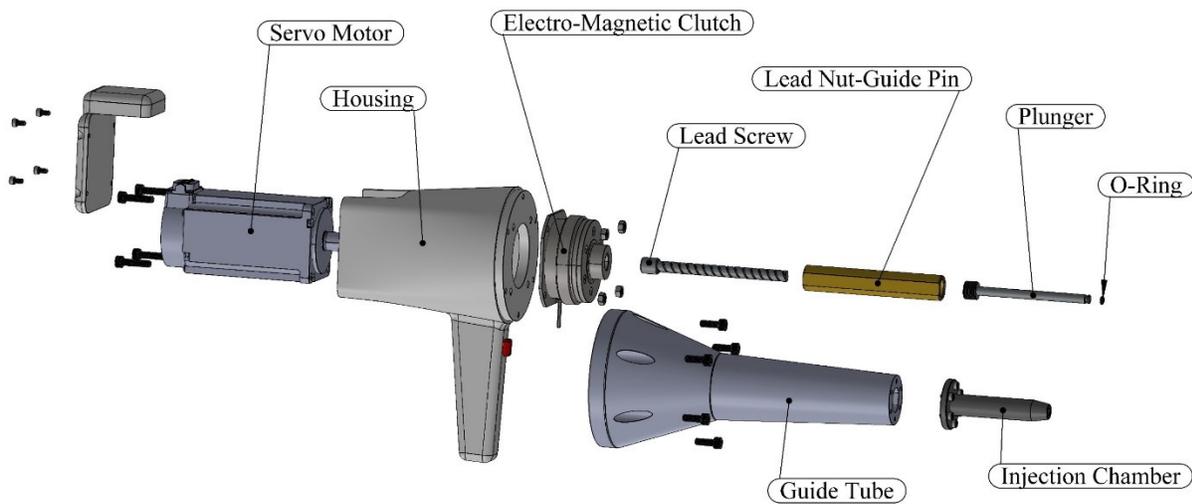
Figure 5.4 Exploded view of screw driven injector

Once the clutch has been energized the servo motor can then maintain the proper plunger velocity by utilizing the same control techniques described in **Chapter 3**. Moreover, due to the prevalence of AC rotary servo motors in motion applications, complete motor control systems which exhibit very rapid response times, low inertia and high speeds are now commonplace and provide a very efficient way to power the proposed screw-driven injector. The motor is coupled to a miniature electromagnetic clutch, this technology has been developed over the years and provides an efficient means of torque transfer, units capable of exhibiting zero slip conditions in less than 5 ms and driving torques of up to 5 Nm are now easily obtained. The clutch drives a lead screw whose lead is determined in such a way to deliver the maximum plunger velocity, given the motor's

optimal speed band. Changes to plunger velocity are made by varying the rotational speed of the motor, and tracking the count from a rotary encoder, the encoder count is correlated to the screw lead via electronic gearing within the motor amplifier. The drive screw, drive nut and linear guide are integrated into one component as illustrated in **Fig. 5.4**, the shape of the guide pin consists of a circle with two flats on either side, and the matching shape is created within the guide tube. This feature prevents the guide pin from rotating on the drive screw while permitting the pin to translate axially, subsequently converting the thrust force generated by the drive screw into linear motion. The plunger is driven via the guide pin and pressurizes the injection chamber as is typical for liquid jet production. The compactness of this design helps minimize the total rotating mass and system inertia.
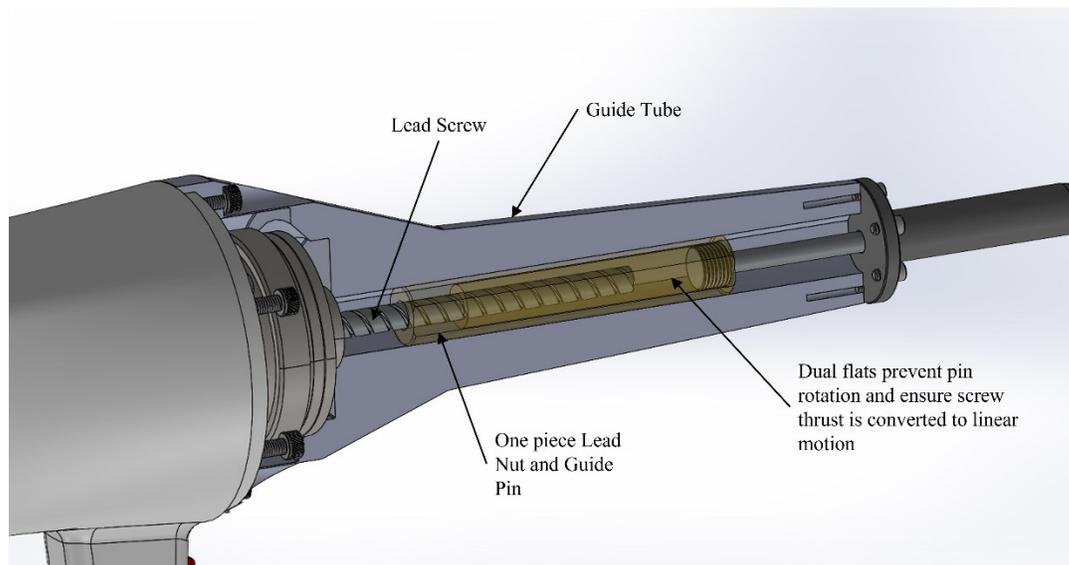
Figure 5.5 Linear motion group for screw driven injector

5.3 Sizing Components for Rotary Liquid Jet Injection

In order to perform proper sizing of each component of the screw-driven, liquid jet injector described in the aforementioned section, it is necessary to understand the maximum forces at play at the onset of plunger movement as well as the desired delivery volumes and targeted power. It was observed from previous chapters that the fluid must undergo pressurization of 15 MPa, within a few ms in order to produce liquid jets with enough momentum to cleanly puncture tissue. If the bore of 6.35 mm for the injection chamber from previous work is maintained in order to draw

comparisons, a thrust force of approximately 500 N is required. Moreover, if the Baker and Sanders (1999) model described in previous chapters is considered, a peak plunger velocity of 4 m/s is required to obtain a corresponding peak of 15 MPa within the first 5 ms of liquid jet injection. This will aid in defining both the motor and drive screw requirements, which are inherently linked by this type of injector construction. The proper sizing of the drive screw must consider the maximum plunger velocity V_{max}, in this case 4 m/s must be used in conjunction with the maximum operating speed of the motor Mf_{max} in rotations per second, with Eq. 5.1, in order to determine the lead l of the drive screw. The lead denotes the amount of axial distance traversed for one rotation of the screw.

$$\frac{V_{max}}{Mf_{max}} = l \qquad\qquad \text{Eq. (5.1)}$$

For a given maximal plunger velocity, the greater the motor speed, the smaller the lead distance of the drive screw. The lead distance is of particular importance as it will determine the torque requirement of the motor and define the manufacturability and performance of the screw. Equation 5.2 relates the screw lead l, the screw efficiency η and the force F_p exerted on the plunger by the fluid to the torque T_s required by the system. The efficiency η of the drive screw is prescribed by Eq. 5.3, and relates the friction coefficient between the two sliding materials μ to the lead angle of the screw α. In the case of the prototype design, the screw is to be manufactured from ductile iron and the nut should be made from bronze, this will result in a friction coefficient of .06 and display good wear characteristics (Budynas and Nisbett, 2014). The lead angle α, is determined by the arctan of the circumference of the drive screw and the chosen lead distance.

$$\frac{F_p \times l}{2\pi\eta} = T_s \qquad\qquad \text{Eq. (5.2)}$$

$$\frac{1 - \mu tan\alpha}{1 + \mu tan\alpha} = \eta \qquad\qquad \text{Eq. (5.3)}$$

For the purpose of this study a Mitsubishi HK-MT63 servo motor with a maximum speed of 10,000 RPM and 7 N·m of torque was selected, this results in a drive screw that must exhibit a lead of 25 mm per revolution in order to achieve the 4 m/s maximum plunger velocity. The motor torque required to deliver a liquid jet injection given an 8-mm diameter drive screw, and a screw efficiency of 85% is approximately 2.35 N·m. This is well below the torque output of the motor

and if successful, the motor sizing could further be reduced. It is also important to note that a single start 25-mm lead drive screw would result in a significant amount of dead space between subsequent crests on the screw. In order to overcome this issue and decrease the loading carried by a single- threaded screw, the injector utilizes a multi-start screw, with two threads spaced at a pitch distance of 12.5 mm apart. This enables the dead space to be reduced, the axial loading to be shared by both threads and the overall lead to be maintained. **Figure 5.1** depicts the variation of lead distance and pitch for screws with multiple starts.
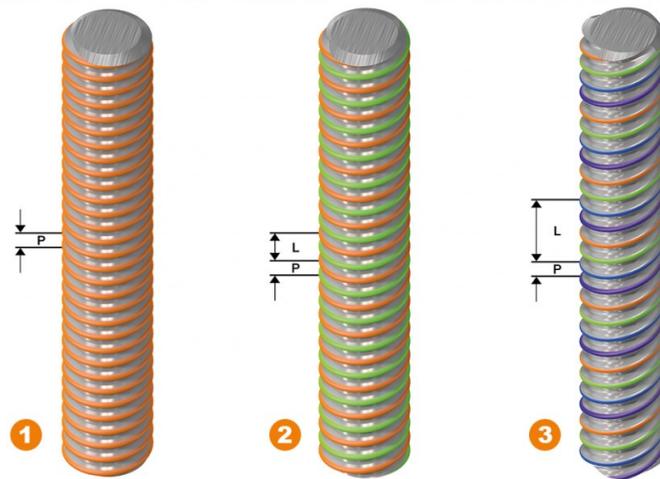
Figure 5.6 Multi-start screw (1) single start (2) double start (3) triple start (courtesy of Igus, 2022)

In order to provide the necessary motion, the screw is coupled to an electromagnetic clutch capable of transmitting the torque generated by the motor in order to propel the injection forward, but also the added torque created by the angular acceleration of the screw and coupling. This is evaluated by the dot product of the angular acceleration of the stationary assembly with the corresponding moment of inertia of that assembly. If the proposed design is considered the clutch must accelerate a mass of .15 kg with 1.2×10^{-6} kg-m^2 moment of inertia to 166 rev/s in a time interval of 5 ms. This results in an additional .250 N·m of torque, thus requiring that the clutch transfer 2.6 N·m of toque at the onset of plunger motion. There exists a plethora of miniature electromagnetic clutches which lend themselves well to the design of the proposed injector and operate within the force requirements and time scales of liquid jet injections. One such example is constructed by MIKI Pulleys whereby a 24V DC electromagnetic clutch can transfer a maximum of 5.5Nm of torque with transfer times of 20 ms to 80% of maximum torque. **Figure 5.6** depicts the construction and specifications of the selected clutch.
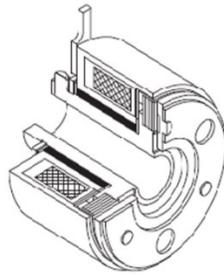
MIKI PULLEY 101-06-11	
Dynamic Torque	5.5 Nm
MAX. Speed	10 000 RPM
Mass	.46 Kg
Armature Pull-in Time	20 ms
Rotor Moment of Inertia	4.23×10^{-5} kgm^2

Figure 5.7 MIKI electromagnetic clutch specifications

Although the rated engagement time is 20 ms, it is common to use a technique known as over excitation, whereby up to three times the rated current is sent to the clutch armature to decrease transfer times. **Figure 5.8** depicts the typical torque versus time behavior, of particular importance is the actual torque build-up time (t_{ap}), which denotes the time required to achieve 80% of the maximum torque. From **Table 5.1**, the use of over excitation, can reduce this time to 5 ms. Moreover, the torque required to drive the injection forward is only 60% of the rated actual torque build-up, if **Fig. 5.8** is observed the behavior between torque vs time is linear within the build-up phase, and consequently the engagement time would be on the order of 3 ms. This works well to provide the same type of energy transfer as gas, spring, or combustion-driven devices, but in a controllable manner. Once the clutch and drive screw are in phase and exhibit no relative motion, then the motor control loop can ensure precise positioning of the plunger. The subsequent torque decay when the armature is no longer excited is also on the order of 5ms. This is also advantageous for pulsatile type injections, as the clutch can be actuated by a high-speed MOSFET, controlled by the same microcontroller providing motor control. The microcontroller can simultaneously change the motor frequency and track screw position as well as actuate the clutch, making it possible to create pressure pulses of varying length and frequency, in a much more controlled manner than what was exhibited in chapter three.

Clutch Size	Operating Time (ms)			
	t_a (Actual Engagment)	t_{ap} (Actual torque build-up time)	t_p (Torque build-up)	t_d (Torque decay)
101-06	8	5	13	5
101-08	9	8	17	8
101-10	10	10	20	11
101-16	18	16	34	23

Table 5.1 Clutch operating times invoking over-excitation
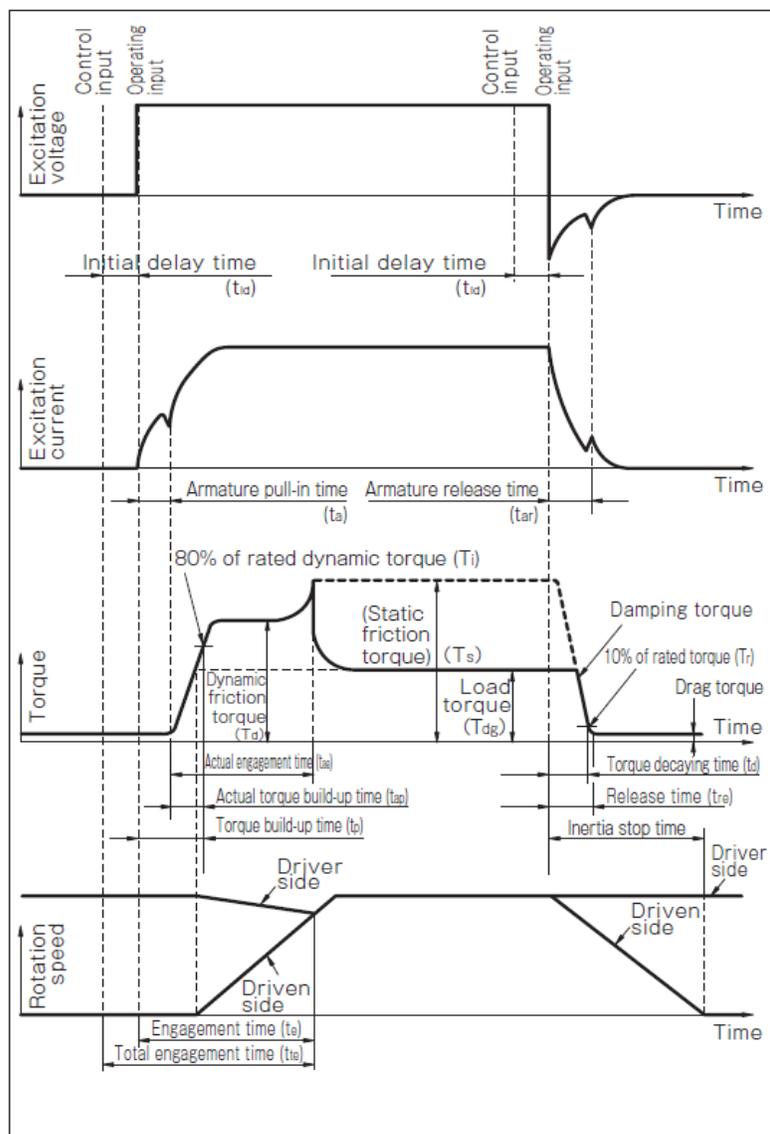
Figure 5.8 Operating time and control signals for electromagnetic clutch (MIKI Pulleys Inc, 2022)

5.4 Power Electronics and Control Scheme

The control and power electronics necessary for the screw-driven injector will take a similar configuration to those used in chapter three. A Xilinx Zync FPGA programmed with the same NC oscillator used previously, will provide a pulse train of the desired frequency, each pulse will correspond to an incremental angular displacement of the rotor shaft, and will be related to linear displacement by utilizing the drive screw lead distance l. The FPGA will provide both a pulse stream and direction signals to a Mitsubishi MRJ5-A motor amplifier capable of providing position control loop times below 32.5 μs. The drive will be coupled to an ultra-low inertia HK-MT63 servo motor, with a 26-bit encoder, capable of a maximum of 7 Nm of torque and 10 000 RPM. This setup should help in improving the response, stability, and precision of the system as both the motor and amplifier are specifically matched to provide optimal performance. The clutch will be powered by a 24V DC power supply fed through a custom circuit consisting of current control and high-speed MOSFET. This module will be controlled by the FPGA, and enable precise and repeated modulation of torque transfer, as well as permitting over excitation of the clutch armature, in order to minimize torque build-up times. The module will also contain a varistor, to deal with the remanent surge current in the windings of the armature caused by powering off the DC supply. For the clutch used in this application the surge voltage can reach 1000 VDC, and thus must be drained through a varistor to the ground to ensure the rapid torque decay and prevent damage to the winding insulation. **Figure 5.9** illustrates the control scheme and the relationships between the major components, it should be noted that once initial testing is accomplished and the concept is proven, an LVDT can be added to track the velocity and position of the guide pin and plunger assembly. This can be used to verify the accuracy of the motion transfer between the clutch and servo motor. Moreover, testing can be performed using the LVDT as feedback for a secondary position/velocity loop, to verify if stagnation pressure accuracy will benefit from this addition.
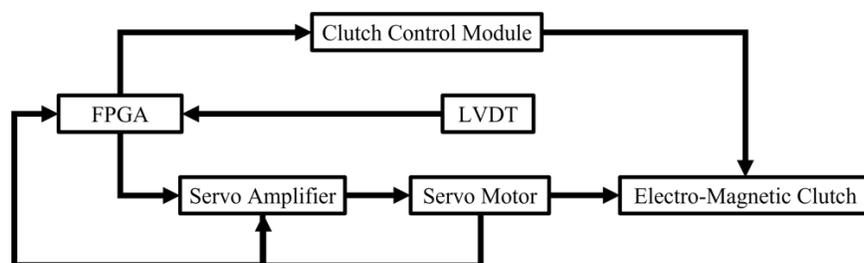
Figure 5.9 Block diagram illustrating control scheme for screw driven injector

5.5 Pressure Profile Generation

The motion profiles used by the FPGA will be generated utilizing the same techniques invoked in chapter three, which rely on the Baker and Sanders model, that relates plunger velocity and displacement to fluid pressurization. **Figure 5.10** depicts the expected output pressure of the device utilizing a 3 ms torque transfer, from **Fig. 5.8**, the torque rise time follows a linear relationship, and using the motor's maximum permissible speed results in a peak stagnation pressure of approximately 22 MPa, the average stagnation pressure of 5 MPa, is chosen to verify the system's ability to decelerate as well as the response accuracy of the servo loop and power electronics.
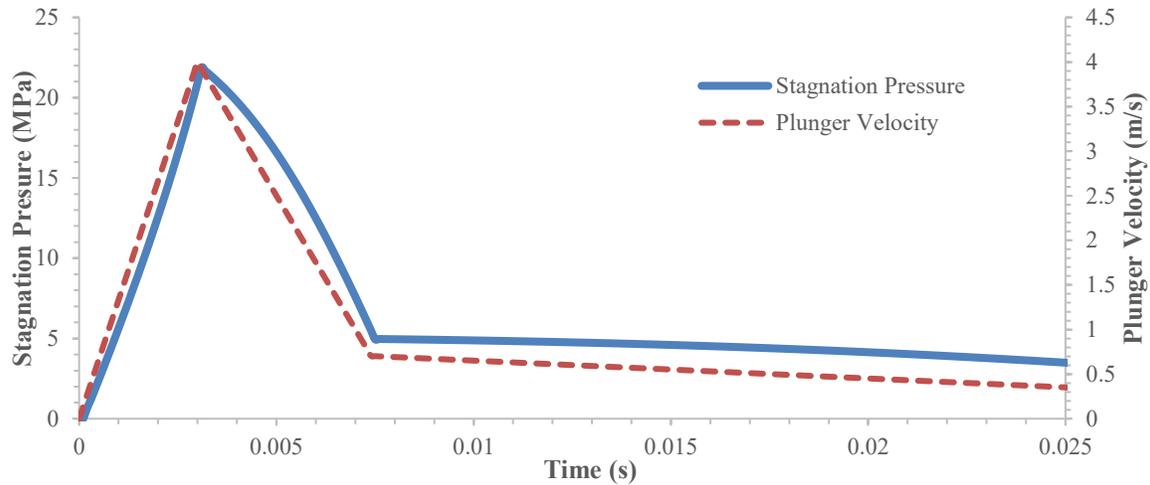
Figure 5.10 Stagnation pressure and plunger velocity as a function of time for screw driven injector

Figure 5.11 illustrates the corresponding behavior of screw speed and stagnation pressure as the injection progresses. The motor is ramped up to 166 rev/s, at which point the electromagnetic clutch is engaged, and the motor speed is held constant for 3 ms, allowing the clutch to fully synchronize the drive screw. The system is then under complete closed-loop control, and the motor is then decelerated rapidly to 20 rev/s, to the desired average stagnation pressure. Once the desired delivery volume is achieved the motor is decelerated rapidly to rest, and the clutch is disengaged.
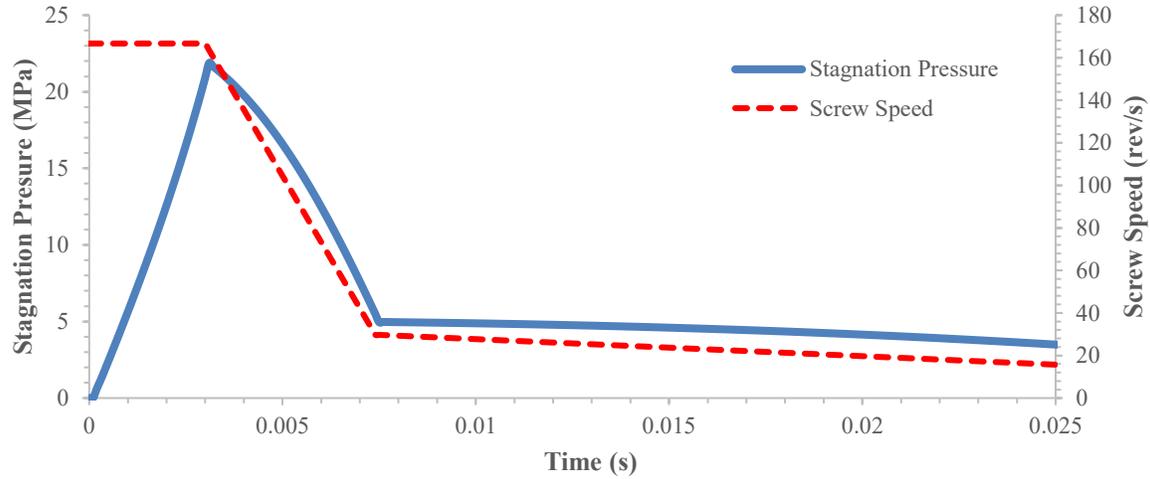
Figure 5.11 Stagnation pressure and screw speed as a function of time for screw driven injector

The proposed screw-driven injector should easily attain a peak stagnation pressure of 22 MPa, requiring a torque of 4.0 N·m and power consumption of approximately 375 Watts. The subsequent liquid jet will display a power of 83 watts if considering a typical nozzle diameter of 150 μm. The peak stagnation pressures can be increased in one of two ways, the first is by utilizing motors capable of higher rpm, the second method is to increase the lead distance of the drive screw. As previously mentioned, adding multiple starts to the lead screw can effectively increase the lead by the corresponding number of starts multiplied by the pitch distance of the threads. This will allow the plunger to translate further per revolution, achieving a greater maximum velocity. This parameter is known as the velocity ratio (*VR*) and can be defined by the product of the nominal outer circumference of the screw and the reciprocal of drive screw lead *l*. Moreover, the velocity ratio can be used to calculate the mechanical advantage *MA* of the power source. This is defined by the product of velocity ratio and drive screw efficiency to yield Eq. 5.5.

$$\frac{\pi D_{screw}}{l} = VR \qquad\qquad \text{Eq. (5.4)}$$

$$VR\eta = MA \qquad\qquad \text{Eq. (5.5)}$$

It should be noted that in this study the screw was optimized to produce higher velocity ratios, in fact, a mechanical advantage of approximately .85 is obtained for the parameters used in this conceptualization. Furthermore, adding multiple starts will lighten the drive screw lowering its moment of inertia, and distribute the axial reaction of fluid pressurization over a greater number

of threads, helping to relieve mechanical stress. However, it should be noted, that increasing drive screw lead will require a proportional increase in the amount of torque required, as is seen in Eq. 5.6, the torque is a product of both the screw lead and the force imposed by the back pressure of the fluid. The increase in lead will cause added torque requirements and the subsequent increase in plunger velocity will yield higher pressures within the injection chamber which will also increase torque requirements. In order to minimize torque requirements and increase stagnation pressures, a technique for over-speeding the motor can be used. Typically, the motor can be run at 150% of the rated speed momentarily, an optimization which minimizes drive screw lead and optimizes the torque delivery can be performed. From Eqs. 5.4 and 5.5 lead can be seen as the amount of mechanical advantage gained by the motor, smaller lead distances will require less driving torque at the expense of plunger speed. However, if the motor frequency is increased, higher stagnation pressures can be achieved without substantial increases in torque. It is realistic to predict that the current velocity scheme can be slightly altered to overspeed the motor to 250 rev/s and maintaining the same drive screw lead and peak stagnation pressure of 35 MPa can be achieved, with a torque of 5 N·m and 6 m/s peak plunger velocity. This begins to approach the lower end of stagnation pressures that were obtained using a detonation-driven device but exhibiting the controllability of a closed-loop servo system. If Eq. 5.2 is slightly modified to consider the axial force imposed by fluid pressurization as the product of the peak pressure desired and the diameter of the injection chamber plunger, then the following expression is obtained, whereby P_{max} represents the peak stagnation pressure and D_p is the diameter of the plunger.

$$\frac{P_{max}D_p^2 \times l}{8\eta} = T_s \qquad \text{Eq. (5.6)}$$

From Eq. 5.6, it is possible to see that decreasing the diameter of the plunger will also decrease the torque required to drive the injection forward. This can be exercised as a technique in which to further increase stagnation pressure, as the result will lower the torque requirements due to the pressure having a reduced surface area on which to act. The length of the injection chamber, plunger and drive screw can then be increased to account for the decrease in cross-sectional area caused by the reduction of the plunger diameter.

5.6 Summary

The future development of the screw-driven injector described in the aforementioned sections will result in a drug delivery device that combines the rapid energy release and practicality of combustion-driven injectors, whilst maintaining the controllability and precision of experimental prototypes powered by linear motors. Future iterations of the concept can examine the use of a ball screw to replace the traditional "*lead screw*" initially proposed. A ball screw makes use of spherical balls to reduce the surface contact between matching threads, leading to screw efficiency of over 90%. This can further help reduce torque demand and increase operating speeds. Nevertheless, the proposed injector design is composed of technologies which have been well characterized and when grouped will provide an excellent platform for the delivery of viscous injectables and cater to large volume injections.

Chapter 6 : Conclusions

6.1 Concluding Remarks

Drug delivery is one of the pillars of modern medicine, today's injectables not only help treat a variety of different ailments, but also serve in protecting against viruses and diseases. Over the past two decades, new emerging drug therapies accompanied by the increasing need to reduce biohazardous waste, curb needle reuse as well as accidental needle stick injuries, and eliminate the phobias associated with needles have led the scientific community to explore many viable needle-free technologies. The use of high-speed liquid jets for drug delivery remains the most versatile and promising technique for replacing traditional hypodermic needles. This simple concept which entails pressurizing the injectable and forcing it through an orifice, whereby it exits as a high-speed jet that exhibits enough energy to puncture human skin, can not only deliver common macro-molecules, but shows increasingly great potential for precise drug localization needed by revolutionary drug therapies.

The objective of the research work conducted throughout this study, aimed at contributing new tools and techniques for coping with some of the drawbacks that have limited the widespread use of NFJIs. Although versatile, studies have shown that they produced pain, bruising, hematomas and cross-contamination. In order to aid in eliminating these shortcomings and yield future injectors which demonstrate a higher degree of efficiency, precision and scalability a thorough investigation of power source requirements and power source designs was conducted.

The emergence of viscous, highly concentrated injectables, used primarily for vaccination purposes, requires novel delivery platforms. Utilizing a CFD model which mimics the power source behavior of gas-powered NFJIs, it was possible to determine that the current commercially available injectors are not well suited to cope with the added forces caused by an increase in fluid viscosity. In fact, it was observed that for a driver pressure of 410 kPa, and an increase of viscosity to a value of 65 cP approximately 100% decline in stagnation pressure was obtained. This was underlined by observing the corresponding Reynolds numbers which declined several orders of magnitude highlighting the impact of viscous forces on the jet injection. It is also important to note that the decrease in stagnation pressure is less sensitive to higher driver pressures. This leads to the conclusion that developing power sources with the ability to rapidly release greater amounts

of energy is required. This notion guided the research work to explore new techniques, as traditional gas-powered injectors have a practical limit to the pressurization that can be safely attained for hand-held usage.

The need to deliver viscous injectables as well as large volume injections typical of the animal health industry, in addition to a high level of controllability and precision, created a set of stringent power source requirements. In order to achieve this goal, the research work focused on illustrating the benefits of utilizing closed-loop control of linear permanent magnet synchronous motors, and the associated NFJI was termed a "*Servo Tube Jet Injector*". This device illustrated that it was possible to successfully decouple the frictional and outside forces that affect plunger displacement and rely solely on the control loop to maintain a plunger velocity trajectory prescribed by a mass balance that considers fluid pressurization. The device successfully shaped jets with preset pressure curves and was also capable of delivering pulsatile mode injections. Although improvements to the system presented in this study can be made with power electronics that exhibit greater ampacities and higher operating frequencies, the scalability of these devices for handheld operation will encounter some difficulty.

In order to achieve greater power generation and designs which can easily be scaled, the use of detonative combustion as a driving mechanism was considered. This technique harnessed the rapid pressure increase across Chapman-Jouguet (CJ) detonation to pressurize the drug, in a similar fashion to gas-powered NFJIs. The results of this study demonstrated great promise for the delivery of large volume injections and viscous injectables. The combustion-driven injector is capable of generating stagnation pressures exceeding 80 MPa, and delivering viscosities greater than 80 cP. Moreover, the mean and average stagnation pressures can be tailored by varying the initial pressure of the combustible gaseous mixture. This is accomplished via the modified use of a model based on the work conducted by Portaro and Ng (2015) and altered to consider combustion dynamics. The combustion-driven device illustrated both repeatability and precision while correlating well with the developed driving model.

The ability to produce an NFJI capable of exhibiting both the rapid energy release and scalability of a combustion-driven device and demonstrate the controllability provided by closed-loop control was also explored. This resulted in a new concept utilizing an ultra-low inertia servo motor coupled to an electromagnetic clutch and then utilizing a drive screw to convert the rotary motion to linear

motion. The clutch makes it possible to decouple the startup phase of the motor with the movement of the injection plunger. This makes it possible to use smaller motors and ramp them up to their optimal operating frequencies, and then through the rapid torque transfer of electromagnetic clutches, release energy to the drive screw pressurizing the fluid and creating high-speed liquid jets. An initial analysis of the hardware required for such a device led to an estimate of peak stagnation pressures of 22 MPa, and a margin to further reduce the sizing of the device while maintaining the same power output.

6.2 Contribution to Knowledge and Originality

The research conducted in this study has led to some significant contributions in helping advance the current state of NFJIs. One of the major findings was the inability of gas-powered injectors to produce adequate power for delivery of viscous injectables. This was accomplished through the use of a previously constructed CFD model and validated through experimental techniques. This CFD model can now be used to analyze power source requirements for fluid properties as well as provide a great tool for verifying the effect of injectables displaying different rheological behavior.

The study also demonstrated the successful use of PID closed-loop control of permanent magnet synchronous motors, for the controlled release of high-speed liquid jets. This study is the first to examine the controlled application of a specific plunger velocity profile through a true closed-loop three phase system. The platform developed in this study not only provides a means to accurately shape the pressure profiles of high-speed jets, but can also be utilized as development tool to study the effects of different stagnation pressure profiles, in the design and analysis stage of future NFJIs that do not exhibit real-time control.

Another important contribution was the successful use of detonation as a mechanism for powering an NFJI. This study characterized the behavior of this phenomenon for liquid jet injection and resulted in a predictive model which allows the peak and stagnation pressures to be altered through the amount of combustible gas that drives the detonation. The device demonstrated the ability to deliver viscous injection and provides a potential platform for emerging drug therapies.

This study compared the use of closed loop actuators and corresponding power electronics with the use of high powered techniques such as the use of a detonation wave for driving the liquid jet injection. The results illustrated that the use of power electronics yields precise real-time control

of jet stagnation pressure, however as injectable viscosity is increased, the detonative mechanism has the ability to better cope with power source requirements in a way that can be practically implemented for a clinical setting.

Lastly, the knowledge acquired in the development of two vastly different power sources was used to conceptualize the building blocks of a novel liquid jet injector providing key benefits of both closed loop control and rapid energy release. These contributions will help improve the quality of future NFJIs, highlighting the advantages of this technology as a viable alternative to hypodermic needles, reducing biohazardous waste, needle reuse, needle stick injuries, and helping to create a fear and pain free drug delivery experience.

References

Aerotech. Linear Motors: Application Guide. www.aerotech.com

Arora, A.; Hakim, I.; Baxter, J.; Rathnasingham, R.; Srinivasan, R.; Mitragotri, S. (2007) Needle free delivery of macromolecules across the skin by nanolitre-volume pulsed microjets. *Proc. Nat. Acad. Sci. USA* 104, 4255–4260.

Baker, A.B.; Sanders, J.E. (1999) Fluid mechanics analysis of a spring-loaded jet injector. *IEEE Trans. Biomed. Eng.* 46, 235–242.

Ball, N.B. (2007) *An Optimized Linear Lorentz-force Actuator for Biorobotics and Needle-free Injection*. Masters' Thesis, Massachusetts Institute of Technology, MA, USA.

Barolet, D.; Benohanian, A. (2018) Current trends in needle-free jet injection: an update. *Clin. Cosmet. Investig. Dermatol.* 11, 231–238.

Barton, I.E. (1998) Comparison of SIMPLE- and PISO-type algorithms for transient flows. *Int. J. Numer. Meth. Fluids* 26, 459-483.

Baxter, J.; Mitragotri, S. (2005) Jet-induced skin puncture and its impact on needle-free jet injections: Experimental studies and a predictive model. *J. Control. Release* 106, 361–373.

Baxter, J.; Mitragotri, S. (2006) Needle-free liquid jet injections: Mechanisms and applications. *Expert Rev. Med. Devices* 3, 565–574.

Beltman, W.M.; Shepherd, J.E. (2002) Linear elastic response of tubes to internal detonation loading. *J. Sound Vib.* 252, 617–655.

Berrospe-Rodriguez, C.; Visser, C.W.; Schlautmann, S.; Ramos-Garcia, R.; Fernandez Rivas, D. (2016) Continuous-wave laser generated jets for needle free applications. *Biomicrofluidics* 10, 014104.

Brennan, K.A.; Ruddy, B.P.; Nielsen, P.M.F.; Taberner, A.J. (2019) Classification of diffuse light emission profiles for distinguishing skin layer penetration of a needle-free jet injection. *Biomed. Opt. Express* 10 (10), 5081–5092.

Brown, M.B.; Martin, G.P.; Jones, S.A.; Akomeah, F.K. (2006) Dermal and transdermal drug delivery systems: Current and future prospects. *Drug Deliv.* 13, 175–187.

Budynas, R.; Nisbett, K. (2014) *Shigley's Mechanical Engineering Design*. 10th Ed., McGraw-Hill, NY, USA.

Chase, C.C.; Daniels, C.S.; Garcia, R. (2008) Needle-free injection technology in swine: Progress toward vaccine efficacy and pork quality. *J. Swine Health Prod.* 16, 254–261.

Chen, K.; Pan, M.; Liu, T. (2017) Design and analysis of a continuous split typed needle-free injection system for animal vaccination. *Open Biomed. Eng. J.* 11, 59–71.

Chen, K.; Zhou, H.; Li, J.; Cheng, G.J. (2010) A model on liquid penetration into soft material with application to needle-free jet injec-tion. *ASME J. Biomech. Eng.* 132, 101005.

Chen, K.; Zhou, H.; Li, J.; Cheng, G. (2011) Stagnation pressure in liquid needle-free injection: Modeling and experimental valida-tion. *J. Drug Deliv. Lett.* 1, 97–104.

Damazo, J.; Shepherd, J.E. (2017) Observations on the normal reflection of gaseous detonations. *Shock Waves* 27, 795–810.

Darcoid Norcal Seals., "O-ring load per linear inch of seal empirical chart" (www.darcoid.com/images/uploads/pdfs/empiricalcharts)

Do, N.N.L.; Taberner, A.J.; Ruddy, B.P. (2017) Design of a Linear Permanent Magnet Synchronous Motor for Needle-free Jet Injection. In *Proceedings of the 2017 IEEE Energy Conversion Congress and Exposition (ECCE),* Cincinnati, OH, USA, Oct. 1-5, 2017.

Do, N.N.L.; Taberner, A.J.; Ruddy, B.P. (2018) A linear permanent magnet synchronous motor for large volume needle-free jet injection. *IEEE Trans. Indust. Appl.* 55 (2), 1437–1446.

Fargnoli, A.S.; Katz, M.G.; Williams, R.D.; Marguilles, K.B.; Bridges, C.R. (2014) A needleless liquid jet injection delivery method for cardiac gene therapy: A comparative evaluation versus standard routes of delivery reveals enhanced therapeutic retention and cardiac specific gene expression. *J. Cardiovasc. Trans. Res.* 7, 756–767.

Ferziger, J.H.; Peric, M. (2004) *Computational Methods for Fluid Dynamics*. 3rd ed., Springer.

Fletcher, D.A.; Palanker, D.V. (2001) Pulsed liquid microjet for microsurgery. *Appl. Phys. Lett.* 78, 1933–1935.

Gad, S.C. (2008) *Pharmaceutical Manufacturing Handbook*. Wiley & Sons, Inc. NJ, USA.

Ghidaoui, M.S.; Zhao, M.; McInnis, D.A.; Axworthy, D.H. (2005) A review of water hammer theory and practice. *Appl. Mech. Rev.* 58, 49–76.

Golub, V.V.; Bazhenova, T.V.; Baklanov, D.I.; Ivanov, K.V.; Kirvokorytov, M.S. (2013) Using of hydrogen-air mixture detonation in needle-free injection devices. *High Temp.* 51, 138–140.

Gordon, S.; McBride, B.J. (1994) *Computer Program for Calculation of Complex Chemical Equilibrium Compositions and Applications*. Technical Report 1311; NASA Reference Publication; NASA: Washington, DC, USA.

Guang, T.H.; Wang, D.T. (1994) *Operation Manual of Sealing Components*. Mechanical Industry Press, Beijing, China.

Han, H.S.; Hong, J.Y.; Kwon, T.R.; Lee, S.E.; Yoo, K.H.; Choi, S.Y.; Kim, B.J. (2021) Mechanism and clinical applications of needle-free injectors in dermatology: Literature review. *J. Cosmetic Dermatology* 20 (12), 3793–3801.

Han, W.; Yang, G.; Law, C.K. (2017) Flame acceleration and deflagration-to-detonation transition in micro- and macrochannels: An integrated mechanistic study. *Combust. Flame* 176, 285–298.

Hingson, R.A.; Davis, H.S.; Rosen, M. (1963) Historical development of jet injection and envisioned uses in mass immunization and mass therapy based upon 2 decades experience. *Mil. Med.* 128, 516–524.

Karnesky, J.; Damazo, J.; Chow-Yee, K.; Rusinek, A.; Shepherd, J. (2013) Plastic deformation due to reflected detonation. *Int. J. Solids Struct.* 50, 97–110.

Kelley, E.L.; Smith, R.H.; Corcoran, G.; Nygren, S.; Jacoski, M.V.; Fernandes, A. (2021) Advances in subcutaneous injections: PRECISE II: a study of safety and subject preference for an innovative needle-free injection system. *Drug Deliv.* 28 (1), 1915–1922.

Kendall, M. (2006) Engineering of needle-free physical methods to target epidermal cells for DNA vaccination. *Vaccine* 24, 4651–4656.

Kendall, M.A. (2010) Needle Free Vaccine Injection. In *Handbook of Experimental Pharmacology*, Springer-Verlag, Berlin Heidelberg, Ch. 3, pp. 194-215.

Kim, J.K.; Mohizin, A.; Lee, S.K. (2018) Experimental investigation on key parameters in air-powered needle-free injection system for skin treatment, *J. Korean Soc. Vis.* 16 (1), 42–47.

Kiyama, A.; Endo, N.; Kawamoto, S.; Katsuta, C.; Oida, K.; Tanaka, A.; Tagawa, Y. (2019) Visualization of penetration of a high-speed focused microjet into gel and animal skin. *J. Vis.* 22, 449–457.

Kojic, N.; Goyal, P.; Lou, C.H.; Corwin, M.J. (2017) An innovative needle-free injection system: comparison to 1 ml standard subcutaneous injection. *AAPS PharmSciTech* 18, 2965–70.

Kolarsick, P.A.J.; Kolarsick, M.A.; Goodwin, C. (2011) Anatomy and physiology of the skin. *J. Derma. Nurses' Ass.* 3 (4), 203–213.

Krivokoritov, M.; Baklanov, D.; Golub, V.; Ivanov, K. (2012) Application of Gas Detonation for a Needleless Device Development. In *Proceedings of the 28th International Symposium on Shock Waves*, Manchester, UK, 17–22 July 2012; Kontis, K., Ed.; Springer: Berlin, Heidelberg, Germany, pp. 403–407.

Krizek, J.; De Goumoëns, F.; Delrot, P.; Moser, C. (2020) Needle-free delivery of fluids from compact laser-based jet injector, *Lab Chip* 20, 3784.

Kumar, A.; Prasad, P.S.; Rao, M.R. (2018) Experimental studies of water hammer in propellant feed system of reaction control system. *Propul. Power Res.* 7, 52–59.

Lee, J.H.S. (2018) *The Detonation Phenomenon*. Cambridge University Press, NY.

Lee, J.J.; Yi, K.H.; Kim, H.S.; An, M.H.; Seo, K.K.; Huh, C.H.; Kim, H.J. (2022) A novel needle-free microjet drug injector using Er:YAG laser: A completely new concept of transdermal drug delivery system. Clin. Anatomy 35, 682–685.

Li, X.; Ruddy, B.; Taberner, A. (2016) Characterization of needle-assisted jet injections. *J. Control. Release* 243, 195–203.

McGrath, J.A.; Eady, R.A.; Pope, F.M. (2004) Anatomy and Organization of Human Skin. In *Rook's Textbook of Dermatology*, 7th Ed., Burns, T.; Breathnach, S.; Cox, N.; Griffiths, C. Eds. Blackwell Science Ltd., NJ, USA.

McKeage, J.W.; Loch, C.; Zwirner, J.; Hammer, N.; White, D.E.; Ruddy, B.P.; Brunton, P.A.; Taberner, A.J. (2021) Controllable jet injection of dental local anaesthetic. *IEEE J. Trans. Eng. Health Med.* 9, 2300108.

McKeage, J.W.; Ruddy, B.P.; Nielsen, P.M.F.; Taberner, A.J. (2018) The effect of jet speed on large volume jet injection. *J. Control. Release* 280, 51–57.

Menezes, V.; Nakagawa, A.; Takayama, K. (2006) Laser-based pulsed liquid microjet for surgery. *J. Indian Inst. Sci.* 86, 207–214.

Mitragotri, S. (2005) Immunization without needles. *Nat. Rev. Immunol.* 5, 905–917.

Mitragotri, S. (2006) Current status and future prospects of needle free liquid jet injectors. *Nat. Rev. Drug Discov.* 5, 543–548.

Miyazaki, H.; Atobe, S.; Suzuki, T.; Iga, H.; Terai, K. (2019) Development of pyro-drive jet injector with controlled jet pressure. *J. Pharm. Sci.* 108, 2415-2420.

Miyazaki, Y.; Usawa, M.; Kawai, S.; Yee, J.; Muto, M.; Tagawa, Y. (2021) Dynamic mechanical interaction between injection liquid and human tissue simulant induced by needle-free injection of a highly focused microjet. *Sci. Rep.* 11, 14544.

Mohanty, C.; Mannavathy, C.; Srikanth, D.; Tabassum, R. (2011) Needle free drug delivery systems: A review. *Int. J. Pharm. Res. Dev. Ijprd* 3, 7–15.

Mohizin, A.; Kim, J.K. (2022) Dispersion profile of a needle-free jet injection depends on the interfacial property of the medium. *Drug Deliv. Trans. Res.* 12, 384–394.

Mohizin, A.; Lee, D.; Kim, J.K. (2021) Impact of the mechanical properties of penetrated media on the injection characteristics of needle-free jet injection. *Exp. Therm. Fluid Sci.* 126, 110396.

Mohizin, A.; Kim, J.K. (2020) Effect of geometrical parameters on the fluid dynamics of air-powered needle-free jet injectors. *Comput. Bio. Med.* 118, 103642.

Mousel, M.R.; Leeds, T.D.; White, S.N.; Herrmann-Hoesing, L.M. (2008) Technical note: Comparison of traditional needle vaccination with pneumatic, needle-free vaccination for sheep. *J. Anim. Sci.* 86, 1468–1471.

Nakayama, H.; Portaro, R.; Kiyanda, C.B.; Ng, H.D. (2015) CFD modeling and validation of high-speed liquid jets from an air-powered needle-free injection system. *J. Mech. Med. Biol.* 16, 1650045.

OpenCFD, "OpenFOAM, The Open Source CFD Toolbox," OpenCFD Ltd. 2013.

Portaro, R.; Ng, H.D. (2015) Experiments and modeling of air-powered needle free liquid injectors. *J. Med. Biol. Eng.* 35, 685–695.

Portaro, R.; Ng, H.D. (2022) Design and Analysis: Servo Tube Powered Liquid Jet Injector for Drug Delivery Applications. Accepted for *Appl. Sci.*, July 2022 (applsci-1796619).

Portaro, R.; Ng, H.D. (2017) Analysis of high-speed jets produced by a servo tube driven liquid jet injector. Presented at the 70th Annual Meeting of the APS Division of Fluid Dynamics, in Denver, CO, USA, Nov. 19-21, 2017.

Portaro, R.; Nakayama, H.; Ng, H.D. (2015) Optimization of drug viscosity used in gas-powered liquid jet injectors. In *Proceedings of the Annual International Conference of the IEEE Engineering in Medicine and Biology Society (EMBC)*, Milan, Italy, 25–29 August 2015.

Portaro, R.; Jaber, H.; Ng, H.D. (2017) Effects of viscosity on the performance of air-powered liquid jet injectors. Presented at the 70th Annual Meeting of the APS Division of Fluid Dynamics, in Denver, CO, USA, Nov. 19-21, 2017.

Portaro, R.; Sadek, J.; Xu H.; Ng, H.D. (2019) Controlled release using gas detonation in needle-free liquid jet injections for drug de-livery. *Appl. Sci.* 9 (13), 2712.

Rane, Y.S.; Marston, J.O. (2021) Transient modelling of impact driven needle-free injectors. *Comput. Bio. Med.* 135, 104586.

Rao, S.S.; Gomez, P.; Mascola, J.R.; Dang, V.; Krivulka, G.R.; Yu, F.; Lord, C.I.; Shen, L.; Bailer, R.; Nabel, G.J.; et al. (2006) Comparative evaluation of three different intramuscular delivery methods for DNA immunization in a nonhuman primate animal model. *Vaccine* 24, 367–373.

Ravi, A.D.; Sadhna, D.; Nagpaal, D.; Chawla, L. (2015) Needle free injection technology: a complete insight. *Int. J. Pharm. Investig.* 5, 192–199.

Raviprakash, K.; Porter, K.R. (2006) Needle-free injection of DNA vaccines: A brief overview and methodology. *Methods. Mol. Med.* 127, 83–89.

Rohilla, P.; Marston, J.O. (2019) In-vitro studies of jet injections. *Int. J. Pharmaceutics* 568, 118503.

Ruddy, B.; Dixon, A.; Williams, R.; Taberner, A. (2017) Optimization of portable electronically-controlled needle-free jet injection systems. *IEEE/Asme Trans. Mechatron.* 22, 2013–2021.

Ruddy, B.P.; Bullen, C.; Ting J.W.C.; Jeong. S.H.; Madadkhahsalmassi, B.; McKeage, J.W.; Svirskis, D.; Tingle, M.D.; Xu, J.; Taberner, A.J. (2019) Subcutaneous nicotine delivery via needle-free jet injection: A porcine model. *J. Control. Release* 306, 83–88.

Schneider, U.; Birnbacher, R.; Schober, E. (1994) Painfulness of needle and jet injection in children with diabetes mellitus. *Eur. J. Pediatr.* 153, 409–410.

Schneider, A.; Mueller, P.; Jordi, C.; Richard, P.; Sneeringer, P.; Nayyar, R.; Yovanoff, M.; Lange, J. (2020) Hold the device against the skin: the impact of injection duration on user's force for handheld autoinjectors. *Expert Opin. Drug Deliv.* 17, 225–36.

Schoppink, J.; Fernandez Rivas, D. (2022) Jet injectors: Perspectives for small volume delivery with lasers. *Adv. Drug Deliv. Rev.* 182, 114109.

Schramm, J.R.; Mitragotri, S. (2002) Transdermal drug delivery by jet injectors: Energetics of jet formation and penetration. *Pharm. Res.* 19, 1673–1679.

Schramm-Baxter, J.; Mitragotri, S. (2004) Needle-free jet injections: Dependence of jet penetration and dispersion in the skin on jet power. *J. Control. Release* 97, 527–535.

Shapiro, J.R.; Hodgins, B.; Hendin, H.E.; Patel, A.; Menassa, K.; Menassa, C.; Menassa, M.;.Pereira, J.A.; Ward, B.J. (2019) Needle-free delivery of influenza vaccine using the Med-Jet® H4 is efficient and elicits the same humoral and cellular responses as standard IM injection: A randomized trial. *Vaccine* 37 (10), 1332–1339.

Shergold, O.A.; Fleck, N.A.; King, T.S. (2006) The penetration of a soft solid by a liquid jet, with application to the administration of a needle-free injection. *J. Biomech.* 39, 2593-2602.

Shepherd, J.E.; Teodorczyk, A.; Knystautas, R.; Lee, J.H.S. (1991) Shock waves produced by reflected detonations. *Prog. Astro. Aero.* 134, 244–264.

Stachowiak, J.C.; von Muhlen, M.G.; Li, T.H. (2007) Piezoelectric control of needle free transdermal drug delivery. *J. Control. Release* 124, 88-97.

Stanyukovich, K.P. (1960) *Unsteady Motion of Continuous Media*. Pergamon Press, NY, USA.

Taberner, A.; Hogan, N.C.; Hunter, I.W. (2012) Needle-free jet injection using real-time controlled linear Lorentz-force actuators. *Med. Eng. Phys.* 34, 1228–1235.

Tagawa, Y.; Oudalov, N.; Visser, C.W.; Peters, I.R.; van der Meer, D.; Sun, C.; Prosperetti, A.; Lohse, D. (2012) Highly focused supersonic microjets. *Phys. Rev. X* 2, 031002.

Vadlapatla, R.; Gayakwad, S.; Yellepeddi, V.; Wong, E.Y. (2021) Needle-free injectors. In *Drug Delivery Devices and Therapeutic Systems*, 1st ed.; Chappel, E., Ed.; Academic Press, London, UK, pp. 199–211.

Vasil'ev, V.V. (2013) The principle aspects of application of detonation in propulsion systems. J. *Combust.* 945161.

Wijsmuller, G.; Snider, D.E., Jr. (1975) Skin testing: A comparison of the jet injector with the Mantoux method. *Am. Rev. Respir. Dis.* 112, 789–798.

Williams, R.M.J.; Ruddy, B.P.; Hogan, N.C.; Hunter, I.W.; Nielsen, P.M.F.; Taberner, A.J. (2016) Analysis of moving-coil actuator jet injectors for viscous fluids. *IEEE Trans. Biomed. Eng.* 63, 1099–1106.

Wolanski, P. (2013) Detonative propulsion. *Proc. Combust. Inst.* 34, 125–158.

Wu, M.H.; Burke, M.P.; Son, S.F.; Yetter, R.A. (2007) Flame acceleration and the transition to detonation of stoichiometric ethylene/oxygen in microscale tubes. *Proc. Combust. Inst.* 31, 2429–2436.

Wu, M.H.; Wang, C.Y. (2011) Reaction propagation modes in millimeter-scale tubes for ethylene/oxygen mixtures. *Proc. Combust. Inst.* 33, 2287–2293.

Zeng, D.; Wu, N.; Qian, L.; Shi, H.; Kang, Y. (2020) A novel controllable pneumatic needle-free injection system for large-volume drug delivery. *J. Pharma. Sci.* 109 (5), 1772-1779.

Zhang, A.; Hogan, N.C.; Hunter, I.W. (2017) Needle-free small-volume Liquid Injection System Powered by a Rotary Actuator. *Proc. Ann. Int Conf. IEEE Eng. Med. Biol. Soc.* 292-295.